Magnetotransport properties of selected high entropy alloys

Kuveždić, Marko

Doctoral thesis / Doktorski rad

2023

Degree Grantor / Ustanova koja je dodijelila akademski / stručni stupanj: **University of Zagreb, Faculty of Science / Sveučilište u Zagrebu, Prirodoslovno-matematički fakultet**

Permanent link / Trajna poveznica: https://urn.nsk.hr/urn:nbn:hr:217:537445

Rights / Prava: In copyright / Zaštićeno autorskim pravom.

Download date / Datum preuzimanja: **2024-05-16**

Repository / Repozitorij:

Repository of the Faculty of Science - University of Zagreb

University of Zagreb

Faculty of Science
Department of Physics

Marko Kuveždić

Magnetotransport properties of selected high entropy alloys

DOCTORAL DISSERTATION

Zagreb, 2023

University of Zagreb

Faculty of Science
Department of Physics

Marko Kuveždić

Magnetotransport properties of selected high entropy alloys

DOCTORAL DISSERTATION

Supervisor:
assoc. prof. dr. sc. Mario Basletić

Zagreb, 2023

Sveučilište u Zagrebu

Prirodoslovno-matematički fakultet
Fizički odsjek

Marko Kuveždić

Magnetotransportna svojstva odabranih visokoentropijskih slitina

DOKTORSKI RAD

Mentor:
izv. prof. dr. sc. Mario Basletić

Zagreb, 2023

Supervisor information

Assoc. Prof. Mario Basletić obtained his PhD in Physics in 2003 from the Faculty of Science, University of Zagreb, under the supervision of dr. Bojana Hamzić on the topic of experimental magnetotransport properties of selected low dimensional organic conductors. In 2006-2007, he took a postdoctoral leave at Unité Mixte de Physique CNRS/Thales (Université Paris-Sud), Palaiseau, France, where he began working on oxide heterostructures and multiferroic systems with potential applications in spintronics.

After returning to the Department of Physics at the Faculty of Science, University of Zagreb as an Assistant Professor, he expanded his research to include experimental studies of highly correlated systems and high-entropy alloys. To date, he has published 62 scientific papers indexed in the Web of Science database, which have received a total of 1775 citations, resulting in an h-index of 19. He has also contributed to numerous conference talks and posters and has been a team member on several scientific projects.

In addition to his research, he is active in teaching and currently teaches Fundamentals of Physics 1-4.

Acknowledgements

I would like to express my deepest gratitude to all those who have supported and guided me throughout the process of completing this thesis.

First and foremost, I owe a debt of gratitude to my loving parents, Vlatko and Ana, my sister, Danijela, and to the rest of my family, for their unwavering support and encouragement throughout my academic journey. Their love and belief in me have been the foundation of my achievements.

I am deeply grateful to my supervisor, assoc. prof. dr. sc. Mario Basletić, for his patience and guidance during the entire process, from conducting my measurements to the writing of this thesis. His expertise and support have been instrumental in the completion of this work.

My sincere thanks go to my colleague assoc. prof. dr. sc. Emil Tafra for his invaluable assistance with the measurements, patiently answering all my questions, and helping me troubleshoot problems. His expertise and patience have greatly contributed to the success of my research.

To my college friends Petar Marević, Matija Kalanj, Saša Vrcelj, Pavao Andričević, and Jure Dragović, thank you for your steadfast friendship and support during and after college. Our annual trips abroad have been an incredible source of joy, providing much-needed respite from academic endeavours.

I would also like to extend my gratitude to Marko Šušak for ensuring that I had access to liquid helium and liquid nitrogen, and to Marko Hum for helping me navigate the PhD bureaucracy. I am also grateful to prof. dr. sc. Emil Babić and dr. sc. Ignacio A. Figueroa for supplying the ribbon samples used in this thesis.

Lastly, I am thankful to all my other colleagues who have lent a helping hand when needed, assisting with measurements and troubleshooting various issues.

This thesis would not have been possible without the collective efforts of all the individuals mentioned above, and I am eternally grateful for their contributions to my success.

Abstract

This thesis presents the findings of a comprehensive, systematic study of transport properties, including resistivity, Hall effect, magnetoresistance, and superconductivity, in amorphous quinary alloys of early and late transition metals. The research focused on metallic glass ribbons from three alloy systems: $(TiZrNbNi)_{1-x}Cu_x$, $(TiZrNbCu)_{1-x}Ni_x$, and $(TiZrNbCu)_{1-x}Co_x$, spanning a broad composition range, along with three alloy variants with a fixed TL (Cu, Ni) content and compositions: $Ti_{0.30}Zr_{0.15}Nb_{0.15}Ni_{0.20}Cu_{0.20}$, $Ti_{0.15}Zr_{0.30}Nb_{0.15}Ni_{0.20}Cu_{0.20}$, and $Ti_{0.15}Zr_{0.15}Nb_{0.30}Ni_{0.20}Cu_{0.20}$. In addition, measurements were conducted on an amorphous thin film of TiZrNbCuNi, which was deposited on a $SrLaAlO_4$ substrate using a pulsed laser deposition (PLD) system. The results of resistivity, Hall effect, magnetoresistance, and superconductivity measurements largely agree with those reported in previous investigations on related binary and ternary amorphous alloys. However, we identified a novel model of two parallel conducting channels, composed of a metal-like and a variable range hopping (VRH)-like channel, that better describes the temperature variation of resistivity observed in our experiments. A possible mechanism for the origin of these two conductance channels was proposed.

Keywords: amorphous alloys, metallic glasses, amorphous thin films, pulsed laser deposition, transport properties, resistivity, Hall effect, magnetoresistance, superconductivity, weak localization, enhanced electron-electron interactions, Anderson localization, variable range hopping

Prošireni sažetak

Materijali s kristalnim uređenjem uvijek su privlačili veliki interes znanstvene zajednice, posebno od razvoja kvantne mehanike. Međutim, savršene kristalne strukture su češće iznimka nego pravilo u prirodi. Umjesto toga, strukture u materijalima variraju od kristalnih rešetci s malim brojem defekata, do vrlo neuređenih amorfnih (staklastih) struktura.

Amorfni metali su čisti metali ili legure koje ne posjeduju dugodosežno atomsko uređenje, a nastaju raznim tehnikama brzog hlađenja taljevine ili plina. Brzina procesa sprječava stvaranje uređene kristalne faze pa atomi ostaju „smrznuti" u metastabilnom stanju koje nalikuje tekućoj fazi. Razvoj tehnika brzog hlađenja tijekom 1960-ih doveo je do povećanog interesa za amorfna metalna stakla i utjecaja dugodosežnog (ne)uređenja na elektronsku strukturu, mehanička, magnetska i električna svojstva metala.

Među metalnim staklima, od posebnog su značaja slitine ranih (Ti, Zr, Nb, Hf) i kasnih (Fe, Co, Ni, Cu) prijelaznih metala, poznate skraćeno kao TE–TL slitine. Ove slitine su od posebnog interesa zbog širokog raspona koncentracija (obično između 20 % i 70 % sadržaja kasnih prijelaznih metala) za koje je moguće formirati metalno staklo. Ovo svojstvo omogućuje detaljno i sustavno proučavanje ovisnosti svojstava materijala o kemijskom sastavu, jer je kod amorfnih slitina, za razliku od kristalnih, moguće dobiti homogenu jednofaznu smjesu s kontinuiranim vrijednostima kemijskog sastava.

Tijekom godina, fokus u razvoju novih materijala polako se pomaknuo s binarnih i ternarnih slitina na složenije, višekomponentne slitine. Tradicionalna strategija razvoja višekomponentnih slitina sastojala se od korištenja jednog ili najviše dva glavna elementa i dodavanja malih količina drugih elemenata kako bi se postigla željena sekundarna svojstva. Međutim, ovaj pristup dizajnu slitina je dosta restriktivan i ostavlja ogromno neistraženo područje u središtu faznog dijagrama višekomponentnih slitina. Početkom ovog stoljeća, u potrazi za novim masivnim metalnim staklima (engl. bulk metallic glasses), upotrijebljena je nova strategija koja koristi višekomponentne legure s gotovo ekviatomskim koncentracijama. Ovaj pristup brzo se proširio na kristalne slitine visoke entropije (engl. high-entropy alloys) te konačno i na intermetalne spojeve i keramike.

Ove višekomponentne slitine i njihova amorfna stanja predstavljaju nove i zanimljive pravce istraživanja. Njihovim istraživanjem možemo proširiti naše razumijevanje utjecaja kemijskog sastava te kemijskog i strukturnog nereda na svojstva materijala. Ta znanja mogu dovesti do razvoja novih materijala s poboljšanim svojstvima i potencijalnim industrijskim primjenama.

U skladu s ovim razvojima, ovaj rad prezentira rezultate opsežnog i sustavnog istraživanja transportnih svojstava, uključujući otpornost, Hallov efekt, magnetootpor i supravodljivost, u amorfnim višekomponentnim slitinama ranih i kasnih prijelaznih metala. Istraživanje se primarno sastojalo od mjerenja traka metalnih stakala (engl. metallic glass ribbons) iz tri sustava kvinarnih slitina: $(\mathrm{TiZrNbNi})_{1-x}\mathrm{Cu}_x$, $(\mathrm{TiZrNbCu})_{1-x}\mathrm{Ni}_x$ i $(\mathrm{TiZrNbCu})_{1-x}\mathrm{Co}_x$ u širokom rasponu kemijskog sastava od gotovo ekviatomskih slitina visoke entropije ($0 \leq x \leq 0.35$) do konvencionalnih slitina s jednim glavnim elementom ($x \geq 0.35$). Dodatno, provedena su mjerenja na amorfnom tankom filmu TiZrNbNiCu, koji je deponiran na $\mathrm{SrLaAlO_4}$ supstrat pomoću tehnike pulsne laserske depozicije.

Na svim uzorcima metalnih staklenih traka izmjereni su supravodljivi prijelazi iznad 300 mK, osim za $(\mathrm{TiZrNbNi})_{0.5}\mathrm{Cu}_{0.50}$ i $(\mathrm{TiZrNbCu})_{0.57}\mathrm{Co}_{0.43}$ slitine. Temperature supravodljivog prijelaza T_c su niže od onih u srodnim binarnim slitinama na bazi Zr, što je najvjerojatnije rezultat negativnog utjecaja Ti, opaženog i u binarnim TE–TL slitinama. U skladu s amorfnim i kristalnim TE–TL slitinama, temperature supravodljivog prijelaza padaju s povećanjem koncentracije kasnih prijelaznih metala.

Vrijednosti Hallovog koeficijenta R_H su u skladu s amorfnim binarnim TE–TL slitinama. Svi Hallovi koeficijenti su pozitivni, osim za $(\mathrm{TiZrNbCu})_{0.57}\mathrm{Co}_{0.43}$ slitinu. U $(\mathrm{TiZrNbCu})_{1-x}\mathrm{Co}_x$ slitinama uočena je promjena predznaka Hallovog koeficijenta R_H s porastom koncentracije x. Kritična koncentracija je oko $x(\mathrm{Co}) = 0.34$. U $(\mathrm{TiZrNbCu})_{1-x}\mathrm{Ni}_x$ slitinama primijećen je blagi pad vrijednosti s većim koncentracijama x. Ekstrapolirana kritična vrijednost je približno $x(\mathrm{Ni}) = 0.6$. Hallovi koeficijenti u $(\mathrm{TiZrNbNi})_{1-x}\mathrm{Cu}_x$ slitinama ostali su približno nepromijenjeni u cijelom mjernom području koncentracija. Prijelazi iz pozitivnih u negativne vrijednosti Hallovog koeficijenta korelirani su s promjenom karaktera d-elektrona na Fermijevom nivou, iz d-elektrona ranih u d-elektrone kasnih prijelaznih metala.

Na svim uzorcima metalnih staklenih traka izmjerene su visoke vrijednosti otpornosti na sobnoj temperaturi (140-240 $\mu\Omega\,\mathrm{cm}$) i mali negativni temperaturni koeficijent otpornosti. Otpornosti na sobnoj temperaturi su rasle s povećanjem koncentracije kasnih prijelaznih metala, u skladu s binarnim TE–TL slitinama, osim za $(\mathrm{TiZrNbCu})_{1-x}\mathrm{Co}_x$ slitine, gdje je primijećena veća promjena nego što je zabilježeno u binarnim $\mathrm{Zr}_{1-x}\mathrm{Co}_x$ slitinama.

Na svim uzorcima je izmjeren pozitivan magnetootpor za magnetska polja do 10 T, dok je za veća polja opažen mogući pad vrijednosti u par mjerenih uzoraka. Promjena u magnetskom polju je u skladu s binarnim amorfnim TE–TL slitinama. Proporcionalno kvadratu magnetskog polja $\propto B^2$ na niskim poljima i proporcionalno korijenu magnetskog polja $\propto \sqrt{B}$ na visokim poljima. Izmjerena ovisnost o magnetskom polju je kvalitativno, pa čak i kvantitativno, u skladu s binarnim amorfnim TE–TL slitinama.

Mjerenja su pokazala jako dobro slaganje sa srodnim binarnim TE–TL slitinama, što sugerira da ove kvinarne slitine možemo promatrati kao pseudo-binarne slitine ranih i kasnih prijelaznih materijala $\mathrm{TE}_{1-x}\mathrm{TL}_x$.

Posebna pažnja posvećena je temperaturnoj ovisnost otpornosti, odnosno pripadnom malom negativnom koeficijentu otpornosti. Iako se u literaturi navedena temperaturna ovisnost pripisuje temperaturno ovisnim komponentama efekata slabe lokalizacije (engl. weak localization) i pojačane elektron-elektron interakcije (engl. enhanced electron-electron interaction), u ovom radu je predložen novi model s dva paralelna kanala vodljivosti koji bolje opisuju izmjerenu temperaturnu ovisnost otpornosti. Jedan kanal pokazuje metalnu vodljivost, dok drugi kanal pokazuje temperaturnu ovisnost nalik preskakanju promjenjivog dosega (engl. variable range hopping, VRH).

Metalni kanal vodljivosti je temperaturno neovisan na višim temperaturama ($\gtrsim 20\,\mathrm{K}$), što pripisujemo elastičnim raspršenjima na neuređenoj rešetci, takozvani rezidualni otpor. Na niskim temperaturama ($\lesssim 20\,\mathrm{K}$), ova komponenta otpornosti opada s temperaturom, što pripisujemo temperaturno ovisnom doprinosu slabe lokalizacije i pojačane elektron-elektron interakcije.

Za drugi kanal vodljivosti, koji pokazuje temperaturnu ovisnost preskakanja promjenjivog dosega, predložili smo da je rezultat formiranja zona lokaliziranih i delokaliziranih stanja. Delokalizirana stanja formiraju beskonačni klaster i više malih konačnih klastera. Metalni kanal vodljivosti je rezultat difuznog gibanje elektrona kroz beskonačni klaster. Međutim, ne doprinose svi dijelovi beskonačnog klastera ovom difuznom transportu elektrona, te dijelove možemo nazvati *slijepe ulice*. Preskakanjem između ovih slijepih ulica i/ili konačnih klastera stvaraju se kanali vodljivosti paralelni beskonačnom klasteru. Zbog temperaturno neovisne vodljivosti beskonačnog klastera ($\gtrsim 20\,\mathrm{K}$), uključujući i slijepih ulica, temperaturna ovisnost otpornosti ovih paralelnih kanala bit će rezultat temperaturne ovisnosti preskakanja promjenjivog dosega $\exp(T_{\mathrm{VRH}}/T)^{1/2}$.

Mjerenja transportnih svojstava amorfnog tankog filma, procijenjene debljine u rasponu od 100-200 nm, pokazuju dobro slaganje s uzorcima metalnih staklenih traka. Depozicijom novih tankih filmova raznih debljina, može se proučavati utjecaj dimenzionalnosti

na vrijednosti i temperaturnu ovisnost transportnih svojstava. Takvo istraživanje bi moglo pružiti vrijedan uvid u prirodu ova dva kanala vodljivosti te pomoći u testiranju valjanosti predloženog modela vodljivosti na amorfne slitine visoke otpornosti.

Ključne riječi: amorfne slitine, metalna stakla, amorfni tanki filmovi, pulsna laserska depozicija, transportna svojstva, otpornost, Hallov efekt, magnetootpor, supravodljivost, slaba lokalizacija, pojačane elektron-elektron interakcije, Andersonova lokalizacija, preskakanje promjenjivog dosega

Contents

Introduction **1**

1 Amorphous Metals **5**
1.1 Glass formation . . . 5
1.2 Structure of amorphous metals . . . 9
1.3 Electronic structure of TE–TL alloys . . . 13
1.4 Transport properties . . . 16
1.4.1 Hall effect . . . 17
1.4.2 Resistivity . . . 21
1.4.2.1 Weak localization . . . 22
1.4.2.2 Electron-electron interaction effects . . . 28
1.4.2.3 Temperature dependence of resistivity . . . 31
1.4.2.4 Magnetoresistance from quantum corrections . . . 34
1.4.2.5 Magnetoresistance in TE–TL alloys . . . 40
1.4.3 Superconductivity . . . 43

2 Concepts **46**
2.1 Anderson localization . . . 46
2.2 Variable range hopping . . . 50
2.2.1 VRH in Granular Metals . . . 54
2.3 Lifshitz model . . . 60

3 Samples and Experimental Methods **62**
3.1 Metallic glass ribbon samples . . . 62
3.2 Amorphous thin film samples . . . 65
3.3 Transport measurements . . . 70
3.4 Superconducting Magnet System . . . 73

4 Results and discussion **76**
4.1 Superconductivity . . . 76
4.2 Hall effect . . . 80
4.3 Resistivity . . . 82
4.3.1 Temperature dependence of resistivity . . . 83
4.3.2 VRH . . . 93

4.3.3 Low-temperature resistivity 103
4.3.4 Magnetoresistance 110

5 Summary and Outlook **116**

References **119**

Biography **128**

Introduction

Crystalline materials have received extensive interest since the advent of quantum mechanics. However, perfect crystalline structures are more the exception than the norm in nature. Disorder can manifest in various forms, ranging from minor impurities within a crystal lattice to the highly disordered extremes observed in amorphous (glassy) structures.

The advent of rapid quenching techniques and the first metallic glasses in the 1960s [1] marked a pivotal moment in the investigation of amorphous materials' properties. This category of materials introduced a new domain in material science beyond the crystal lattice. Several questions arose as a consequence of this development: How does the absence of long-range order influence the electronic structure, mechanical, magnetic, and electrical properties? What are the implications of disorder and short-range order? And why do crystalline and amorphous materials with identical compositions exhibit some shared properties but not others?

These and other questions have spurred new experimental and theoretical research endeavours. For instance, due to the high disorder, conduction electrons exhibit a very short mean free path, causing their behaviour to deviate from models based on the Boltzmann transport equations, which have been effective in describing transport properties of, for example, crystalline metals. As a result, examination of quantum corrections to the Boltzmann theory and alternative theories became necessary.

For example, with short elastic and long phase-breaking (inelastic) mean free paths, interference effects between incident and scattered electron wavefunctions can become significant. This aspect, not accounted for in the Boltzmann transport equations, places special emphasis on electron paths forming closed loops, as there are then two paths of equal length for the electron wavefunction—specifically, the closed path executed in opposite directions. If the electron wavefunctions maintain phase coherence, the two partial waves can reinforce each other, thereby doubling the probability of such paths compared to classical expectations.

Among metallic glasses, one of the notable categories are alloys of early (Ti, Zr, Nb, Hf) and late (Fe, Co, Ni, Cu) transition metals, known as TE–TL alloys. These alloys are of particular interest due to the wide range of compositions (typically 20-70 % of TL content) that form metallic glasses [2]. This property is highly advantageous, as unlike crystalline alloys, homogeneous single-phase systems of amorphous alloys can be prepared with continuously varying compositions. As a result, the properties of the system can be examined as a function of composition without the interference of structural phase transitions, providing valuable insights into the properties and behaviour of these alloys.

Moreover, these alloys belong to the group of so-called strong scattering alloys [3], which display negative temperature coefficients of resistivity and positive Hall coefficients, contradicting the nearly free electron models developed for weakly scattering metals. Consequently, extensive research has been conducted on this class of alloys [3–8].

Over the years, the focus of new materials development has transitioned from binary and ternary alloys to more complex, multicomponent alloys. The conventional strategy involved using one or, at most, two principal components, and then incorporating small amounts of various other elements to impart secondary properties. However, this approach to alloy design is restrictive, leaving a vast, underexplored region in the middle of the phase diagram of multicomponent alloys.

At the start of this century, in an effort to discover new bulk metallic glasses, a novel method was introduced that used multicomponent alloys with nearly equiatomic concentrations [9, 10]. According to traditional understanding, these multicomponent alloys should have resulted in the formation of numerous phases and intermetallic compounds. However, experimental studies found a remarkably smaller number of phases in these systems, and even single-phase solid solutions [11, 12]. These single-phase solid solutions quickly attracted attention and spurred a significant expansion of research into multicomponent, nearly equiatomic alloys [13, 14]. It was proposed that high configurational entropy in these systems increases the stability of solid solutions relative to intermetallic compounds [12], leading to the term *high entropy alloys*. This research subsequently extended to high entropy intermetallic compounds and ceramics [13, 14].

These novel multicomponent alloys and their corresponding amorphous states offer intriguing research opportunities, shedding light on the effects of compositional variations and chemical complexity on material properties. Moreover, alloys exhibiting both a solid solution phase and an amorphous (metallic glass) phase, such as $Al_{0.5}$TiZrPdCuNi [15, 16], allow for direct comparisons between systems that share chemical disorder, but one possesses structural order, while the other is structurally disordered.

Understanding the intricate relationship between chemical and structural disorder, composition, and material properties in these alloys can offer valuable insights, contributing to the advancement of materials science. This knowledge may lead to the discovery of new materials with improved performance and potential applications across various industries. Ultimately, continued research in this area holds significant potential to influence the future of materials science and technology.

Following these developments, the research conducted and presented in this thesis focuses on measuring and classifying the electronic properties, including electrical resistivity, magnetoresistance, Hall effect, and superconductive transitions, of amorphous samples from three quinary TE–TL alloy systems: $(\mathrm{TiZrNbCu})_{1-x}\mathrm{Ni}_x$, $(\mathrm{TiZrNbNi})_{1-x}\mathrm{Cu}_x$, and $(\mathrm{TiZrNbCu})_{1-x}\mathrm{Co}_x$, encompassing both the nearly equiatomic high entropy range ($0 \leq x \leq 0.35$) and the conventional range ($x \geq 0.35$). Additionally, a proof-of-concept amorphous thin films of TiZrNbNiCu have been fabricated using pulsed laser deposition, representing an initial step in exploring the effects of dimensionality on this class of amorphous metal alloys. Part of the research present in this work, has already been published in two papers [17, 18].

The structure of this thesis is organized as follows:

Chapter 1 provides a definition of amorphous metals and metallic glasses, and a brief discussion of their key structural properties. This is followed by an overview of the transport properties, including resistivity, Hall effect, magnetoresistance, and superconductivity, in high-resistivity amorphous materials, with a primary focus on amorphous TE–TL alloys.

Chapter 2 introduces relevant concepts and theories that will be useful in the analysis and discussion of the obtained results.

Chapter 3 details the experimental setups and methodologies for data collection and analysis presented in this work. Furthermore, it briefly describes the preparation of the amorphous ribbon samples employed in this research, which were prepared by Dr. Ignacio A. Figueroa at the *Institute for Materials Research–UNAM, Mexico*. Additionally, Section 3.2 outlines the preparation of amorphous thin films of the TiZrNbCuNi alloy using pulsed laser deposition at the *Department of Physics, Faculty of Science in Zagreb*, and their characterisation.

Chapter 4 presents the results of transport measurements conducted on amorphous ribbon and thin film samples, comparing and contrasting these findings with similar binary TE–TL metallic glass alloys. In addition, a novel description of the temperature dependence of resistivity is introduced, which suggests the presence of two parallel con-

ducting channels in the studied alloys: one metallic-like and the other resembling variable range hopping (VRH).

Lastly, **Chapter 5** offers a summary of key findings and potential avenues for future research.

Chapter 1

Amorphous Metals

Amorphous metals are pure metals or alloys possessing no long-range atomic order. They are typically formed by a variety of techniques which involve rapid solidification from the gas or liquid phases. Common methods include melt spinning, splat quenching, and evaporation or sputtering onto a substrate. The solidification occurs so rapidly that it leaves no time for nucleation and crystal growth, and so the equilibrium crystalline phase is not reached. Instead, atoms solidify into a disordered, thermodynamically metastable state that is similar to the liquid phase, i.e. to a glassy state [19]. In some cases, amorphous metals can also be produced by mechanical alloying, ion implantation or electrochemical deposition.

1.1 Glass formation

We can examine the formation of an amorphous, glassy state by monitoring changes that occur in the material as it cools from a liquid state. For instance, we can track the volume change with temperature, as illustrated in Figure 1.1. When the temperature of a liquid metal is gradually lowered, its volume decreases until it reaches the melting point T_{m}. At this temperature, the volume experiences a sudden drop, reaching a value typical of the solid crystalline metal. As it continues to cool, the volume decreases gradually, depending on the coefficient of thermal expansion.

During the crystallization process, the liquid typically experiences undercooling, enabling the liquid state to persist below the melting temperature. This occurs because an activation energy barrier must be overcome for nucleation sites to form. The extent of undercooling relies on various factors, including: the viscosity of the liquid, the free energy difference between the undercooled melt and the crystal phases, the imposed cooling

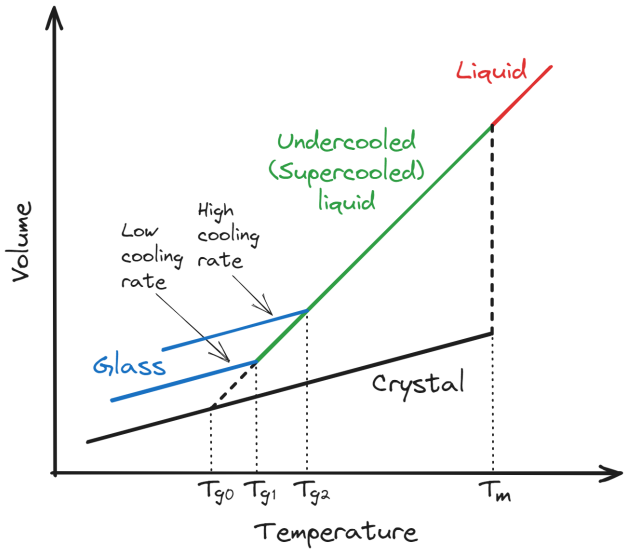

Figure 1.1: Schematic illustration of the change in volume with temperature for a normal crystalline and a glass-forming material. After [20].

rate, and heterogeneous nucleating agents [20].

Unlike ordinary metals, glass-forming metals can exhibit significant undercooling, facilitated by high cooling rates. The melt volume continues to decrease in this undercooled region, accompanied by an increasing viscosity. At a certain temperature well below T_m, the viscosity becomes so high that the liquid essentially freezes in place, leading to the formation of a solid glassy state. The temperature at which the undercooled liquid solidifies into glass is referred to as the glass-transition temperature T_g. However, since this transition to the glassy state occurs without a distinct phase transition like crystallization (i.e. the transition is continuous), there is no precisely defined temperature at which it takes place. Instead, there exists a temperature range in which the liquid transitions to glass, depending on the cooling rate and the method of glass preparation. The faster the alloy is cooled from the liquid state, the higher the values of the transition temperature T_g and density of the resulting glassy state. In metallic glasses, these values can differ by as much as 100 K, with corresponding density differences of up to 0.5 % [8].

Unlike crystalline solids, which transform into the liquid state at the melting temperature T_m upon heating, metallic glasses, similar to other types of glasses, can often revert to the undercooled liquid state without crystallization. This state is commonly referred to as the *supercooled liquid region* [20]. At T_x, a temperature higher than T_g, the supercooled liquid transitions into a crystalline phase or phases. The temperature interval between these temperatures, $\Delta T_x = T_x - T_g$, is referred to as the width of the supercooled liquid

region. The value of ΔT_x depends on the material and cooling rate and is typically used as an indicator of the thermal stability of the produced glass.

It is crucial to recognize that, for metallic glasses, there is no unique "structure" as there is for a crystal. The temperature at which the glass transition occurs determines the structure, and this temperature is a function of the cooling rate. Consequently, the properties of glassy materials are dependent on their history. Fortunately, the transport properties of interest are reasonably reproducible if the specimens are made with standard techniques and their temperature is not raised excessively. Nevertheless, care must be taken to ensure the quality of the amorphous phase.

The temperature dependence of volume exhibits a change in slope at the glass transition temperature, as seen in Figure 1.1. Other thermodynamic variables, such as entropy and enthalpy, are also continuous through the glass transition and exhibit a change in slope. Accordingly, at T_g, there is a discontinuity in the derivative of these variables, such as the coefficient of thermal expansion $\alpha_T = (\partial \ln V/\partial T)$, compressibility $\kappa_T = -(\partial \ln V/\partial p)_T$, and heat capacity $C_p = (\partial H/\partial T)_p$. It follows that calorimetric experiments are effective markers of the glass transition temperature. A useful method for monitoring the glass transition phenomena is by means of differential scanning calorimetry (DSC) or differential thermal analysis (DTA), in which the sample is heated at a constant rate, usually 5-40 $\mathrm{K\,min^{-1}}$, and changes in heat flow (DSC) or temperature (DTA) compared to an empty reference pan are measured.

A typical DSC curve for metallic glasses is illustrated in Figure 1.2(a). The curve displays three significant features. The glass transition temperature T_g is identified by a change in the slope of the baseline due to the increased heat capacity of the supercooled liquid. This is followed by one or multiple crystallization events starting at T_x, indicated by large exothermic peaks. Lastly, the onset of the alloy melting process is observed at T_m, which is endothermic in nature. Most alloys, unless they correspond exactly to the eutectic composition, possess a range of melting temperatures. Therefore, two temperatures should be identified: one at the start, T_m (the solidus temperature, sometimes denoted as T_s), and the other at the end of the melting process, T_l (the liquidus temperature). It is important to note that the values of T_x and T_g are not inherent to a given amorphous alloy but depend on the heating rate. Additionally, DSC/DTA curves of metallic glass can be more complex, with multiple glass and crystallization events.

An example of a DSC/DTA curve for metallic glass ribbons of one of the multicomponent TE–TL alloy systems studied in this work, $(\mathrm{TiZrNbCu})_{1-x}\mathrm{Co}_x$, is shown in Figure 1.2(b). These curves are quite similar to those of $(\mathrm{TiZrNbCu})_{1-x}\mathrm{Ni}_x$ and

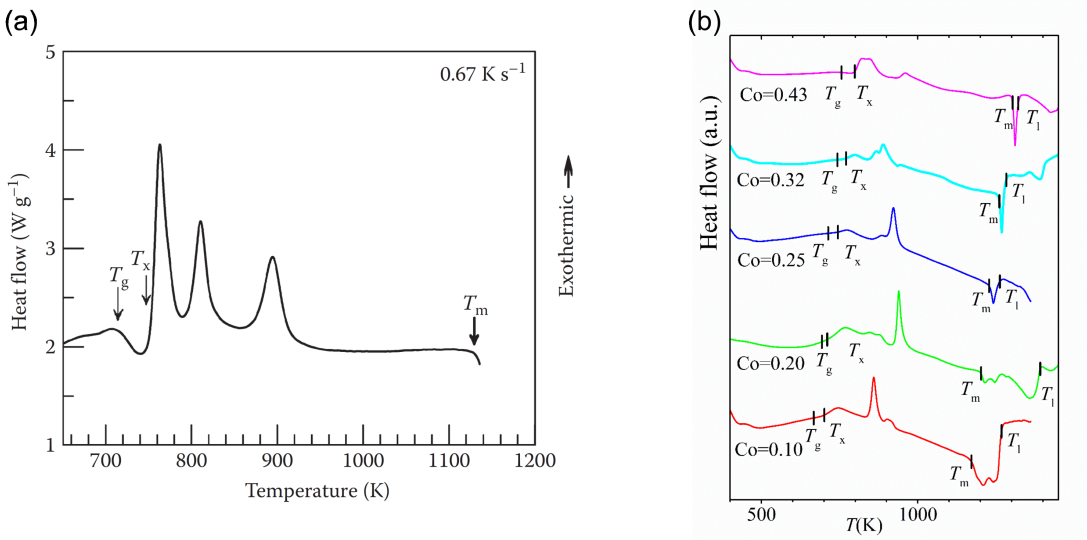

Figure 1.2: (**a**) Illustration of a typical DSC curve for a metallic glass alloy. (**b**) DSC/DTA curves of $(TiZrNbCu)_{1-x}Co_x$ metallic glass ribbons, obtained at a constant heating rate of 20 K min^{-1}. On heating, three processes can be observed: the glass transition temperature T_g, multiple crystallization processes starting at T_x, and the start and end of melting at the temperatures T_m and T_l respectively. (a) is reproduced from [20] and (b) from [21].

$(TiZrNbNi)_{1-x}Cu_x$ metallic glasses [21–23].

Before proceeding further, a few clarifications regarding terminology need to be made. Historically, in the literature, the terms *noncrystalline*, *amorphous*, and *glassy* have been used interchangeably to refer to similar random atomic arrangements in solid materials, with some researchers preferring one term over the others. Over the years, it has generally been accepted that *noncrystalline* is a generic term used to describe any solid material that lacks crystallinity. Moreover, a distinction has emerged between *glassy* and *amorphous* materials. A *glass* is any noncrystalline solid obtained through continuous cooling from the liquid state, while an *amorphous* solid is any noncrystalline material obtained by any other method [20]. In this thesis, the term *amorphous* will be used more generally to include any noncrystalline metal (or alloy) irrespective of the method of preparation, including metallic glasses.

Some researchers have also emphasized that the hallmark of a true glass is the presence of a glass transition temperature T_g. For a majority of melt-spun metallic glass ribbons that have been structurally proven noncrystalline, DSC/DTA curves do not display a clear glass transition. This is likely due to a small difference between T_g and T_x in these materials; the presence of T_g cannot be clearly observed next to a strong exothermic peak at T_x [20]. Therefore, in this thesis, no distinctions for metallic glasses based on the

observation of the glass transition temperature T_g will be made. It should be noted that amorphous alloys produced by non-solidification methods might not show the presence of T_g, as it is expected to be observed only during solidification from the liquid state [20].

1.2 Structure of amorphous metals

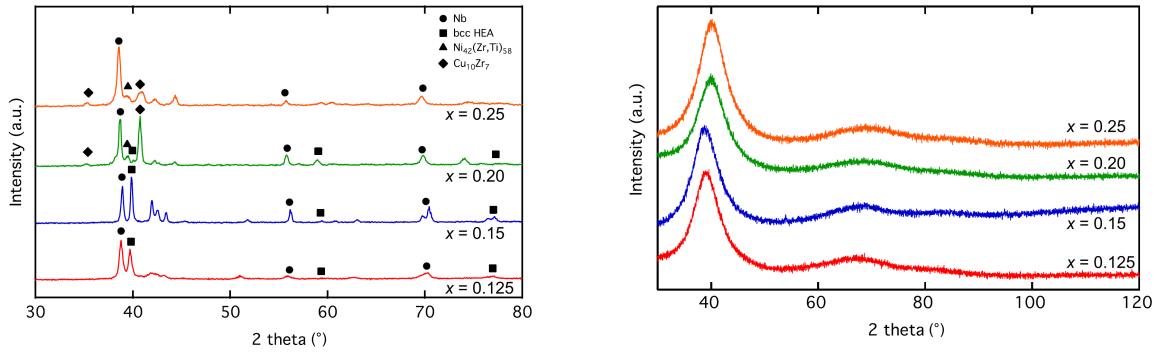

Figure 1.3: X-ray diffraction pattern for slow cooled polycrystalline samples (left panel) and melt spun amorphous ribbons (right panel) of $(TiZrNbCu)_{1-x}Ni_x$. Adapted from [24].

The absence of long-range order in amorphous metals is evident in their X-ray diffraction (XRD) patterns. Figure 1.3 displays the diffraction patterns of $(TiZrNbCu)_{1-x}Ni_x$ alloys in both crystalline and amorphous states. The diffraction pattern of crystalline samples (Figure 1.3, left) features multiple sharp peaks corresponding to Bragg reflections from parallel crystal lattice planes. In contrast, the amorphous diffraction pattern lacks sharp peaks, presenting only broad, diffuse halos; one large (though typically of smaller intensity than Bragg maxima in crystals) and several smaller ones. This pattern results from the short-range order in amorphous metals, as atoms cannot be truly randomly distributed. Factors such as a tendency for close packing, well-defined atomic sizes, and a closest distance of approach lead to distinct local structures.

The amorphous structure can be conceptualized as a relatively close-packed collection of nearly hard spheres, as illustrated in Figure 1.4(a). Surrounding any given atom, there is a ring of first neighbours at an average distance of d_1, a less well-defined ring of second neighbours at d_2, and so on. This short-range order plays an important role in shaping the electron density of states $N(E)$, which in turn affects other material properties.

The short-range order in a material can be visualized using the radial distribution function $g(r)$, which depicts the deviation from the average atom number density n_0 at a distance r from a reference atom. In other words, the number of atoms found in

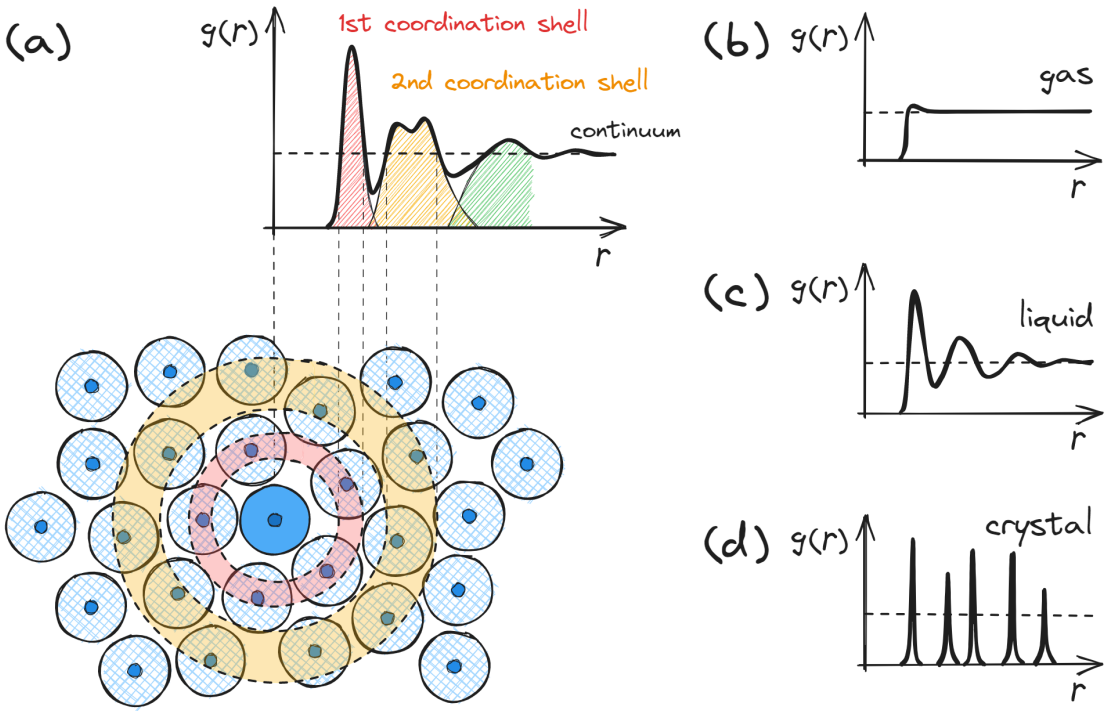

Figure 1.4: (**a**) Illustration of the close-packed structure in an amorphous metal and the corresponding radial distribution function $g(r)$. Illustrations of the radial distribution function $g(r)$ of (**b**) a gas, (**c**) a liquid, and (**d**) a crystal. After [25, 26].

the volume of a spherical shell with radius r and thickness dr is given by $n_0 g(r) 4\pi r^2 \mathrm{d}r$. As illustrated in Figure 1.4(a), $g(r) = 0$ at small values of r due to the finite sizes of atoms. As r increases, the first maximum emerges, corresponding to the nearest neighbour distance in the amorphous material. Further maxima appear as r increases, representing the second, third, and subsequent nearest neighbour distances; however, their intensities rapidly diminish and eventually converge to the average density $\lim_{r\to\infty} g(r) = 1$. For comparison, in gases, where near true randomness exists, $g(r) = 1$ for all values of r larger than the size of the atom or molecule, as seen in Figure 1.4(b). Conversely, in crystalline materials, $g(r)$ consists of a series of delta functions at distances characteristic of a given crystal lattice, as seen in Figure 1.4(d).

The radial distribution function $g(r)$ can be determined from the measured angular distribution of the intensity of elastically scattered X-ray or neutron beams $I(Q)$.[a] $g(r)$

[a]Here, $Q = 2Q_0 \sin\theta$ represents the magnitude of the scattering vector, where Q_0 is the magnitude of the wave vector of the incoming X-rays/neutrons, and Θ is the angle of incidence of the X-ray/neutron beam.

is calculated from the following equation [19, 26]:

$$g(r) = 1 + \frac{1}{2\pi^2 n_0} \int_0^\infty [S(Q) - 1] Q^2 \left(\frac{\sin Qr}{Qr} \right) \mathrm{d}Q \ , \tag{1.1}$$

where $S(Q)$ is the structural factor, which is determined from:

$$S(Q) = \frac{I(Q)}{N f^2} \ , \tag{1.2}$$

where N represents the number of atoms involved in the scattering process, and f denotes the atomic scattering factor, which depends on the atomic species involved, the type of scattering, and in the case of X-rays, the magnitude Q.[b]

The radial distribution function is also often reported in the form:

$$R(r) = 4\pi r^2 n_0 g(r) \ , \tag{1.3}$$

which describes the number density of atoms found at a distance r. This radial distribution function will have the peaks corresponding to the nearest neighbours, as seen in Figure 1.4, superimposed on the average density parabola $4\pi r^2 n_0$.

An example of the radial distribution function $R(r)$ determined from synchrotron-based high-energy XRD (HEXRD) measurements for one of the multicomponent TE–TL systems studied in this work, $(\mathrm{TiZrNbNi})_{1-x}\mathrm{Cu}_x$, is shown in Figure 1.5. The graph displays short-range order as described, featuring a large maximum whose centre shifts from 2.96 Å to 2.75 Å as x increases from 0.12 to 0.50. Furthermore, smaller maxima, that correspond to the second and third nearest neighbours, can be observed at greater radial distances r. The decrease in the first nearest neighbour distance with increasing Cu content is attributed to the replacement of larger TE atoms by smaller Cu atoms. The difference between $R(r)$ for $x = 0.05$ and $x > 0.05$, specifically the narrower and more pronounced first and third peaks, has been ascribed to the emergence of a nanocrystalline phase in the amorphous matrix for $x \leq 0.05$ [22].

By integration over the first maximum, it is possible to determine the average number

[b] For more detailed treatments of the radial distribution function and its calculation from various elastically scattered beams when multiple atomic species are involved, see, for example, Chapter 15 in [26] or Chapter 3 in [27].

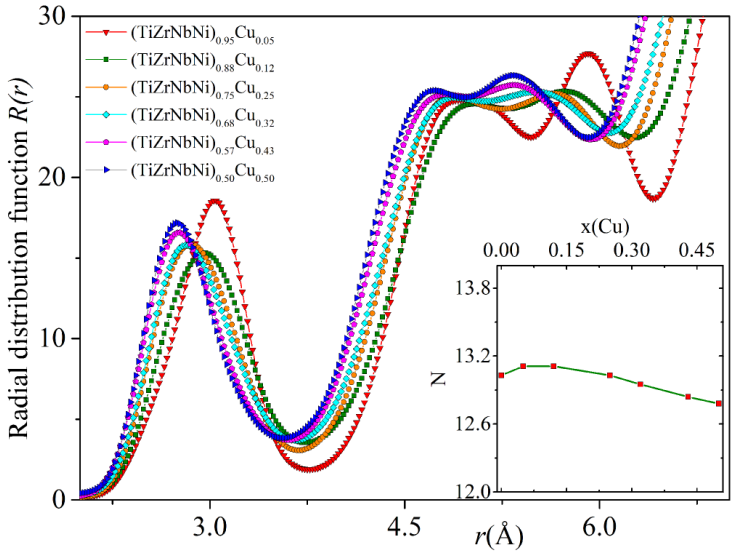

Figure 1.5: Radial distribution function od $(TiZrNbNi)_{1-x}Cu_x$ alloys. Inset: The corresponding average coordination number (average number of first nearest neighbour atoms). Reproduced from [22].

of first nearest neighbour atoms, i.e. the average coordination number:

$$N = \int_{\text{first maximum}} R(r)\mathrm{d}r \ . \tag{1.4}$$

The inset of Figure 1.5 shows that the coordination number does not change significantly with Cu content, suggesting no alteration in the short-range order for $(TiZrNbNi)_{1-x}Cu_x$ alloys, consistent with binary TE–Cu alloys [28, 29]. This contrasts with $(TiZrNbCu)_{1-x}Ni_x$ and $(TiZrNbCu)_{1-x}Co_x$ alloys, where N remains nearly constant with Ni and Co content before sharply increasing around $x = 0.43$ and $x = 0.25$, respectively [30].

It is worth noting that the standard XRD technique has limited sensitivity when detecting small volume fractions of crystalline phase within an amorphous matrix, especially if the crystals are nanocrystalline.[c] As a result, even if the XRD pattern displays only broad peaks, the material may still contain a small quantity of nanocrystals dispersed within the amorphous matrix.

[c]The measurement resolution increase with decreasing photon wavelength.

1.3 Electronic structure of TE–TL alloys

Prior to examining the transport properties of amorphous metals, it is beneficial to understand their electron band structure and density of states, as they play a crucial role in explaining various physical properties such as electron transport, Hall effect, superconductivity, magnetism, and more. Numerous techniques have been developed to investigate the electronic structure of crystalline metals, which rely on a long mean free path of conduction electrons (e.g., de Haas-van Alphen effect, radio-frequency size effect, cyclotron resonance, and high-field magnetoresistance). However, these techniques are inapplicable to amorphous materials, which generally exhibit short mean free paths. As a result, the principal technique for investigating the electron density of states in metallic glasses is photoemission (photoelectron) spectroscopy (PES).

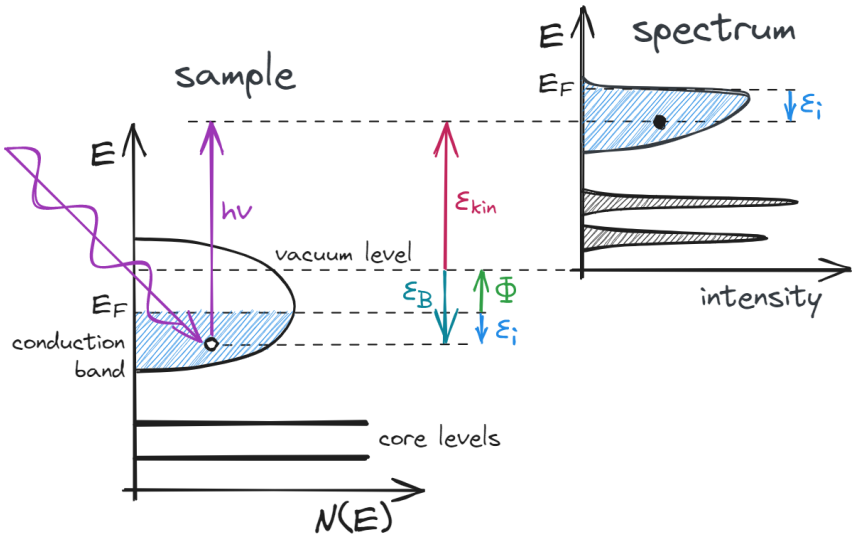

Figure 1.6: Schematic diagram of the photoemission process (photoelectron effect) used to measure the electron density of states of the conduction band and core levels. After [31].

In this technique, high-energy monochromatic photons are used to impart sufficient energy to eject electrons from their bound state in the sample into the vacuum. The kinetic energy of the emitted electrons can be measured to determine the band structure below the Fermi level, as depicted in Figure 1.6. The binding energy of the electron in the atom relative to the vacuum level ε_B is given by the difference between the energy of the incident photon $h\nu$ and the kinetic energy of the emitted electron ε_{kin}. By subtracting the work function Φ, the binding energy with respect to the Fermi level E_F can be calculated:

$$\varepsilon_i = h\nu - \varepsilon_{kin} - \Phi \, . \tag{1.5}$$

Assuming the number of emitted electrons at a given kinetic energy $\varepsilon_{\mathrm{kin}}$ is proportional to the density of states at the corresponding binding energy ε_{i}, this technique provides experimental information on the electronic density of states within the valence band as a function of binding energy [31]. However, this assumption is generally imprecise and the number of emitted electrons depends on the type of atom and band (s, p, d or f) and the photon energy involved [26]. In other words, the shape of the PES spectra generally depend on the energy of an incoming photon. Although corrections can be applied, they are often unknown or disregarded. In fact, this discrepancy can be exploited to distinguish the contributions of different types of bands and atoms. The technique is differentiated into ultraviolet photoemission (photoelectron) spectroscopy (UPS) and X-ray photoemission (photoelectron) spectroscopy (XPS) based on the energy of the incident photons.

In this work, we will focus on the electronic structure of TE–TL alloys. Figure 1.7 displays various examples of UPS spectra for binary TE–TL metallic glasses. Given the typically low contribution from sp-bands to the photoemission intensity, these spectra primarily reflect the density of states of d-electrons.

The prominent feature evident in these spectra is the presence of two well-defined peaks, which form the so-called "split band" structure. The peak situated closer to the Fermi level is attributed to the d-states of TE elements, whereas the deeper-lying peak is associated with the d-states of TL elements. Consequently, the density of states at the Fermi level is predominantly influenced by TE d-states. This assignment of the two peaks to TE and TL d-states was corroborated by Greig et al. on Cu–Zr alloys [32]. They successfully differentiated between the Cu and Zr d-bands, due to a more pronounced change in excitation probabilities of Zr d-electrons between photon energies of 40 eV and 120 eV compared to Cu d-electrons.

As seen in Figure 1.7(a), the density of states for both crystalline and amorphous alloys are similar, although fine details in the density of states of the crystalline alloy are smoothed out in the amorphous case. This suggests that the split band structure is not a result of the amorphous nature. The striking similarity can be largely attributed to the fact that the density of states of the d-electrons is determined by short-range interactions. In other words, short-range order, which is similar in amorphous and crystalline TE–TL alloys, is more important than long-range order when determining d-electron density of states [3].

Furthermore, hybridisation between the TE and TL d-bands leads to a shift in the position of the bands relative to their positions in the pure metal. The d-band of the

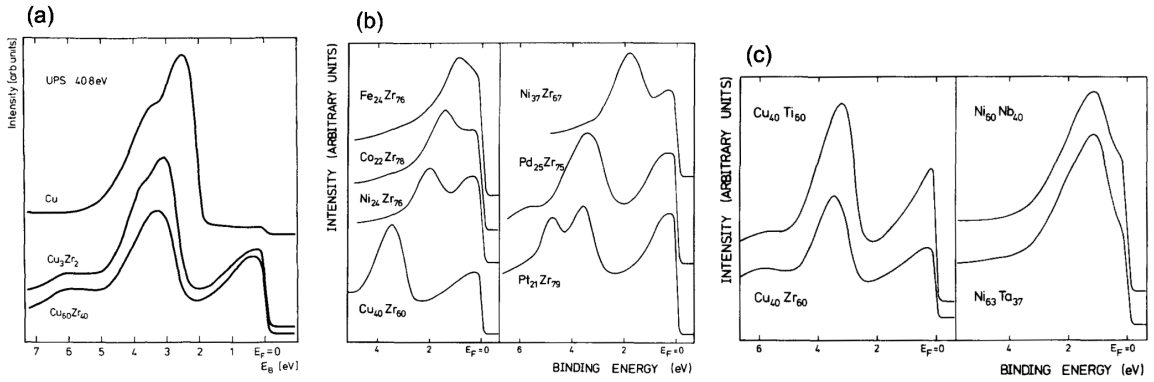

Figure 1.7: Comparison of UPS spectra for (**a**) amorphous $Cu_{60}Zr_{40}$, crystalline Cu_3Zr_2 and pure Cu metal; (**b**) Zr-based metallic glasses with different late transition metal; (**c**) Cu and Ni metallic glasses with various early transition metals. The (a) panel was reproduced from [33]; (b) and (c) panels were reproduced from [34].

late transition metal is pushed to higher binding energies, and that of the early transition metal component to lower binding energies [3].

For the same TE component, alloying with different TL elements of increasing atomic number (i.e. Fe→Co→Ni→Cu→Pd→Pt) causes the d-band splitting to increase, as seen in Figure 1.7(b). However, the band structure remains almost unchanged if the TL component is kept constant while the TE element is varied within the same group, as shown in Figure 1.7(c). Additionally, as the concentration of TL elements increases, the binding energy of the TL d-band decreases, i.e. shifts towards the Fermi level, while the peak width increases [34]. Thus, at a certain crossover concentration the Fermi level is expected to shift from the TE d-band to the TL d-band [35].

Figure 1.8 shows the UPS spectra for the three quinary alloy systems studied in this work, $(TiZrNbNi)_{1-x}Cu_x$, $(TiZrNbCu)_{1-x}Ni_x$ and $(TiZrNbCu)_{1-x}Co_x$, all with the same concentration $x = 0.43$, as well as for the equiatomic TiZrNbCuNi for comparison. Contrary to the binary alloys with two peaks, these quinary alloys display three peaks in their UPS spectra. A similar shape of the UPS spectra had been observed in ternary TE–TL alloys.

In $(Ni_{0.33}Zr_{0.67})_{0.85}X_{0.15}$ alloys, the inclusion of a TL element (X=Fe, Co, Cu) led to the appearance of a third peak associated with the d-band of the added element. In contrast, the addition of a TE element (X=Ti) merely altered the height and width of the TE (Zr) peak at the Fermi level [36], mirroring the change observed when changing the TE element in binary TE–TL alloys, as observed in Figure 1.7(c). Similarly, in our quinary alloys, the peak at the Fermi level originates from the d-bands of TE elements (Ti, Zr and Nb),

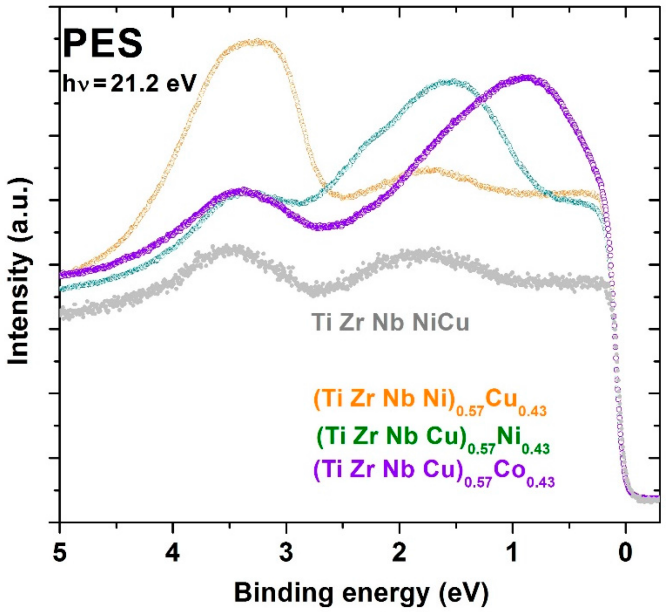

Figure 1.8: Photoemission spectra of TiZrNbNiCu, $(\mathrm{TiZrNbNi})_{0.57}\mathrm{Cu}_{0.43}$, $(\mathrm{TiZrNbCu})_{0.57}\mathrm{Ni}_{0.43}$, and $(\mathrm{TiZrNbNi})_{0.57}\mathrm{Cu}_{0.43}$. The Fermi level E_F is located at the binding energy value of zero. Reproduced from [30].

while the two remaining peaks correspond to the two TL elements. The peak at higher binding energies, situated around 3.5 eV, corresponds to the Cu d-band, while the peak closer to the Fermi level is attributed to either the Ni or Co d-band [21, 22, 30, 37, 38].

In accordance with binary TE–TL alloys, the peak corresponding to the Cu d-band in $(\mathrm{TiZrNbNi})_{1-x}\mathrm{Cu}_x$ alloys shifts only slightly towards the Fermi level with increasing concentration x. In contrast, in $(\mathrm{TiZrNbCu})_{1-x}\mathrm{Ni}_x$ alloys, the peak associated with the Ni d-band exhibits a considerable shift from about 1.85 eV for $x = 0.20$, to 1.5 eV for $x = 0.43$, and in $(\mathrm{TiZrNbCu})_{1-x}\mathrm{Co}_x$ alloys, the Co d-band peak demonstrates an even more pronounced shift from 1.3 eV for $x = 0.20$ (not show here, see [21]), to 0.8 eV for $x = 0.43$.

1.4 Transport properties

This section offers a brief overview of experimental findings and relevant theoretical models regarding the Hall effect, resistivity, magnetoresistance, and superconductivity in amorphous non-magnetic TE–TL alloys.

1.4.1 Hall effect

Hall coefficient measurements have generally showed either no or only a small temperature dependence (a few precent) for most non-magnetic amorphous alloys [3, 39]. This small temperature dependence has been attributed [40] to enhanced electron-electron interactions (EEI; see subsection 1.4.2.2) which result in a temperature dependence in the form of [41]:

$$\frac{\Delta R_{\mathrm{H}}}{R_{\mathrm{H}}} = 2\frac{\Delta\rho^{\mathrm{EEI}}}{\rho} \propto -\sqrt{T}\,. \tag{1.6}$$

This dependence is intriguing because it predicts that the sign of the temperature change of the Hall coefficient $\Delta R_{\mathrm{H}}(T)$ is opposite to the sign of the Hall coefficient itself. It decreases (increases) with temperature for positive (negative) Hall coefficients, assuming a negative temperature coefficient of resistivity, which is the case in high resistivity amorphous alloys.

This behaviour has been observed in a series of TE–TL alloys [40, 42]. However, it is important to note that these changes are small, in accordance with the change in resistivities which are typically a few precent. This makes it potentially challenging to accurately measure these differences in the Hall coefficient due to the small Hall signals. Furthermore, it has been shown that small amounts of crystallinity in the sample can produce strong temperature-dependent Hall coefficients [43].

An intriguing property of Hall effect in amorphous transition metals is the widespread appearance of positive (hole-like) values of the Hall coefficient R_{H}. This is evident in Figure 1.9 for some binary TE–TL alloys. Several observations can be made about the Hall coefficient values in non-magnetic TE–TL alloys.

At higher TE concentrations, R_{H} is positive. However, as the concentration x of the TL element increases, the Hall coefficient changes sign at a certain critical concentration x_{c}. This critical concentration tends to increase with the atomic number of the TL element (following the order Co→Ni→Cu). For example, the critical concentrations are found to be approximately 0.32 for $Zr_{1-x}Co_x$, 0.45 for $Zr_{1-x}Ni_x$ and 0.8 for $Zr_{1-x}Cu_x$ [35].

This crossover has been associated with the shift in the character of the d-band at the Fermi level from TE-dominated to TL-dominated [35]. This correlation between the position of the TL d-band and the R_{H} values can be observed by comparing Figure 1.6 with Figure 1.9. As the TL d-band moves towards the Fermi level, either through an increase in the atomic number of the TL element or an increase in TL concentrations, the values of the Hall coefficient decrease and ultimately change sign. This crossover tends to occur earlier in TL elements with lower atomic numbers, since their d-band is located

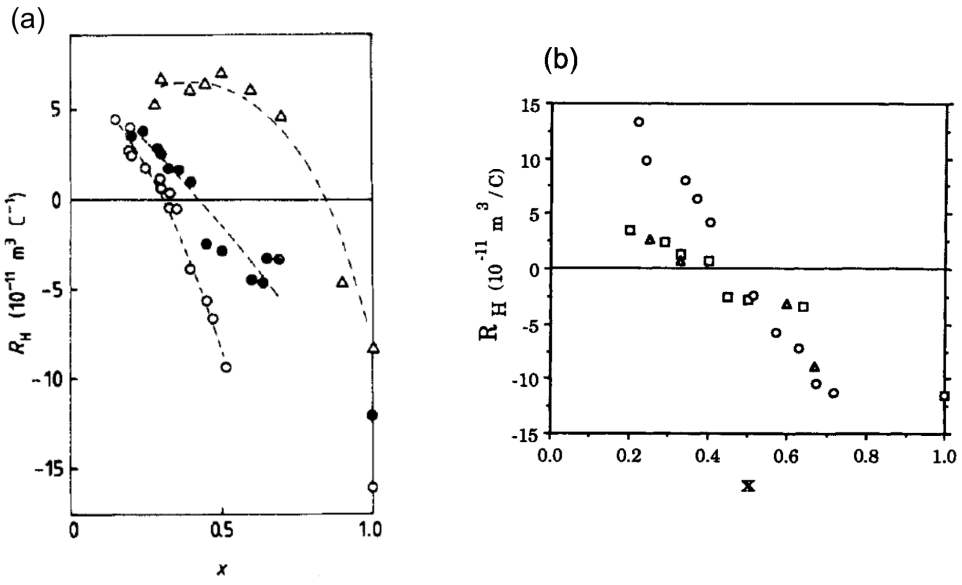

Figure 1.9: Room-temperature Hell coefficients R_{H} for (**a**) $Zr_{1-x}Cu_x$ (open triangles), $Zr_{1-x}Ni_x$ (closed circle) and $Zr_{1-x}Co_x$ (open circles); and (**b**) $Ti_{1-x}Ni_x$ (open circles), $Zr_{1-x}Ni_x$ (open squares) and $Hf_{1-x}Ni_x$ (open triangles). Panel (a) was reproduced from [44] and panel (b) from [39].

closer to the Fermi level. On the other hand, in TE-Cu the d-band of Cu is always situated far below the Fermi level, and in pure Cu, it is the s-states that dominate the Fermi level. Therefore, the crossover occurs when the Fermi level becomes dominated by sp-states of Cu.

Interestingly, the crossover concentration seems to be relatively insensitive to whether the TE element belongs to the 3-d, 4-d, or 5-d series [29, 39, 44], as seen in Figure 1.9(b). However, limited experimental data suggest that the critical concentration increases with the atomic number (group) of the TE element (e.g. Zr→Nb) [39, 45]. Lastly, the positive values of R_{H} tend to decrees with higher series of the TE element (from 3d to 4d to 5d) [3, 29, 44, 46].

The observed positive Hall coefficients contradict the negative values predicted by the nearly free electron model, commonly used for simple metals. In this model, the Hall coefficient is given by:

$$R_{\mathrm{H}} = -\frac{1}{ne}\,, \tag{1.7}$$

where n denotes the density of charge carriers (electrons) per unit volume. Even when accounting for two types of charge carriers, such as highly mobile s-electrons and sluggish d-electrons with charges $q_{1,2}$, mobilities $\mu_{1,2}$, and concentrations $n_{1,2}$, the Hall coefficient,

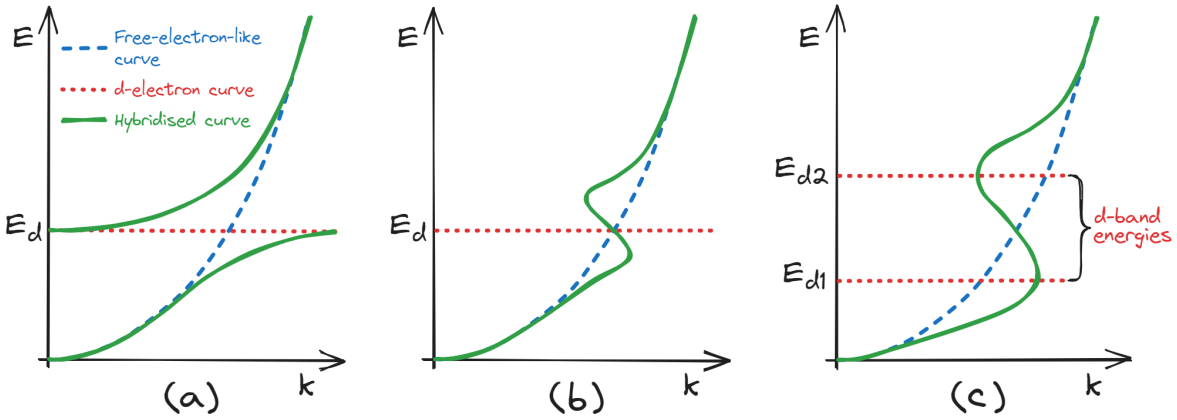

Figure 1.10: Illustration of s-d hybridisation with a parabolic free-electron-like s-electron curve and an infinitely narrow d-electron band (**a**) without and (**b**) with damping. (c) Illustration of a more realistic s-d hybridised curve from an well-defined d-band. After [8].

given by:

$$R_{\mathrm{H}} = \frac{q_1 n_1 \mu_1^2 + q_2 n_2 \mu_2^2}{\left(|q_1 n_1 \mu_1| + |q_2 n_2 \mu_2|\right)^2} \,, \tag{1.8}$$

still remains negative, since the electron charges are negative ($q_1 = q_2 = -e$).

To date, a consensus has not been reached on the explanation for the occurrence of the positive Hall coefficient in transition-metal-based amorphous alloys. Various explanations have been suggested thus far [3]. One of the more widely recognized explanations proposes that the positive Hall coefficient results from an "S"-shaped $E(k)$ dispersion curve, which appears due to s-d hybridization, as initially proposed by G. F. Weir et. al. [47]. The outline of this model is as follows:

With a parabolic free-electron-like dispersion curve ($E(k) \propto k^2$) of s-electron states and an infinitely narrow band of d-electron states, as illustrated in Figure 1.10(a). Where the s- and d-curves intersect, a phenomenon known as hybridization may occur. A quasi-free electron with an energy not too far from that of a d-state can be thought of as spending part of its time in that state, i.e. it is no longer purely s-like but takes on some d-character, and its dispersion curve $E(k)$ is modified accordingly. There are no longer separate s- and d-like electrons but hybrids of intermediate character.

The illustration without damping and a perfectly narrow band is unrealistic. When damping is included to account for electron scattering, the sharp change at the d-band density E_d is spread over a range of energies, as illustrated in Figure 1.10(b). This results in an "S"-shaped dispersion curve featuring a region with a negative slope around E_d. Furthermore, in real alloys, the d-band spans a range of energies, and due to heavy

scattering, the associated wavefunctions are heavily damped. This leads to a more realistic shape, as shown in Figure 1.10(c).

The crucial outcome of this s-d hybridization is the emergence of a region of energies where, due to the negative slope of the dispersion curve, electrons have negative group velocities. It means that when the Fermi level resides within this range, the electrons that govern transport will possess negative group velocities. For simple metals with a spherical Fermi surface this leads to a positive Hall coefficient [3, 48]:

$$R_H = -\frac{\frac{\partial E(k)}{\partial k}}{\left|\frac{\partial E(k)}{\partial k}\right|}\frac{1}{ne}\,. \tag{1.9}$$

Following this, Nguyen-Manh et. al. [49] demonstrated that the Hall coefficient is proportional to the derivative of the density of states at the Fermi level, given by:

$$R_H = \frac{-\alpha}{2eN_s^2(E_F)}\left.\frac{dN_s(E)}{dE}\right|_{E=E_F}\,, \tag{1.10}$$

where α is a constant between 1-3 and $N_s(E)$ is the density of the hybridized s-states. Once again, s-d hybridization leads to negative values of $dN_s(E)/dE$ and, consequently, a positive Hall coefficient.

Not all d-states participate in the hybridization, so care must be taken to account for the un-hybridized d-states contribution to the Hall effect. Although the mobility of d-electrons is smaller than that of s-electrons, this can be compensated by their higher concentration. Calculations [3] have shown that while the contribution of d-electrons to conductivity can be significant, their contribution to the Hall effect would be small and negative.

Additionally, anomalous contributions to the Hall effect, such as skew-scattering and the side-jump effect that involve spin-orbit interactions, have been proposed to contribute to and account for the positive Hall coefficient in non-magnetic amorphous alloys [3, 39, 44, 50, 51]. Skew scattering can lead to a positive contribution to the Hall effect, but estimates of its size imply that this contribution would be negligible [3, 51]. For the side-jump mechanism, theoretical models have not definitively established whether it contributes to the Hall effect in amorphous systems at all, or whether its contribution is sizeable enough to shift the negative free electron value of the ordinary Hall coefficient to a positive value [39, 51].

More recently, a comprehensive experimental and theoretical review of the anoma-

lous Hall effect, including skew-scattering and side-jump contributions to the anomalous Hall conductivity (resistivity), was presented by N. Nagaosa et. al. [52]. From the experimental data, three regimes were identified: the high conductivity regime ($\sigma_{xx} > 10^6\,\Omega^{-1}\,\mathrm{cm}^{-1}$), where skew-scattering with $\sigma_{xy} \propto \sigma_{xx}$ scaling dominates;[d] the good-metal regime ($10^4\,\Omega^{-1}\,\mathrm{cm}^{-1} < \sigma_{xx} < 10^6\,\Omega^{-1}\,\mathrm{cm}^{-1}$), where intrinsic Barry phase related anomalous Hall effect and side-jump dominate, and σ_{xy} is roughly independent of σ_{xx}; and finally, the bad-metal regime ($\sigma_{xx} < 10^4\,\Omega^{-1}\,\mathrm{cm}^{-1}$), in which the anomalous Hall conductivity scales as $\sigma_{xy} \propto \sigma_{xx}^{1.6-2.0}$.[e] The origin of this particular scaling has not been identified.

According to these findings, neither skew-scattering nor the side-jump effect should be observed in amorphous alloys with resistivities $>100\,\mu\Omega\,\mathrm{cm}$ ($\sigma_{xx}<10^4\,\Omega^{-1}\,\mathrm{cm}^{-1}$), which is the case for most TE–TL alloys. It is important to note that, as of now, there is no clear evidence supporting the applicability of either the s-d hybridization or the spin-jump mechanism to TE–TL alloys. Further research, experimental and theoretical, is needed to better understand the underlying mechanisms that contribute to the positive Hall coefficient in these materials.

1.4.2 Resistivity

The resistivity of amorphous metals is significantly higher than that of their crystalline counterparts, ranging from 20-1000 $\mu\Omega\,\mathrm{cm}$ [26], with only minor changes in resistivity occurring within the temperature range of 2-300 K. The highly disordered nature of these materials makes this observation unsurprising. What is intriguing, however, is that the temperature coefficient of resistivity (TCR) can be either positive or negative, a characteristic rarely observed in crystalline metals. Furthermore, the values of the TCR appears to be linearly (anti)correlated with resistivity, an empirical relationship first reported by J. H. Mooij in 1973. [53], and subsequently known as the Mooij correlation. Amorphous alloys with resistivities below $150\,\mu\Omega\,\mathrm{cm}$ typically exhibit a positive TCR, while those with resistivities above this threshold display a negative TCR.

To describe the temperature dependence of resistivity of metallic glasses, nearly free electron models have been developed, such as a generalization of the Faber-Ziman theory, originally formulated to describe the resistivities of simple liquid metals and alloys, to account for the inelastic electron-phonon scattering that becomes significant at tempera-

[d] $\sigma_{xx} = j_x/E_x$ is the conductivity (magnetoconductivity) of the material and $\sigma_{xy} = j_x/E_y$ describes the appearance of an electric field perpendicular to the current, i.e. the Hall effect.

[e] Assuming $\rho_{xy} \ll \rho_{xx}$, which is generally satisfied in metallic glasses, the anomalous contribution to Hall resistivity scales as $\rho_{xy} \sim \rho_{xx}^{0.0-0.4}$

tures below the Debye temperature Θ_D [26]. These models have had some success when applied to metallic glasses with resistivities low enough that the electron mean free path l is significantly longer than both interatomic distances and the electron wavelength λ, i.e. $k_F l \gg 1$, where $k_F = 2\pi/\lambda$ is the Fermi wavevector. These criteria tend to be satisfied only for "simple" alloys without d- and f-states near the Fermi level. In the case of amorphous transition metal alloys, resistivities are typically $\gtrsim 150\,\mu\Omega\,\mathrm{cm}$, and the electron mean free path, in terms of the semiclassical theory, is comparable to its wavelength, $k_F l \gtrsim 1$. For these alloys, also called strong scattering alloys, the Faber-Ziman and other models based on the Boltzmann transport theory cannot explain the temperature dependence of resistivity [54], and quantum corrections to semiclassical theories need to be considered [3, 55].

In the Boltzmann transport theory, electron propagation between scattering events is treated as a classical free particle trajectory, meaning there is no interference between electron wavefunctions at different points along their path, and the rare scattering events are considered independently. However, when scattering events are not rare, interference effects between electron wavefunctions scattered from different scattering centres along their path must be taken into account. As a result, conduction electrons should be treated as waves that propagate through the material and can interfere with themselves and each other. These interference effects provide the first-order corrections to the semiclassical theory and will be discussed in the following two subsections, before we turn to describing the temperature dependence of resistivity in binary TE–TL alloys according to the present consensus in the literature, in subsection 1.4.2.3.

1.4.2.1 Weak localization

As electrons move through a system, they experience a series of random scattering events, resulting in a random, diffuse motion of electrons. These scattering events can be divided into those that maintain and those that break phase coherence between the incident and scattered electron wavefunctions. The first type involves elastic scattering on static disorder, in which the electron preserves its energy and thus the time variation of the wavefunction ($\exp(i\varepsilon t/\hbar)$). The mean time between elastic scatterings is denoted as τ_e. The scattering processes that break phase coherence include inelastic electron-phonon and electron-electron collisions, as well as spin-flip scattering by magnetic impurities. The time between these processes, where phase coherence is maintained, is known as the *phase-breaking* or *dephasing* time and is denoted by τ_φ.

Classical transport theory can be applied when $\tau_\varphi < \tau_e$, i.e. when there is no phase

coherence between incident and scattered wavefunctions and they do not interfere. However, in a disordered system, where elastic scattering events are frequent and when the temperature is low enough that inelastic scattering processes are rare, phase coherence is maintained for a time $\tau_\varphi \gg \tau_\mathrm{e}$, and quantum interference between scattered wavefunctions can occur.

Consider an electron that propagates diffusely from point $\mathbf{R_1}$ to point $\mathbf{R_2}$, as seen in Figure 1.11. Classically, the probability $P_{\mathbf{R_1}\to\mathbf{R_2}}$ of reaching point $\mathbf{R_2}$ is given by the sum of probabilities of all possible paths between $\mathbf{R_1}$ and $\mathbf{R_2}$. However, if all scattering processes are elastic, i.e. phase coherence is maintained along paths between $\mathbf{R_1}$ and $\mathbf{R_2}$, we have to consider interference and sum up the probability amplitudes A_i of all paths. The probability is then given as the square modulus of this sum:

$$P_{\mathbf{R_1}\to\mathbf{R_2}} = \left|\sum_i A_i\right|^2 = \sum_i |A_i|^2 + \sum_{i\neq j} A_i A_j^* \,, \tag{1.11}$$

The first term represents the classical probabilities, and the second term accounts for interferences, which are excluded in the classical treatment.

The phase change along a path is given by the line integral [56]:

$$\Delta\varphi = \int_{\mathbf{R_1}}^{\mathbf{R_2}} \mathbf{k}\cdot \mathrm{d}\mathbf{l} \,. \tag{1.12}$$

Since the lengths of the paths between $\mathbf{R_1}$ and $\mathbf{R_2}$ differ substantially, so will the final phase differences between them. When summing over all possible path combinations the interference term would generally average to zero, since there would be a random phase difference between them. Even when considering quantum interference effects, there appears to be no change in the classical conductivity.

There exists, however, a special class of electron trajectories that contain closed loops, as illustrated in Figure 1.11, where interference effects appear. When two electron paths traverse a closed loop in the opposite directions and all processes are elastic, the associated partial electron wavefunctions accumulate the same phase change and therefore interfere constructively.[f] Since, the two paths are in phase and possess the same probability amplitude A, the probability that an electron returns to its starting position $\mathbf{O}$ in a closed loop after a series of elastic scattering events is: $W = 2\,|A|^2 + 2AA^* = 4\,|A|^2$, which is

[f] The two paths can be transformed into each other by simultaneously reversing $\mathbf{k}$ and $\mathrm{d}\mathbf{l}$ in Equation (1.12); $\mathbf{k}\to-\mathbf{k}$ and $\mathrm{d}\mathbf{l}\to-\mathrm{d}\mathbf{l}$.

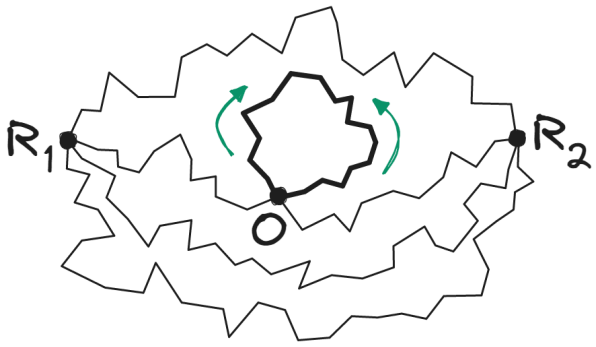

Figure 1.11: Illustration of various diffusive paths between point $\mathbf{R_1}$ and point $\mathbf{R_2}$, including a path with a closed loop. **O** marks the starting/ending point of the path around the closed loop.

twice as likely as in the classical treatment $W_{\text{classical}} = 2\,|A|^2$. An enhanced probability of an electron returning to the point it has left, i.e. enhanced backscattering, increases the time the electron spends at this point, and therefore decreases the probability of finding the electron at point $\mathbf{R_2}$, the point of observation. As a result, the material exhibits a lower conductivity (higher resistivity) than theories neglecting this interference. This phenomena is referred to as *weak localisation* (WL).

We can estimate the magnitude of this correction to the conductivity. Assuming that electrons propagate ballistically for times shorter than the elastic mean free time τ_{e}, and diffusively for longer times, the probability $p(r,t)$ that the electron reaches a distance r in time $t > \tau_{\text{e}}$ can be obtained by solving Fick's second law for diffusion:

$$\frac{\partial p(r,t)}{\partial t} = D\nabla^2 p(r,t)\ , \tag{1.13}$$

where D is the diffusion coefficient. The normalized solution is:

$$p(r,t) = (4\pi Dt)^{-3/2}\mathrm{e}^{-r^2/4Dt}\ . \tag{1.14}$$

The electron can interfere with itself if it returns to the origin $r = 0$ in some time t. The probability for a point-like object to return precisely to the origin is zero. However, we can view an electron as a wave packet with a dimension of its wavelength λ. Therefore, travelling ballistically with the Fermi velocity v_{F}, an electron in some time $\mathrm{d}t$ sweeps a volume $\lambda_{\text{F}}^2 v_{\text{F}}\mathrm{d}t$. Then the probability for the electron to find itself within this volume around the origin in time $\mathrm{d}t$ is given by:

$$p(r=0,t)\,\lambda^2 v_{\text{F}}\mathrm{d}t = \frac{\lambda^2 v_{\text{F}}}{(4\pi Dt)^{3/2}}\ \mathrm{d}t\ . \tag{1.15}$$

To estimate the enhanced probability of backscattering, we integrate the return probability (1.15) over the time the electron wavefunction remains coherent. The diffusive motion sets in after the elastic mean free time τ_e. For times shorter than the elastic mean free time τ_e, the propagation is ballistic, and there is no chance of return. On the other end, after a phase-breaking time τ_φ, the partial wavefunctions are no longer coherent and cannot interfere. The relative change in conductivity (resistivity)[g] is proportional to this return probability:

$$-\frac{\Delta\rho}{\rho_0} \propto \frac{\Delta\sigma}{\sigma_0} \propto -\int_{\tau_e}^{\tau_\varphi} \frac{\lambda^2 v_F}{(4\pi D t)^{3/2}}\, \mathrm{d}t \propto -\frac{1}{(k_F l)^2}\left[1-\left(\frac{\tau_e}{\tau_\varphi}\right)^{1/2}\right], \tag{1.16}$$

where expressions for the diffusion coefficient $D = v_F^2 l/3$ and electron wavelength $\lambda = 2\pi/k_F$ were used, and $l = v_F\tau_e$ is the mean free path between elastic scattering events, which the electron traverses ballistically.

From Expression (1.16), we observe that, as expected, the interference effect vanishes when the phase-breaking time τ_φ is reduced to equal the elastic scattering time τ_e. Furthermore, the magnitude of the effect is determined by the factor $(k_F l)^2$. If this factor is large, signifying that the mean free path of the electrons is large compared to their Fermi wavelength, the effect is vanishingly small, and vice versa. Since the elastic scattering time τ_e is temperature-independent, the temperature dependence of the WL contribution to conductivity will be due to the temperature dependence of the phase breaking time τ_φ.

In the preceding discussion, the electron's spin was not considered. This is a valid approach provided that the electron's spin state remains conserved during elastic scattering events. However, this will no longer be the case, if elastic scattering of conduction electrons involves spin-orbit coupling, as this interaction can induce a change to the electron's spin state.

The spin-orbit interaction during an elastic scattering event depends on the product [8, 57]:

$$\mathbf{k}\times\mathbf{k}'\cdot\boldsymbol{\sigma}\,, \tag{1.17}$$

where $\mathbf{k}$ and $\mathbf{k}'$ are the wave vectors of the electron before and after scattering, respectively, and $\boldsymbol{\sigma}$ denotes the Pauli spin matrix. Given that the partial waves traverse the loop in opposite directions the induced changes in the spin state will be different. As a result, the spin states of the partial waves may no longer coincide when they return

[g] Assuming $\rho_{xx} \gg \rho_{xy}$ it follows that $\rho_{xx} \approx 1/\sigma_{xx}$; additionally if $\Delta\rho_{xx} \ll \rho_{xx}$ it follows that $\Delta\rho_{xx}/\rho_{xx} \approx -\Delta\sigma_{xx}/\sigma_{xx}$. Subscript "xx" is omitted from the main text.

to the starting position. Indeed, their spin states could assume opposite signs, leading to destructive interference of the probability amplitudes. This destructive interference reduces the probability of a return to the starting position below the classical term, and thus enhancing the probability of forward scattering. Under conditions where the spin-orbit interaction is strong enough, this destructive interference could lead to an increase in conductivity (a reduction in resistivity) relative to semiclassical Boltzmann values. This phenomena is known as *weak antilocalization* (WAL).

If the initial and final states of the electron are determined by wavefunctions φ_α and φ_β (α and β are spin indices), respectively, the interference term has the form $C = A_1 A_2^* = 1/2(\varphi_\alpha^{(1)}\varphi_\beta^{(2)}\varphi_\beta^{(1)*}\varphi_\alpha^{(2)*})$ [41]. Making use of the eigenstate functions of the total spin for a two-electron system:

$$\begin{aligned} \psi_{1,\pm1} &= \varphi_\pm^{(1)}\varphi_\pm^{(2)} \,, \\ \psi_{1,0} &= \frac{1}{\sqrt{2}}\left(\varphi_+^{(1)}\varphi_-^{(2)} + \varphi_-^{(1)}\varphi_+^{(2)}\right) \,, \\ \psi_{0,0} &= \frac{1}{\sqrt{2}}\left(\varphi_+^{(1)}\varphi_-^{(2)} - \varphi_-^{(1)}\varphi_+^{(2)}\right) \,, \end{aligned} \tag{1.18}$$

this interference term can be reformulated as:

$$C = \frac{1}{2}\left(|\psi_{1,+1}|^2 + |\psi_{1,0}|^2 + |\psi_{1,-1}|^2 - |\psi_{0,0}|^2\right) \tag{1.19}$$

The wavefunction $\psi_{0,0}$ corresponds to the singlet combination of the initial and final spin configurations, with total spin $j = 0$. The tree wavefunctions $\psi_{1,m}$ correspond to the triplet combination with total spin $j = 1$ and projections $m = +1, 0, -1$. In the absence of spin-orbit coupling, all four components are numerically identical [8] and the interference term $C = |\psi_{0,0}|^2$ is positive and equals the classical term, as obtained in the weak localization discussion where the spin variable was disregarded.

Calculations, as outlined in [41, 58], demonstrate that the triplet configurations decay due to spin-orbit scattering with a characteristic time τ_{so}, called the spin-orbit time, which depends on both the strength of the spin-orbit coupling and the concentration of such scattering centres. On the other hand, the singlet configuration remains unaffected by spin-orbit scattering and decays in time τ_φ. In other words, the triplet state $\psi_{1,m}$ contains the information on the electron's spin state, which is gradually lost over time τ_{so} as a consequence of random spin-orbit scattering events.

Accounting for the electron's spin introduces a correction to the integral in Equation

1.16, in the form of [41]:

$$-\frac{\Delta\rho}{\rho_0} \propto \frac{\Delta\sigma}{\sigma_0} \propto -\int_{\tau_e}^{\tau_\varphi} \frac{\lambda^2 v_F}{(4\pi D t)^{3/2}} \left(\frac{3}{2}e^{-t/\tau_{so}} - \frac{1}{2}\right) \, dt \, . \tag{1.20}$$

The first term within the parentheses, with the exponential factor, describes the decay of the triplet form due to spin-orbit scattering, or in other words, the probability that the phase coherence in the triplet state is preserved at some time t. The second, negative, term stems from the singlet's contribution to interference.

For $\tau_e \ll \tau_\varphi \ll \tau_{so}$, we can approximate the exponential factor as $\exp(-t/\tau_{so}) \approx 1$ during the time interval of phase coherence, and the integral reverts to the form in Equation 1.16 for WL, meaning there is effectively no spin-orbit scattering. However, for $\tau_e \ll \tau_{so} \ll \tau_\varphi$, the first term decays rapidly and the second term leads to an increase in conductivity above the semiclassical Boltzmann value, i.e. to the aforementioned weak antilocalization.

Phase breaking primarily occurs due to inelastic electron-electron and electron-phonon scattering events. Hence, the phase-breaking time τ_φ can, in a first approximation, be identified with the inelastic scattering time $\tau_\varphi \simeq \tau_{in}$. Assuming that both the inelastic and spin-orbit scattering times considerably exceed the elastic scattering time, $\tau_{in}, \tau_{so} \gg \tau_e$. A comprehensive analysis of the interference effects in three dimensions using the diagrammatic technique [59] provides the temperature-dependent component of the conductivity change due to WL, including the spin-orbit interaction (WAL), up to the leading order in τ_{in}/τ_e and τ_{so}/τ_e, as:

$$\Delta\sigma^{WL}(T) = \frac{e^2}{2\pi^2\hbar D^{1/2}} \left[3\left(\frac{1}{\tau_{so}} + \frac{1}{4\tau_{in}}\right)^{1/2} - \left(\frac{1}{4\tau_{in}}\right)^{1/2}\right] \, . \tag{1.21}$$

The diffusion coefficient, which depends on the elastic scattering time τ_e, and the spin-orbit time τ_{so}, are temperature independent. On the other hand, the inelastic scattering time is polynomially dependent on temperature $\tau_{in} \propto T^{-p}$, where p is a positive constant.

In a low-temperature region where $\tau_{so} \ll \tau_{in}$, the contribution from $1/\tau_{so}$ dominates the conductivity change, leading to an increase in total conductivity (WAL). In this region as the temperature increases, the second term in the square brackets of Equation (1.21) increases more rapidly than the first. This leads to a reduction in conductivity, suppression of the WAL effect, i.e. a positive temperature coefficient of resistance. This trend continues until a minimum conductivity in Equation (1.21) is reached at $\tau_{in} \approx 2/\tau_{so}$. Beyond this point, further increases in temperature (and in turn, the inelastic scattering

time τ_{in}) result in an increase in conductivity, as the WL effect continues to be suppressed, i.e. a negative TCR.

Additionally, scattering on magnetic impurities, not discussed so far, will result in a flattening of the resistance curve at low temperatures [60]. A high rate of magnetic scattering events, will result in a saturation like behaviour at low temperatures, irrespective of the presence of spin-orbit coupling.

For higher temperatures, when $\tau_{\text{in}} \ll \tau_{\text{so}}$, there is effectively no spin-orbit scattering, and the Expression (1.21) simplifies to:

$$\Delta\sigma^{\text{WL}}(T) \simeq \frac{e^2}{2\pi^2\hbar D^{1/2}} \left(\frac{1}{\tau_{\text{in}}}\right)^{1/2} . \tag{1.22}$$

In this regime, the conductivity change due to WL scales with temperature as $\Delta\sigma^{\text{WL}}(T) \propto T^{p/2}$.

The semiclassical Boltzmann contribution to resistivity is temperature-independent when the dominant contribution stems from elastic scattering events on static disorder, i.e. residual resistance. Such conditions generally coincide with the observation of interference effects (WL and WAL), where the elastic scattering rate $1/\tau_{\text{e}}$ surpasses the inelastic electron-phonon scattering rate $1/\tau_{\text{in}}$. Thus, barring other factors, the temperature dependence of total resistivity (conductivity) will be governed by the temperature dependence of WL and WAL, as characterized by Equation (1.21).

While residual resistivities are frequently observed at low temperatures even in the so-called good metals, the magnitude of interference effects is inversely proportional to the diffusion coefficient D (or the electron mean free path l). Given that good metals possess large diffusion coefficients, the contribution from the interference effect will be negligible.

Instead, these effects are usually discernible in materials with substantial amount of disorder, whether structural or chemical, when the electron mean free path l is short, thus leading to low diffusion coefficients D. For instance, such conditions are often found in high-resistivity amorphous alloys, including TE–TL alloys.

1.4.2.2 Electron-electron interaction effects

A second source of quantum corrections to the Boltzmann transport theory, potentially as significant as WL, stems from enhanced electron-electron interactions (EEI) due to the diffusive motion of electrons. Unlike WL effects, which would manifest in a system

of non-interacting electrons, the presence of EEI effects requires the Coulomb interaction between electrons.

In good metals owing to the ballistic motion, distance between electrons increases linearly with time, $r \propto v_{\mathrm{F}} t$. However, under diffusive motion, the inter-electron distance increases at a significantly slower rate $r \propto v_{\mathrm{F}}\sqrt{t\tau_{\mathrm{e}}}$. This slower dispersal means that electrons spend a longer period of time within a given spatial region, which in turn elevates the likelihood of two electrons encountering each other twice within a brief time interval. Consequently, this phenomenon gives rise to enhanced electron-electron interactions.

The relevant time scale for the enhanced interaction between two electrons, whose energies differ by $\Delta\varepsilon$, is the time $\hbar/\Delta\varepsilon$ during which the states of the two electrons are almost indistinguishable due to the Heisenberg uncertainty principle [61]. Given that diffusion occurs for electrons within the energy bounds of $\pm k_{\mathrm{B}}T$ around the Fermi level E_{F}, the mean energy difference between two conduction electrons is $\Delta\varepsilon \approx k_{\mathrm{B}}T$. As a consequence, the characteristic time frame wherein the enhanced interaction between two electron occurs is [62]:

$$\tau_{\mathrm{T}} \simeq \frac{\hbar}{2\pi k_{\mathrm{B}}T} \,, \tag{1.23}$$

called the *thermal coherence time*, and is analogous to the phase-breaking time τ_φ in the WL phenomena. With increasing temperature, τ_{T} decreases, subsequently reducing the EEI effect.

While a straightforward physical interpretation of WL is available, to our knowledge, no analogous, comprehensive, and straightforward interpretation exists for the EEI effect. Nonetheless, some attempts [62] have been undertaken to partially elucidate the physical origin of certain contributions (such as the Hartree component of the diffusion channel) to conductivity that arise from EEI.

The temperature-dependent correction to conductivity from enhanced electron-electron interactions in three dimensions, can be derived from comprehensive diagrammatic computations [41], and is given as:

$$\Delta\sigma^{\mathrm{EEI}}(T) = \frac{0.915e^2}{4\pi^2\hbar}\sqrt{\frac{k_{\mathrm{B}}T}{\hbar D}}\left[\frac{4}{3} - \frac{3}{2}\tilde{F}_\sigma - 2g(T)\right] \,, \tag{1.24}$$

where

$$\tilde{F}_\sigma = \frac{32}{3F}\left[\left(1+\frac{1}{2}F\right)^{\frac{3}{2}} - 1 - \frac{3}{4}F\right] \,, \tag{1.24a}$$

is the renormalized value of the parameter $0 \leq F \leq 1$, which is the average of the screened

Coulomb interaction over the Fermi surface [63, 64]. Additionally,

$$\frac{1}{g(T)} = \begin{cases} -\ln\left(\frac{T}{T_c}\right) & \text{for superconductors,} \\ \frac{1}{\lambda_0} + \ln\left(\frac{2e^{\gamma}T_F}{\pi T}\right) & \text{for normal metals,} \end{cases} \tag{1.24b}$$

is the so-called renormalized coupling constant, where λ_0 is the bare electron interaction constant determined by both the virtual-phonon exchange and repulsive Coulomb interaction [64–66], T_c is the superconducting transition temperature, T_F is the Fermi temperature, and $\gamma \approx 0.577$ is the Euler's constant.

The elements within the square bracket of Equation (1.24) are typically classified into the Diffusion (particle-hole) channel, further separated into exchange (4/3) and Hartree ($-3\tilde{F}_\sigma/2$) contributions, and the particle-particle (Cooper) channel ($-2g(T)$). The expression for the Cooper channel is valid for $\ln(T/T_c) \gg 1$ or $\ln(T_F/T) \gg 1$.

For superconductors, the Cooper channel contribution will increase conductivity, while for normal metals it reduces conductivity. For normal metals, however, the Fermi temperature T_F is typically in the order of $\sim 10^4$ K. Consequently, the magnitude of the contribution becomes negligible at low temperatures (<30 K), where EEI effects are typically observed in metallic glasses.

The exchange component of the Diffusion channel enhances conductivity, while the Hartree component, conversely, reduces conductivity with increasing temperature. Generally, the exchange component outweighs the Hartree component ($4/3 > 3\tilde{F}_\sigma/2$), leading to an overall EEI correction that increases the conductivity as $\sqrt{T}$, thus offering an additional mechanism for a negative temperature coefficient of resistance, besides WL.

Remarkably, the Expression (1.24) for the temperature dependence of the conductivity correction due to enhanced EEI bears a striking similarity to the Expression (1.22) for the temperature dependence of the WL correction. In fact, excluding the Cooper channel contribution, the ratio between the two mechanisms $\Delta\sigma^{\mathrm{EEI}}(T)/\Delta\sigma^{\mathrm{WL}}(T)$ scales with $\sqrt{T\tau_{\mathrm{in}}}$ [41]. This implies that when $T\tau_{\mathrm{in}} \gg \hbar/k_B \approx 7.6 \times 10^{-12}$ K s, the contribution from the EEI has decreased more than the WL contribution, compared to the zero-temperature limit ($\tau_{\mathrm{in}} = \infty$).[h] In other words, when the criteria is fulfilled — which typically arises at low temperatures if τ_{in}^{-1} increases faster than T — the temperature dependence of conductivity will be dominated by the temperature decrease of the EEI contribution.

For a comprehensive review of quantum corrections to Boltzmann transport theory, the

[h] The zero-temperature limit differs from the bare Boltzmann conductivity, due to a reduction of conductivity due to EEI and WL quantum corrections.

following articles are recommended. B. L. Altshuler and A. G. Aronov [41] offer a detailed diagrammatic analysis of enhanced electron-electron interaction effects, as does the review by H. Fukuyama [67], both of which also delve into the topic of weak localization. P. A. Lee and T. V. Ramakrishnan [63] explore enhanced electron-electron interaction effects from the perspective of scaling theory. B. Kramer and A. MacKinnon [68] provide an overview of the weak localization effect. Meanwhile, S. Chakravarty and A. Schmid [58] present a wave-based theory of weak localization based on semiclassical principles.

1.4.2.3 Temperature dependence of resistivity

In strong scattering, i.e. high-resistivity alloys ($\gtrsim 150\,\mu\Omega\,\mathrm{cm}$), the elastic scattering rate is higher than the inelastic electron-phonon scattering rate, $\tau_\mathrm{e} \ll \tau_\mathrm{in}$. As already mentioned, under these circumstances, the Boltzmann component of conductivity exhibits a weak temperature dependence, effectively behaving as a large residual resistance. The temperature variation of conductivity is then principally driven by quantum corrections to the conductivity (WL, WAL, EEI), which are significant in disordered systems with small diffusion coefficients (i.e., short electron mean free paths).

In high-resistivity amorphous alloys, where primarily quantum corrections dictate the temperature dependence of resistivity, two temperature regimes can be delineated [3]. In the high-temperature regime ($\gtrsim 30\,\mathrm{K}$), the temperature dependence of resistivity is predominantly due to the suppression of the WL contribution as temperature increases. Conversely, in the low-temperature regime ($\lesssim 30\,\mathrm{K}$), the EEI contribution becomes increasingly significant as the temperature decreases, dictating the temperature variation of resistivity .

The temperature dependence of WL originates from the temperature dependence of the dephasing time τ_φ, which can be identified with the inelastic electron-phonon scattering time τ_in as discussed earlier. In the presence of strong impurity scattering, the low-temperature ($T < \Theta_\mathrm{D}$) inelastic electron-phonon scattering rate scales as $1/\tau_\mathrm{in} \propto T^2$, in contrast to $1/\tau_\mathrm{in} \propto T^3$ scaling observed in good transition metals (see [69, 70] and references therein). While the inelastic electron-electron scattering rate also scales as $1/\tau_\mathrm{in} \propto T^2$ at low temperatures, its contribution remains negligible compared to electron-phonon scattering [3, 69]. Above the Debye temperature ($T > \Theta_\mathrm{D}$), the scattering rate adopts the classical $1/\tau_\mathrm{in} \propto T$ dependence, though this scaling is known to extend somewhat below the Debye temperature.

The aforementioned temperature-dependent behaviour of the inelastic scattering time leads to the following temperature profile of weak localization in high-resistivity amor-

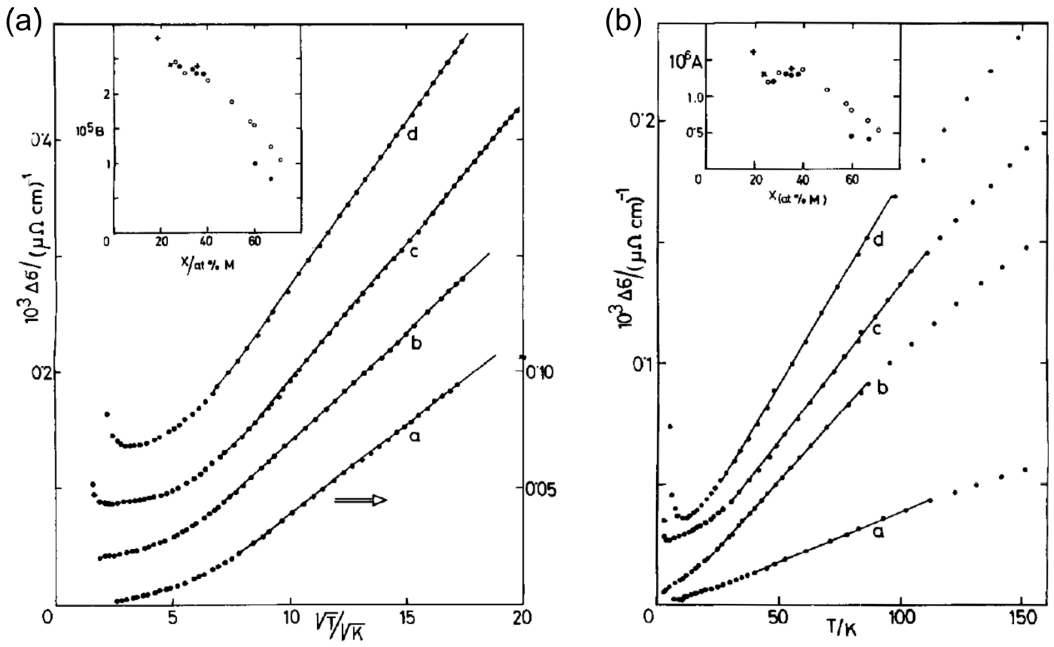

Figure 1.12: Change of conductivity $\Delta\sigma$ as a function of $\sqrt{T}$ (**a**) and T (**b**) for a set of $Zr_{1-x}TL_x$ alloys, marked as follows: a – $Zr_{0.33}Ni_{0.67}$, b – $Zr_{0.50}Cu_{0.50}$, c – $Zr_{0.76}Fe_{0.24}$, d – $Zr_{0.81}Co_{0.19}$. The insets shows the variations of the respective fit slope values with TL concentrations x. Reproduced from [70].

phous metals:

$$\Delta\sigma^{\mathrm{WL}}(T) \propto \begin{cases} T & \text{for } T \ll \Theta_{\mathrm{D}}\,, \\ \sqrt{T} & \text{for } T \gtrsim \Theta_{\mathrm{D}}\,. \end{cases} \tag{1.25}$$

Empirically, the transition between these two temperature regimes roughly occurs at $\Theta_{\mathrm{D}}/3$ [69–71]. Figure 1.12 provides an example of this temperature dependence of conductivity, for a set of Zr–TL alloys.

At lower temperatures, the resistivity (conductivity) curve begins to display signs of saturation, attributable to spin-orbit coupling, and potentially due to scattering on magnetic impurities. However, as the temperature is further reduced, below approximately 15 K, an increase in resistivity is observed. This increase has been ascribed to the EEI contribution to conductivity, and exhibits the characteristic $\sqrt{T}$ dependence. In superconducting systems, however, this low-temperature behaviour may not be easily discernible if the superconducting transition temperature T_c is sufficiently high. This is due to superconducting fluctuations, which lead to a decrease in resistivity even above T_c.

This combination of temperature-dependent contributions of the WL and EEI effects

was used to interpret the temperature dependence of resistivity of amorphous TE-TL [3, 45, 55, 69–74], as well as other high-resistivity amorphous metals (for instance, $La_{1-x}Al_x$ [75]) over a wide temperature range.

It is pertinent to acknowledge the alternative proposals that have been made to describe the temperature dependence of resistivity in the high- and low-temperature regimes of these amorphous alloys. For instance, U. Mizutani and colleagues proposed an empirical function:

$$\rho(T) = A + B \exp\left(-\frac{T}{\Delta}\right) \ . \tag{1.26}$$

to describe the temperature dependence of resistivity in the 30-300 K range for high-resistivity non-magnetic metallic glasses with d-electron or f-electrons at the Fermi level. At lower temperatures, the resistivity deviates from the exponential function.

They successfully fitted this equation to a diverse range of TE–TL and other amorphous alloys (for instance, $Y_{1-x}Al_x$ and $La_{1-x}M_x$ where M≡Al, Si, Ag, Au) [76–80]. They tentatively attributed this temperature dependence to a phonon-assisted delocalisation process [80].

In the low-temperature regime, distinguishing between $\rho(T) \propto \sqrt{T}$ and $\rho(T) \propto \ln(T)$ temperature dependencies has proven to be a challenge [3, 45, 71, 80]. This low-temperature increase was initially attributed to the Kondo effect due to magnetic impurities, $\rho(T) \propto \ln(T)$. However, this was subsequently discounted, as the increase was observed to persist in samples with no trace of magnetic impurities and in the presence of high magnetic fields which should destroy the Kondo effect [3].

An alternative proposal for the observed increase involved electron scattering on fast relaxing two-level systems (TLS) [3, 81, 82]. Since amorphous materials are in a metastable state, certain atoms or groups of atoms can tunnel between states of roughly equivalent energy. Scattering from these centres was proposed to lead to a resistivity increase at low temperatures, akin to the Kondo effects, given by $\rho(T) \propto \ln(A+T^2)$. Furthermore, scattering from TLS could result in an inelastic scattering rate proportional to T, thus producing a $\sqrt{T}$ temperature dependence of the WL contribution to conductivity, which is also predicted from the EEI effect.

While it has been argued that both the direct contribution to resistivity and the variation in the inelastic scattering time would result in negligible resistivity corrections (refer to [3] and the references therein), the significance of the TLS effect remains an open issue [83, 84].

1.4.2.4 Magnetoresistance from quantum corrections

To start the discussion on magnetoresistance (MR), a qualitative overview of the influence of a magnetic field on quantum interference effects (WL and WAL) is provided. This is followed by a detailed accounting of the quantitative theoretical expressions describing the magnetic field dependence of WL (inclusive of WAL) and EEI corrections to conductivity. In the next subsections 1.4.2.5, an overview of MR in amorphous TE–TL alloys is presented.

As a wavefunction propagates in a magnetic field, it accumulates an additional phase change, thus necessitating a modification of the line integral in Equation (1.12) where $\mathbf{k}$ is replaced by $(\mathbf{k} - e\mathbf{A}/\hbar)$, where $\mathbf{A}$ is the vector potential of the magnetic field, $\mathbf{A} = \nabla \times \mathbf{B}$. The additional phase change arising from a magnetic field for paths around a closed loop is:

$$\oint \frac{e}{\hbar}\mathbf{A}\mathrm{d}\mathbf{l} = \int \frac{e}{\hbar}\mathbf{B}\mathrm{d}\mathbf{S} = \frac{e}{\hbar}\phi \ , \tag{1.27}$$

where ϕ denotes the magnetic flux threading the loop. The ensuing phase difference between two counter-propagating waves is therefore $2e\phi/\hbar$.

As the magnetic field strength increases, this phase difference also increases, thereby diminishing constructive interference and the probability for a particle to return to its initial position, which in turn reduces resistivity.

Further increase of the magnetic field will bring the waves back into phase, thereby enhancing constructive interference and resistivity, leading to a periodic fluctuation in MR as the flux increases with a period of $\hbar/2e$. This phenomenon is known as the *Aharonov-Bohm effect* [8].

In a disordered system, the interference effect underlying WL is formed from closed loops of varying sizes and orientations relative to the magnetic field, thereby yielding differing values for the magnetic flux and dephasing. Eventually, random values of the phase difference for different closed loop paths lead to a complete destruction of the constructive interference that contributes to enhanced backscattering. An increase in magnetic field suppresses the resistivity increase due to WL, resulting in a characteristic negative MR (positive magnetoconductivity). The characteristic time in which dephasing due to the magnetic field occurs is given by [41]:

$$\tau_B = \frac{\hbar}{4eBD} \ . \tag{1.28}$$

For long magnetic times $t_B \gg \tau_{\mathrm{in}}$, i.e. weak magnetic fields, all paths experience a small

phase change, leading to a unified dephasing of all paths and an accompanying reduction in resistivity. For small values of the phase difference $\Delta\varphi$, the probability of returning to the starting position **O** in a closed loop path is $W(B) = 2|A|^2(1+\cos\Delta\varphi) \approx 2|A|^2(2-\Delta\varphi^2/2)$. Given that $\Delta\varphi \propto B$, for weak magnetic fields the resistivity decrease will be proportional to $\Delta\rho \propto B^2$.

At higher magnetic fields, the reduction in resistivity is more gradual as paths with waves moving out of phase are partially offset by those moving back into phase. For $\tau_B < \tau_{\text{in}}$, the temperature dependence can be obtained by substituting the upper integration limit in Equation (1.16) from τ_{in} to τ_B. This leads to a resistivity decrease in a magnetic field as $\Delta\rho \propto \sqrt{1/\tau_B} \propto \sqrt{B}$.

The presence of a magnetic field similarly destroys the interference terms leading to weak anti-localization, enhanced forward-scattering, resulting in a positive MR. Similarly to WL, the resistivity increases as $\Delta\rho \propto B^2$ for weak magnetic fields, transitioning to $\Delta\rho \propto \sqrt{B}$ for high magnetic fields.

The expression for the change in conductivity with magnetic fields due to WL and WAL in case of strong or weak spin orbit scattering is given as [85, 86]:

$$\Delta\sigma^{\text{WL}}(B) = \frac{e^2}{2\pi^2\hbar}\sqrt{\frac{eB}{\hbar}}\left[\frac{3}{2}f_3\left(\frac{4eDB\tau_{\text{so}}^*}{\hbar}\right) - \frac{1}{2}f_3\left(\frac{4eDB\tau_{\text{in}}}{\hbar}\right)\right], \tag{1.29}$$

where:

$$\frac{1}{\tau_{\text{so}}^*} = \frac{1}{\tau_{\text{in}}} + \frac{4}{\tau_{\text{so}}}, \tag{1.29a}$$

and

$$f_3(x) = \sum_{n=0}^{\infty}\left\{2\left(n+1+\frac{1}{x}\right)^{\frac{1}{2}} - 2\left(n+\frac{1}{x}\right)^{\frac{1}{2}} - \left(n+0.5+\frac{1}{x}\right)^{-\frac{1}{2}}\right\}, \tag{1.29b}$$

with limiting values [87]:

$$f_3(x) = \begin{cases} x^{3/2}/48 & \text{for } x \ll 1\,, \\ 0.6049 & \text{for } x \gg 1\,. \end{cases} \tag{1.29c}$$

As discussed qualitatively, the Equation (1.29) has limiting forms of $\propto B^2$ and $\propto \sqrt{B}$, for small and high magnetic fields, respectively. The sign of the change will depend on the strength of spin-orbit scattering. Specifically, four different magnetic field regimes can be

identified. Without spin-orbit scattering, for small fields Expression (1.29) reduces to:

$$\Delta\sigma^{\mathrm{WL}}(B) \approx +\frac{e^2}{192\pi^2\hbar}\ (4D\tau_{\mathrm{in}})^{3/2}\ \left(\frac{eB}{\hbar}\right)^2\ , \tag{1.30a}$$

and only a positive magnetoconductivity (negative MR) is observed. However, in the presence of spin-orbit scattering there is necessarily a small-field regime $\tau_B > \tau_{\mathrm{so}}$ in which magnetoconductivity is negative (a positive MR) with the form:

$$\Delta\sigma^{\mathrm{WL}}(B) \approx -\frac{e^2}{96\pi^2\hbar}\ (4D\tau_{\mathrm{in}})^{3/2}\ \left(\frac{eB}{\hbar}\right)^2\ . \tag{1.30b}$$

For high magnetic fields $\tau_{\mathrm{in}} \gg \tau_B$, if $\tau_B > \tau_{\mathrm{so}}$ still holds, the magnetoconductivity will remain positive and is defined as:

$$\Delta\sigma^{\mathrm{WL}}(B) \approx -0.6049\frac{e^2}{4\pi^2\hbar}\ \sqrt{\frac{eB}{\hbar}}\ . \tag{1.30c}$$

For even higher magnetic fields $\tau_B < \tau_{\mathrm{so}}$, spin-orbit scattering is ineffective in the time before dephasing due to the magnetic field occurs and a positive magnetoconductivity (negative MR) appears:

$$\Delta\sigma^{\mathrm{WL}}(B) \approx +0.6049\frac{e^2}{2\pi^2\hbar}\ \sqrt{\frac{eB}{\hbar}}\ . \tag{1.30d}$$

The same expressions is obtained in the high-field regime if no spin-orbit scattering is present. Interestingly, the high field regimes are independent of τ_{in}, and therefore temperature, while the low field regime can be used to determine the value of τ_{in}.

What magnetic field regimes will be observed in a material will depend on the relative size of the spin-orbit time τ_{so} and inelastic scattering time τ_{in}. Accordingly, the shape of the MR curve can be classified into three categories, as illustrated in Figure 1.13. For weak spin-orbit scattering $\tau_{\mathrm{in}} \ll \tau_{\mathrm{so}}$ a negative MR is observed. Although, a small positive magnetoresistance may still be observed at low enough magnetic fields for a finite value of spin-orbit scattering. For very strong spin-orbit scattering $\tau_{\mathrm{in}} \gg \tau_{\mathrm{so}}$, the magnetic field required to suppress spin-orbit scattering is larger than the applied magnetic fields and only a positive MR is observed up. For moderate values of spin-orbit coupling $\tau_{\mathrm{in}} \simeq \tau_{\mathrm{so}}$, a transition from a positive to negative MR will be observed at approximately $\tau_B \simeq \tau_{\mathrm{so}}$.

An additional contribution to MR of WL and WAL originates from Zeeman spin

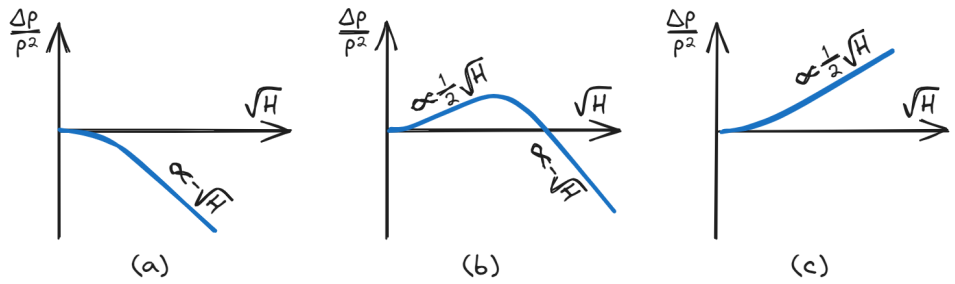

Figure 1.13: A schematic diagram of the WL and WAL magnetoconductivity for (**a**) weak $\tau_{\text{in}} \ll \tau_{\text{so}}$, (**b**) moderate $\tau_{\text{in}} \sim \tau_{\text{so}}$ and (**c**) strong $\tau_{\text{in}} \gg \tau_{\text{so}}$ spin-orbit scattering. After [88].

splitting. A full expression including the spin splitting contribution is given as [59]:

$$\begin{aligned}\Delta\sigma^{\text{WL}}(B) = &\frac{e^2}{2\pi^2\hbar}\left\{\sqrt{\frac{eB}{\hbar}}\left[f_3\left(\frac{h}{1+t}\right)+\frac{0.5}{\sqrt{1-\gamma}}\left[f_3\left(\frac{h}{t_+}\right)-f_3\left(\frac{h}{t_-}\right)\right]\right]\right.\\ &\left.-\frac{1}{\sqrt{D\tau_{\text{so}}}}\left[\frac{\sqrt{t_+}-\sqrt{t_-}}{\sqrt{1-\gamma}}-\sqrt{t+1}+\sqrt{t}\right]\right\}\ ,\end{aligned} \tag{1.31}$$

where

$$\begin{aligned} t &= \frac{\tau_{\text{so}}}{4\tau_{\text{in}}}\ ,\\ t_\pm &= t + 0.5(1 \pm \sqrt{1-\gamma})\ ,\\ h &= \frac{eDB\tau_{\text{so}}}{\hbar}\ ,\\ \gamma &= \left(\frac{g^*\mu_B B\tau_{\text{so}}}{2\hbar}\right)^2\ , \end{aligned} \tag{1.31a}$$

g^* is the effective g-factor and μ_{B} is the Bohr magneton. Without spin splitting, i.e. $\gamma = 0$, this expression is reduced back to Equation (1.29).

Both models in Expressions (1.29) and (1.31) produce identical values in the limits of $\tau_{\text{so}} \to 0$ and $\tau_{\text{so}} \to \infty$. Between those limits the values can differ appreciably. For high values of the diffusion coefficient $D > 1\,\text{cm}^2\,\text{s}^{-1}$ the difference is negligible [64, 89]. However, this is generally not the case for metallic glasses where the diffusion coefficient is often lower than $1\,\text{cm}^2\,\text{s}^{-1}$ and the full expression including Zeeman spin splitting should be used [89].

The exchange contribution to the Diffusion channel in the enhanced EEI correction to conductivity is insensitive to the magnetic field and the EEI contribution to MR will originate from the Hartee term and the Cooper channel.

In the Cooper channel the MR due to orbital breaking is given as [86]:

$$\Delta\sigma^{\mathrm{EEI,C}}(B) = -\alpha\frac{e^2}{2\pi^2\hbar}\sqrt{\frac{eB}{\hbar}}\; g(T,B)\; \phi_3\left(\frac{2DeB}{\pi k_{\mathrm{B}}T}\right) \tag{1.32}$$

where:

$$\phi_3(x) = \sqrt{\frac{\pi}{2x}}\int_0^\infty \frac{t^{1/2}}{\sinh^2 t}\left(1 - \frac{xt}{\sinh(xt)}\right)\mathrm{d}t \tag{1.32a}$$

with limiting values [87]:

$$\phi_3(x) = \begin{cases} 0.32925\; x^{3/2} & \text{for } x \ll 1\ , \\ 1.900344 & \text{for } x \gg 1\ , \end{cases} \tag{1.32b}$$

The coefficient α was defined as having a value of 1 for weak and 1/4 for strong spin orbit coupling. However, newer calculations arrived at $\alpha = 1/\pi$ irrespective of the strength of spin-orbit coupling [41, 64]. Since $g(T,B)$ is generally negative above the superconducting transition temperature, the Cooper channel will produce a positive contribution to magnetoconductivity, i.e. negative MR.

Two other expressions for the magnetic dependence of conductivity for the enhance EEI in the Copper channel exist in literature, one that includes the Zeeman spin splitting and magnetic spin scattering [41] and the other that includes dephasing due to inelastic scattering [90]. These two expressions reproduce values of Equation (1.32) in the limit of large diffusivity and long dephasing time, respectively. Values of all three expression agree well in the limit of small magnetic fields (with $\alpha = 1/\pi$). However, they differ substantially for high magnetic fields with input values typical of metallic glasses. That said, since the coupling constant $g(T,B)$, which is found in all three expressions, has not been satisfactorily generalized to include the effects of the magnetic field, it is unclear if either expression is appropriate [64]. The treatment of the Cooper channel is often restricted to small fields, where $g(T,B) \approx g(T)$ values given by Equation (1.24b) can be used and the relatively simple Expression (1.32) can be applied.

In the diffusion channel, orbital dephasing does not lead to a change in resistance, and the magnetic field dependence is due to spin splitting, which results in a positive MR contribution, is given as [41, 91]:

$$\Delta\sigma^{\mathrm{EEI,D}}(B) = -\frac{e^2}{4\pi^2\hbar}\tilde{F}_\sigma\sqrt{\frac{k_{\mathrm{B}}T}{2\hbar D}}\; g_3\left(\frac{g\mu_B B}{k_{\mathrm{B}}T}\right)\ , \tag{1.33}$$

where $\tilde{F}_\sigma$ is given by Equation 1.24a and:

$$g_3(x) = \int_0^\infty \mathrm{d}\Omega \left\{ \frac{\mathrm{d}^2}{\mathrm{d}\Omega^2} \left[\frac{\Omega}{\mathrm{e}^\omega - 1} \right] \right\} \left(\sqrt{\Omega + x} + \sqrt{|\Omega - x|} - 2\sqrt{\Omega} \right) , \tag{1.33a}$$

with limiting values [87]:

$$g_3(x) = \begin{cases} 0.056464\ x^2 & \text{for } x \ll 1\,, \\ x^{1/2} & \text{for } x \gg 1\,. \end{cases} \tag{1.33b}$$

Just as with MR due to WL, Equations (1.33) and (1.32) exhibit the same asymptotic behaviour, notwithstanding the temperature and field dependence of $g(T, B)$. Specifically, they are proportional to B^2 at low fields, and proportional to a $\sqrt{B}$ and temperature independent at high magnetic fields. That said, the contributions to the total MR and the characteristic fields that mark the transition between the two regimes are different than in MR due to WL and WAL. Consequently, in a regime where both EEI and WL effects contribute to MR, the resulting dependence on the magnetic field will exhibit complex behaviour.

In superconducting materials, quenching of superconducting fluctuations by the magnetic field provides another vital contribution to magnetoresistance (MR). These are divided into the Aslamasov-Larkin and Maki-Thomson contributions, associated with superconducting fluctuations and scattering of normal electrons by these fluctuations, respectively [41, 64].

The Aslamasov-Larkin contribution decreases rapidly beyond the superconducting transition temperature T_c, proving significant only in the immediate vicinity of the superconducting transition. Conversely, the Maki-Thomson contribution declines more slowly with temperature, and is relevant even far from the superconducting transition. While the Maki-Thomson contribution to the temperature dependence of resistivity in three dimensions is typically negligible compared to the Cooper channel contribution, it constitutes a significant component of the MR in superconducting materials.

The Maki-Thomson contribution to magnetoconductivity is given as follows [41]:

$$\Delta\sigma^{\mathrm{MT}}(B) = -\frac{e^2}{2\pi^2\hbar} \sqrt{\frac{eB}{\hbar}}\ \beta(T, B)\ f_3 \left(\frac{4eDB\tau_{\mathrm{in}}}{\hbar} \right) . \tag{1.34}$$

It has a form similar to magnetoconductivity due to WL and they are often merged into a single expression for superconducting alloys, by substituting $1/2 \to 1/2 + \beta(T, B)$

next to the singlet term in Equation (1.29). Given that $\beta(T, B) > 0$ is always positive, the Maki-Thomson contribution reduces magnetoconductivity (increases MR) in absolute terms.

The values of $\beta(T, B = 0)$ were tabulated by Larkin A. I. [65] as a function of renormalized coupling constant $g(T)$ for values not to close to the transition temperature T_c. The precise magnetic field dependence of $\beta(T, B)$ remains unknown [41, 64]. However, an approximate form of field dependence is often employed. Rather than calculating $g(T)$ with Equation (1.24b), $g(T, B)$ is calculated using the following formula [92]:

$$\frac{1}{g(T,B)} = -\ln\left(\frac{T}{T_c}\right) + \Psi\left(\frac{1}{2}\right) - \Psi\left(\frac{1}{2} + \frac{DeB}{2\pi kT}\right) , \tag{1.35}$$

where $\Psi(x)$ is the Digamma function. Then, Larkin's tabulation of $\beta(g(T))$ is employed to determine an approximate field-dependent $\beta(T, B)$ from $g(T, B)$. Although, such calculated vales of $\beta(T, B)$ have the wrong asymptotic form. Instead of converging to the magnetoconductivity value in the absence of the Maki-Thomson contribution, they result in a vanishing magnetoconductivity at high fields [64, 93].

1.4.2.5 Magnetoresistance in TE–TL alloys

In the low-temperature regime ($\lesssim 50\,\mathrm{K}$), non-magnetic TE–TL alloys exhibit magnetoresistance approximately 10^4 times greater than the normal metallic MR (which, according to the Kholer's rule, should be of the order of $\Delta\rho/\rho \sim 10^{-8}$ at 1 T) [8, 55]. The prominent contribution to the MR is found to originate from magnetic field dependence of WL and WAL [88, 94], even though the temperature dependence of resistivity below about 15 K is attributed to temperature-dependent contributions from EEI.

Contributions to MR from EEI effects are minor, becoming significant only at low temperatures and high magnetic fields, specifically, under conditions of high B/T ratios — at temperatures exceeding 1 K for fields higher than approximately 10 T, but only a few tesla for temperatures below 1 K [55, 88]. Additionally, in superconducting alloys, MR is anticipated to increase significantly as the superconducting transition temperature T_c is approached, due to the suppression of superconducting fluctuations by the magnetic field.

J. B. Bieri et. al. [88] conducted MR measurements on a series of different strong scattering amorphous alloys. The alloys demonstrated varying MR profiles, depending on the relative strength of spin-orbit scattering. Alloys composed of "light" metals and thereby exhibiting weak spin-orbit scattering, such as $Mg_{0.20}Cu_{0.80}$, displayed negative

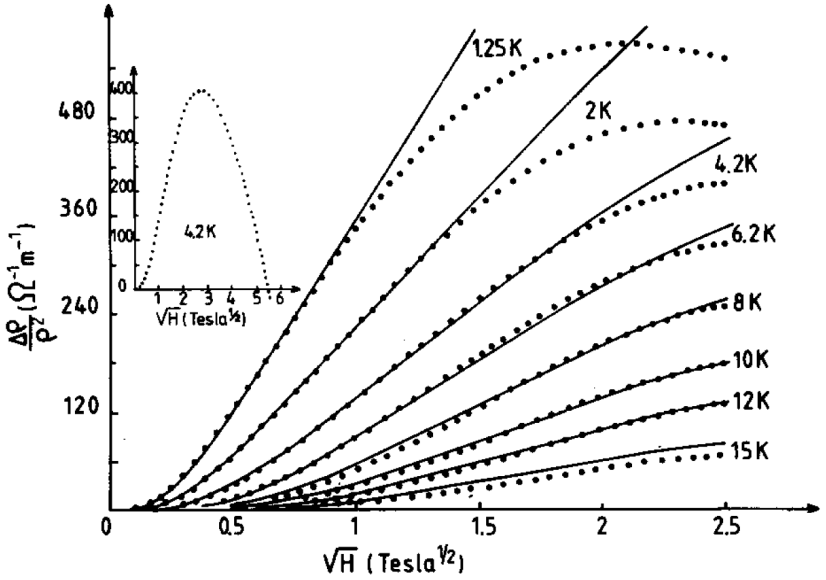

Figure 1.14: Magnetoresistance as a functions of $\sqrt{\mu_0 H}$ at a set of temperatures for amorphous $Zr_{0.43}Cu_{0.57}$. Solid lines depict fits to WL magnetoresistance given in Equation (1.29) with the contribution for Maki-Thomson superconductive fluctuations given with Equation (1.34). Magnetic field independent values of $\beta(T)$ were used. Inset: magnetoresistance measured in a very high pulsed magnetic field, up to 30 T. Reproduced from [97].

MR in line with WL, as illustrated in Figure 1.13(a). Notably, in accordance with theory, the slopes of the linear variation in $\sqrt{\mu_0 H}$ were temperature-independent, and a minor positive MR was observed at the lowest temperature (1.2 K) in weak magnetic fields.

On the other hand, alloys with "heavy" elements indicative of strong spin-orbit coupling, such as $Cu_{0.50}Lu_{0.50}$ and $Pd_{0.80}Si_{0.20}$), exhibited solely positive MR up to 6 T, as illustrated in Figure 1.13(c). Meanwhile, a transition from positive to negative MR in high magnetic fields was observed in alloys displaying moderate spin-orbit scattering, such as $Cu_{0.50}Y_{0.50}$ and $Zr_{0.43}Cu_{0.57}$), as illustrated in Figure 1.13(b).

Comparable behaviour has been reported in other amorphous strong scattering alloys (such as Ti–Cu, Zr–Cu, Y–Al, Cu–Mg, Ca–Al; see [3] and references therein). Additionally, when small amounts of "heavy" elements, such as Au and Ag, were introduced to the parent Ca-Al alloys, a transition from negative to positive MR was observed, attributable to the substantial spin-orbit coupling associated with Au and Ag atoms [95, 96].

The magnetoresistance (MR) behaviour of the amorphous alloy $Zr_{0.43}Cu_{0.57}$ will serve as an illustrative example, and is shown in Figure 1.14. A characteristic positive MR, transitioning to a negative slope at high fields and low temperatures, is observed. The inset

of Figure 1.14 shows a broad peak around 9 T during a pulsed magnetic field measurement at 4.2 K. Eventually, at around 30 T, MR values transition into the negative range. The observed change in slope in the $\sqrt{\mu_0 H}$ dependence, contrary to expectations for WL MR, arises from the influence of Maki-Thomson superconducting fluctuations. The observed discrepancies between the fitting curves and the empirical data are attributed to several factors. These include the omission of electron-electron interaction (EEI) effects, the utilization of a field-independent $\beta(T)$ [94], and the neglect of the Zeeman spin splitting contribution to weak antilocalization (WAL), which necessitates the use of Equation (1.21) instead of Equation (1.29) [89].

A similar MR behaviour was observed in $Cu_{1-x}Ti_x$ alloys [94]. A peak in MR around 4 T was discerned in $Ti_{0.65}Cu_{0.35}$, with negative MR values observable above 20 T. In contrast, $Ti_{0.50}Cu_{0.50}$ exhibited a broad peak only at around 30 T. Better fit to the data, compared to $Zr_{0.43}Cu_{0.57}$, was achieved with the use of the orbital component of WL MR combined with the Maki-Thomson contribution using a magnetic field dependent $\beta(T, \mu_0 H)$ factor and the diffusion component of the EEI MR given with Equation (1.33).

Various researchers have used the low magnetic field MR data to determine the values and temperature dependence of the inelastic scattering time τ_{in} (see [3] and references therein). For instance, from linear fits to $(\mu_0 H)^2$, J. B. Bieri et. al. [88, 97] found that $\tau_{\text{in}}^{-1} \propto T^2$ for temperatures above 5-10 K across a range of different amorphous alloys. Meanwhile, A. Schulte and G. Fritsch [98] found a relationship of $\tau_{\text{in}}^{-1} \propto T^p$ with $p = 2-3$ for a range of $Ti_{1-x}Cu_x$ alloys between 6-20 K. M. A. Howson et. al. [94] used fits across the whole magnetic field range to the equations of WL and WWI, concluding that $\tau_{\text{in}}^{-1} \propto T^2$ above 20 K deviates to $\tau_{\text{in}}^{-1} \propto T^4$ between 4-10 K.

P. Lindqvist and Ö. Rapp [89] noted that the scaling parameter of calculated τ_{in} at low temperatures is highly sensitive to the choice of the diffusion coefficient. In a more recent work, P. Lindqvist [99], with a thorough handling of the limiting values employed in τ_{in} calculations, found $\tau_{\text{in}}^{-1} \propto T^p$ with $p = 1.15 \pm 0.1$ between 1.5-5 K and $p = 3.7 \pm 0.5$ between 20-50 K for $Ti_{0.35}Cu_{0.65}$. These results for τ_{in} were interpreted as a combination of saturating behaviour at low temperatures due to scattering from magnetic impurities or zero-point motion, and contributions from electron-electron scattering ($p = 3/2$) and electron-phonon scattering ($p = 3 - 4$). These observations have cast doubt on the applicability of Expression (1.25) to describe the temperature dependence of resistivity due to weak localization at low temperatures.

1.4.3 Superconductivity

TE–TL amorphous alloys are considered extremely dirty type-II superconductors, due to very short electron mean free paths l_e, with estimated values of the dirtiness parameter $\xi_0/l_e \approx 300 - 1300$ and the Ginzburg-Landau parameter $\kappa = 70 - 100$ [100, 101], where ξ_0 is the BCS coherence length and λ the penetration depth.

The superconducting transition temperature T_c for TE–TL alloys are usually below 4 K, and decrease with increasing TL content, as seen in Figure 1.15,. The rate of the decrease depends on the TL element, and increases in order Ni, Cu, Co, Fe [66, 100, 102, 103].

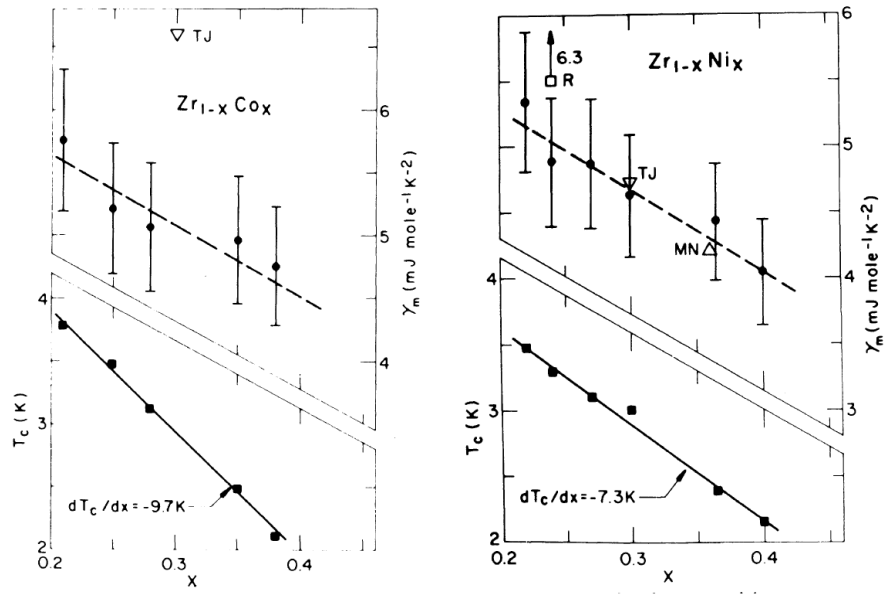

Figure 1.15: Composition dependence x of the superconducting transition temperature T_c and the molar specific-heat coefficient γ_m of $Zr_{1-x}Co_x$ (left panel) and $Zr_{1-x}Ni_x$ (right panel) amorphous alloys. Reproduced from [100].

The variation with TE content is less clear. The values for (3d) Ti–TL and (5d) Hf–TL alloys are generally lower than those of (4d) Zr–TL [66, 102, 104]. Similarly, measurements on $(Zr_{1-x}Ti_x)_{0.78}Ni_{0.22}$ showed a significant decrease of T_c with increasing Ti content, while for $(Zr_{1-x}Nb_x)_{0.78}Ni_{0.22}$ T_c values increased with small amounts of added Nb content (5-15%) and then decreased for higher concentrations of Nb [100]. Additionally, no superconductive transitions for metallic glasses in $Ti_{1-x}Ni_x$ and $Ti_{1-x}Cu_x$ alloys were observed down to 1.4 K and 1.0 K respectively [102].

The temperature variation of the upper critical field $\mu_0 H_{c2}(T)$ is usually well described

in metallic glasses by the Werthamer–Helfand–Hohenberg (WHH) theory, also known as the Werthamer–Helfand–Hohenberg-Maki (WHHM) theory [100, 105, 106], which includes the effects of the Pauli spin paramagnetism and spin-orbit interactions. According to the WHH theory, in the dirty limit, the critical field $\mu_0 H_{c2}(t)$ is obtained as the magnetic field that satisfies [107]:

$$\begin{aligned}\ln\left(\frac{1}{t}\right) = &\left(\frac{1}{2}+\frac{i\lambda_{\mathrm{so}}}{4\gamma}\right)\Psi\left(\frac{1}{2}+\frac{\bar{h}+\frac{1}{2}\lambda_{\mathrm{so}}+i\gamma}{2t}\right)\\ &+\left(\frac{1}{2}-\frac{i\lambda_{\mathrm{so}}}{4\gamma}\right)\Psi\left(\frac{1}{2}+\frac{\bar{h}+\frac{1}{2}\lambda_{\mathrm{so}}-i\gamma}{2t}\right)-\Psi\left(\frac{1}{2}\right)\ ,\end{aligned} \tag{1.36}$$

where $\Psi(x)$ is the Digamma function,

$$t = \frac{T}{T_c}\ , \tag{1.36a}$$

is the reduced temperature,

$$\bar{h} = \frac{eH_{c2}D}{k_{\mathrm{B}\pi T_c}}\ , \tag{1.36b}$$

is the scaled upper critical field,

$$\alpha = \frac{\hbar}{2m_{\mathrm{e}}D}\ , \tag{1.36c}$$

is the Maki parameter [108],

$$\lambda_{\mathrm{so}} = \frac{\hbar}{3\pi k_{\mathrm{B}} T_c \tau_{\mathrm{so}}}\ , \tag{1.36d}$$

is the spin-orbit interaction parameter and

$$\gamma = \left[\left(\alpha\bar{h}\right)^2 - \left(\tfrac{1}{2}\lambda_{\mathrm{so}}\right)^2\right]^{1/2}\ . \tag{1.36e}$$

However, in order to obtain a proper fit the measured $\mu_0 H_{c2}(t)$ data to the WHH formula, a wide enough temperature range needs to be measured, down to at least $0.2T_c$ [106].

The Maki parameter describes the relative importance of the orbital and spin paramagnetic Cooper pair breaking mechanisms in the magnetic field, and can be defined as [108]:

$$\alpha = \sqrt{2}\frac{H_{c2}^{\mathrm{orb}}(0)}{H_{\mathrm{P}}(0)}\ , \tag{1.37}$$

where $H_{c2}^{\mathrm{orb}}(0)$ and $H_{\mathrm{P}}(0)$ are the orbital- and Pauli-limiting fields respectively. In the dirty limit, the orbital-limiting field can be estimated from the initial slope of the upper

critical field $(\mu_0 dH_{c2}/dT)_{T=T_c}$ as:

$$\mu_0 H_{c2}(0) = -0.69 T_c \left(\mu_0 \frac{dH_{c2}}{dT}\right)_{T=T_c} . \tag{1.38}$$

Whereas, the Pauli-limiting field for a weak-coupling BCS superconductor is:

$$\mu_0 H_{\mathrm{P}}^{\mathrm{BCS}}(0) = 1.84 T_c . \tag{1.39}$$

From this considerations, in the absence of spin-orbit interaction ($\lambda_{\mathrm{so}} = 0$) according to the WHH formula the upper critical field can be estimated as:

$$\mu_0 H_{c2}(0) = \frac{H_{c2}^{\mathrm{orb}}(0)}{\sqrt{1+\alpha^2}} . \tag{1.40}$$

That said λ_{so} is not negligible in TE-TL alloys [100, 106]. Additionally, the electron-phonon and spin-fluctuation corrections to the Pauli limiting field need to be considered. However, as noted by N. Toyota et. al. [105], the Pauli limiting field should be renormalized on account of electron-phonon coupling (λ_{ep}), spin-fluctuations (λ_{sf}) and the Stoner factor S, which are not insignificant in TE–TL metallic glasses [66, 102, 109].

Chapter 2

Concepts

This chapter will briefly review some concepts and phenomena relevant for the discussion on temperature dependence of resistivity in chapter 4.

2.1 Anderson localization

It was first pointed out by P. W. Anderson [110] that the knowledge of the density of states is not sufficient to describe the physical properties of disordered systems. The view had previously been that scattering by random potential causes the Bloch waves to lose phase coherence on the length scale of the mean free path, but that wavefunctions remain extended throughout the system. Anderson pointed out that in the presence of strong disorder electron wavefunctions can become localised. The wavefunction is confined to a small region of space, falling of exponentially with distance from a starting point in space

$$\psi(\boldsymbol{r}) \propto \mathrm{e}^{-|\boldsymbol{r}-\boldsymbol{r}_0|/\xi} \tag{2.1}$$

where ξ is the localization length. Furthermore, if states at the Fermi level E_F are localised no current can pass thorough the system at absolute zero, i.e. the system will exhibit insulation behaviour, even though the density of states at the Fermi level $N(E_\mathrm{F})$ is finite. Opening of a band gap at the Fermi level is not a prerequisite for insulating behaviour. The localisation of wavefunctions due to the presence of disorder is called the *Anderson localization* and the associated insulators the *Anderson insulators*, which is distinguished from band insulators by a finite density of states at the Fermi level.

We can examine the problem of localization and charge transport in disordered system with a tight-binding model with a single electron state per site (atom). Neglecting

electron-electron interactions and electron spin we can write the Hamiltonian as:

$$H = \sum_i \varepsilon_i c_i^\dagger c_i - \sum_{i \neq j} t_{ij} c_i^\dagger c_j \ , \tag{2.2}$$

where ε_i is the energy of the electron at the site i, $c_i^\dagger$ and c_i are the creation and annihilation operator of the electron state at the site i, and t_{ij} is the hopping integral between sites i and j. In an ordered system, where ε_i are identical for all sites, and we only consider hopping between nearest neighbours $t_{i(i+1)} = t$ the tight-binding model would produce extended Bloch states in a band of width $D = 2zt$, where z is te number of nearest neighbours. In a disordered system the values of the site energies ε_i and the hopping integrals t_{ij} between them would vary randomly. The former is called diagonal disorder, the latter off-diagonal or structural disorder. For simplicity the Anderson model assumes that off-diagonal disorder is negligible, and we only consider nearest neighbour hopping with the same hopping integral $t_{i(i+1)} = t$. Although, for a full description of an amorphous system with varying separation between nearest neighbours, off-diagonal disorder should be considered. Nonetheless, this simplified model will provide a good qualitative picture of the disorder induced localization. The effect of disorder is introduced in the system through a random and uncorrelated distribution of site energies ε_i, i.e. energy of a particular site is independent of the energies at other sites. The energy distribution is assumed uniform over some interval W, that is, the probability distribution of the site energies is:

$$P(\varepsilon) = \begin{cases} \frac{1}{W} & |\varepsilon| \leq \frac{W}{2} \ , \\ 0 & |\varepsilon| > \frac{W}{2} \ . \end{cases} \tag{2.3}$$

However, other distribution functions, such as Gaussian and Lorentzian can be used [56]. This is the so-called the *Anderson model* and can be visualized as a set of periodically spaced potential wells of varying depth, see Figure 2.1.

The exact solutions to the Anderson model are only known in one dimension, where states are localized for any small amount of disorder. Nonetheless, we can gain a qualitative understanding of the disordered system. We start by observing two limiting cases. When there is no disorder $W = 0$ (all sites possess the same energy), the electron wavefunctions are Bloch waves extending over the whole system. On the other hand, when there is no overlap $t = 0$, the states are localised to the sites and the electron wavefunctions are the site wavefunctions.. What interests us, though, is what happens between these extremes. Anderson found that for a sufficiently large W/t, all states are localised

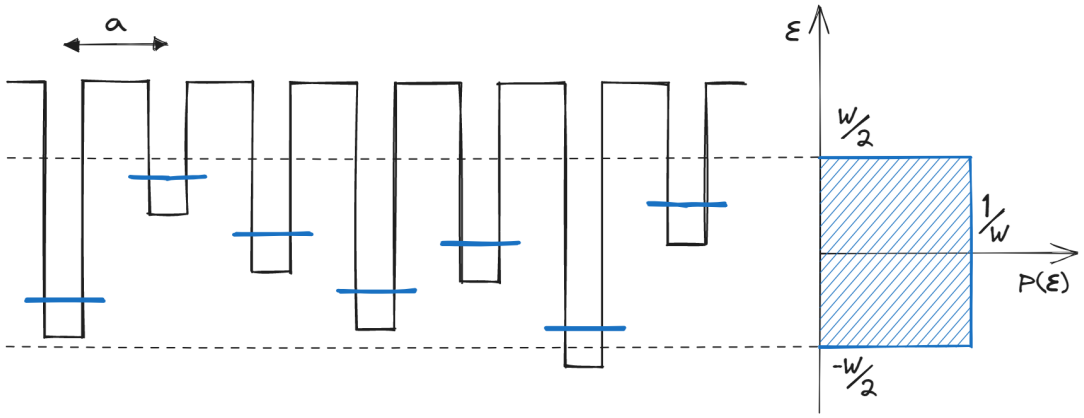

Figure 2.1: Illustration of the Anderson model. A set of periodically spaced potential wells of varying depths. After [111].

and there exists a critical value of $(W/t)_c$ below which delocalised states appear in the middle of the band.

For a given value of $0 < W/t < (W/t)_c$ localised states can be found at the band edges, see Figure 2.2. These localised states are separated from delocalised states by a sharp boundary at some energy level E_{C} (or E'_{C}) called the *mobility edge*. If the Fermi level of a material is found in the delocalised region of the band the material will exhibit metallic behaviour and conduction will involve diffusion of conduction electrons through the material. On the other hand, if the Fermi level is in the localised region the material will exhibit insulating properties and the conduction will proceed either through hopping between localised states or activation to the delocalised state above the mobility edge. This type of transition from metal to insulator, either due to the change in disorder W/t or the position of the Fermi level, is called the *Anderson metal-insulator transition* (MIT).

A better understanding of this model can be obtained by examining the simplest case of two potential wells, which when isolated from each other, have electron energies ε_1 and ε_2 and corresponding wavefunctions ϕ_1 and ϕ_2. The electron wavefunctions of the interacting system are then:

$$\begin{aligned} \psi_I &= c_1\phi_1 + c_2\phi_2 \ , \\ \psi_{II} &= c_2\phi_1 + c_1\phi_2 \ . \end{aligned} \tag{2.4}$$

The exact solutions of c_1 and c_2, and the energies of the two wavefunctions E_I and E_{II} are rather complicated, but it will be sufficient to examine the two limiting cases [112, 113].

If the energy difference of the two wells is small compared to the hopping integral, i.e. overlap of ϕ_1 and ϕ_2, $|\varepsilon_1 - \varepsilon_2| \ll t$, then $c_1 \sim c_2$ and $E_I - E_{II} = 2t$. In this case

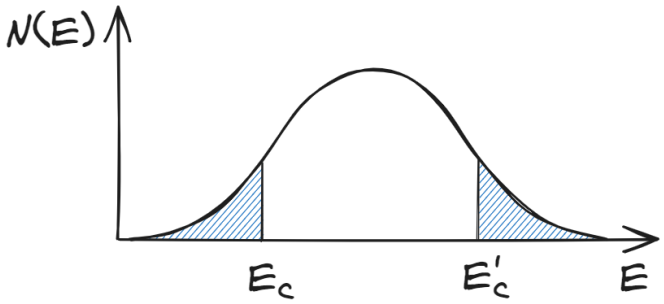

Figure 2.2: Illustration of the density of states of a band in the Anderson model, with delocalized states in the centre of the band and localized states (marked with blue hatching) at the band edges. Energies E_{C} and E'_{C} demarcate the regions of delocalized and localised states at the so-called mobility edge. After [112].

electron is equally shared between the two wells, i.e. the wells have an equal probability of containing the electron. Here we can observe, that in case $\varepsilon_1 = \varepsilon_2$ the electron is shared between the wells no matter how far apart they are, i.e. how small the hopping integral is. As a consequence two states of the same energy in the band must simultaneously be localized or delocalised; for if one is delocalized and the two are connected then the other must be too. This is an argument for the existence of the *sharp* mobility edge separating localised and delocalised states in the band [112].

If the energy difference of the two wells is large compared to the hopping integral, $|\varepsilon_1 - \varepsilon_2| \gg t$, then $c_2/c_1 = t/|\varepsilon_1 - \varepsilon_2|$. This ratio increases exponentially with increasing separation of the wells. In this limit, the energy E_I (E_{II}) and wavefunction ψ_I (ψ_{II}) of state I (II) are close to the isolated well energy ε_1 (ε_2) and wavefunction ϕ_1 (ϕ_2). Therefore, each state corresponds to the electron being in one well or the other, there is no collectivization of the electron.

From the example of two wells, we can construct an image of an infinite array of wells, following the arguments of [113, 114]. If the energy of two sites is found within a energy band $-\Delta/2 < E < \Delta/2$, where energy E is well within the range of site energies ε_i and the bandwidth is of the order of t, they are called *resonant*, and if they are outside this band they are called *nonresonant*. The implication of this definition is that if two resonant sites are nearest neighbours, they share an electron state.

Two resonant sites are also connected if they are linked by a chain of connected nearest neighbour resonant sites. All such connected resonant sites form a cluster. The absolute value of the electron wavefunction is roughly constant across all sites of the cluster and negligible outside.

In the following, we disregard all nonresonant sites. With this step, we also disregard the coupling of two resonant sites separated by a nonresonant site, but the effective overlap integral of these resonant sites will be t^2/W, instead of t. If t/W is small (the limit of large disorder), we can safely neglect coupling via nonresonant sites. Therefore, the extent of the wavefunction is determined by the size of the resonant cluster.

In the Anderson model the site energies are uniformly distributed in an interval W. Therefore, the fraction of resonant sites is of the order t/W. If t/W is small there are only finite isolated clusters. When t/W is increased to some critical value and an infinite cluster of resonant sites is formed, the electron wavefunction spreads infinitely over the infinite cluster. In other words the material exhibits a change from insulating behaviour of isolated cluster to metallic behaviour of the infinite cluster.

The value of $(\Delta/W)_c$ can be determined with percolation theory, and it corresponds to the site problem percolation threshold for a given lattice. To estimate the critical value of $(W/t)_c$, a connection between the bandwidth Δ and the hopping integral t needs to be found. B. I. Shklovskii and A. L. Efros [113] propose that, since at the percolation threshold the infinite cluster is formed from a practically one-dimensional chain, it is natural to take the one-dimensional chain bandwidth as the resonant bandwidth $\Delta \approx 4t$. While this approach is crude, it gives good agreements between $(W/t)_c = 4/(\Delta/W)_c$ and $(W/t)_c$ from computer simulations.

2.2 Variable range hopping

In a system where all states near the Fermi level are localised at the absolute zero $T = 0\,\mathrm{K}$, all electrons will be trapped in the localised states and no conduction can occur. If the temperature is high enough, electron in the localised states can be excited into empty delocalised states above the mobility edge at E_C, or in case the whole band is localised to the nearest empty states in a delocalized band E_D. At low temperatures, above the absolute zero $T = 0\,\mathrm{K}$, the energy required to jump to the mobility edge $E'_\mathrm{C} - E_\mathrm{F}$ or an empty delocalised band $E_\mathrm{D} - E_\mathrm{F}$ might be higher than the available thermal energy $k_\mathrm{B}T$. Nevertheless, even in this regime the electrons can move by thermally activated tunnelling, hopping, between localised states, if there is a finite overlap between their wavefunctions. This transfer is accompanied by an absorption or emission of a phonon to account for the energy difference between the states.

The conductivity of the system is proportional to the probability of hopping between

two localized states [113]:

$$\sigma \propto \exp\left(\frac{-2R}{\xi} - \frac{\Delta\varepsilon}{k_{\mathrm{B}}T}\right) , \tag{2.5}$$

where R is the distance and $\Delta\varepsilon$ is the energy difference between two localized states. The first component represents the probability of tunnelling between localised wavefunctions, which decay exponentially with distance, see Expression (2.1), and therefore have small finite overlaps. The second term corresponds to the probability of thermal activation, that is, of finding a phonon with the necessary energy $\Delta\varepsilon$ to complete the hop between states with different energies. The first term favours shorter distance hops, while the second term prefers longer distances, as this increases the probability of finding states that are closer in energy. Therefore, an electron might have a higher probability of hopping to a spatially distant state if the energy difference between them is smaller. This mechanism is referred to as *variable range hopping* (VRH).

Assuming constant density of states near the Fermi level $N(E_F)$ The number of states inside a d-dimensional sphere of radius R within an energy interval ΔE is

$$CR^d N(E_{\mathrm{F}})\Delta E , \tag{2.6}$$

where C is a constant. Therefore the smallest energy difference between states an electron sees inside a radius R is:[a]

$$\Delta\varepsilon = \frac{1}{CR^d N(E_{\mathrm{F}})} . \tag{2.7}$$

By substituting Equation (2.7) into Equation (2.5), we find an expression:

$$\sigma \propto \exp\left(\frac{-2R}{\xi} - \frac{1}{CR^d N(E_{\mathrm{F}})k_{\mathrm{B}}T}\right) , \tag{2.8}$$

in which the first component ($\propto R$) increases, and the second component ($\propto 1/R^d$) decreases with increasing distance R. Consequently, there should be an optimal hopping distance R_{optimal}, that minimizes this expression. To find R_{optimal}, we differentiate the expression with respect to R, equate it to zero, and obtain:

$$R_{\mathrm{optimal}} = \left(\frac{\xi d}{2CN(E_{\mathrm{F}})k_{\mathrm{B}}T}\right)^{\frac{1}{d+1}} . \tag{2.9}$$

Assuming that hops with optimal hopping distance dominate the conductivity, the fol-

[a] The smallest energy interval ΔE needed to find one state at a distance R

lowing expression can be obtained:

$$\frac{1}{\rho(T)} = \sigma(T) = \sigma_0 \exp\left[-\left(\frac{T_{0\mathrm{d}}}{T}\right)^{\frac{1}{d+1}}\right] . \tag{2.10}$$

VRH characterized by this temperature dependence of conductivity (resistivity) is know as Mott VRH, after N. F. Mott who first proposed this type of hopping [115]. The temperature exponent depends on the dimension of the system d, with values of 1/4 for three-, 1/3 for two-, and 1/2 for one-dimensional systems.

The treatment presented here is only qualitative. A proper determination of $T_{0\mathrm{d}}$ requires a more intricate derivation involving percolation methods [113].

According to Equation (2.9), the optimal hopping distance decreases with temperature and at one point becomes comparable to the distance between nearest neighbours. When this occurs the conductions is confined to hopping between nearest neighbours, and only the second component of Equation (2.5) is temperature dependent. The conductivity exhibits an activation like behaviour:

$$\frac{1}{\rho(T)} = \sigma(T) = \sigma_0 \exp\left(-\frac{A}{T}\right) , \tag{2.11}$$

where A represents the average energy difference between nearest neighbours. This type of hopping is called *nearest neighbour hopping* (NNH).

In deriving the Mott VRH hopping we assumed that the density of states is constant around the Fermi level, however, A. L. Efros and B. I. Shklovskii showed that due to Coulomb interaction the density of states vanishes at the Fermi level [116].

We start with a system in ground state, i.e. all the electron states above the Fermi level E_{F} are empty and all states below are full. It is convenient to first redefine the energies with respect to the Fermi level:

$$\epsilon = E - E_{\mathrm{F}} . \tag{2.12}$$

The energy required to transfer an electron from an occupied state $\epsilon_i < 0$ to an unoccupied state $\epsilon_j > 0$ that are separated by a distance r_{ij} is:

$$\Delta E_{i\to j} = \epsilon_j - \epsilon_i - \frac{e^2}{\kappa r_{ij}} , \tag{2.13}$$

where κ is the relative permittivity.[b] The third term $e^2/\kappa r_{ij}$ compensates for the self interaction of the electron in state j with the now empty state i. This expression can be better understood if the excitation process is performed in two steps. First we move the electron from state i to infinity, and in the second step we bring it back to state j. The work required for the first step is $-(\epsilon_i + E_\mathrm{F})$. The work required for the second step would be $\epsilon_j + E_\mathrm{F}$ if state i is still occupied, i.e. the system was in the ground state. However, in the second step the donor i is empty and when calculating the work we must treat state i as if it contains a positively charged hole. The attraction between the electron and the hole diminishes the required work by $e^2/\kappa r_{ij}$

Since the starting system was in the ground state, the transfer energy $\Delta E_{i\to j}$ must be positive for any pair of occupied $\epsilon_i < 0$ and unoccupied states $\epsilon_j > 0$. Therefore, the smaller (closer to the Fermi level) the energies ϵ_i and ϵ_j are, the larger the separation between them has to be to satisfy $\Delta E_{i\to j} > 0$. In particular, the density of states must be zero at the Fermi level $N(E_\mathrm{F}) = 0$, as in that case the separation would have to be $r_{ij} = \infty$. This is referred to as the *Coulomb gap*. It represents a type of soft gap, where the density of states iz zero at only one point, unlike a hard gap where the density of states is zero for a range of energies (e.g., between the conductions and valence band of a semiconductor).

To determine the shape of the gap, consider all pairs of states in a small energy range $(-\epsilon/2,\epsilon/2)$. From $\epsilon_j - \epsilon_i < \epsilon$ and $\Delta E_{i\to j} > 0$, it follows that:

$$r_{ij} > \frac{e^2}{\kappa\varepsilon} \,. \tag{2.14}$$

Therefore the concentration of states[c] within the energy range $(-\epsilon/2,\epsilon/2)$ in d-dimensions is limited to:

$$n(\varepsilon) \propto \frac{1}{r_{ij}(\varepsilon)^d} < \left(\frac{\kappa\varepsilon}{e^2}\right)^d \,, \tag{2.15}$$

From this we obtain the upper limit on the density of states:

$$N(\varepsilon) = \frac{\partial n(\varepsilon)}{\partial \varepsilon} < d\left(\frac{\kappa}{e^2}\right)^d |\varepsilon|^{d-1} \,. \tag{2.16}$$

In other words, the density of states needs to fall off at least as fast as $|\varepsilon|^{d-1}$ as ε approaches the Fermi level.

Efros and Shklovskii argue [113, 116] that density of states also cannot fall off faster

[b] Using Gaussian units for simplicity. $1/4\pi\epsilon_0 = 1$

[c] number of states per unit of d-dimensional volume

than $|\varepsilon|^{d-1}$ either. Density of states $N(\varepsilon) \propto |\varepsilon|^{d-1}$ implies that states within the energy range $(-\epsilon/2,\epsilon/2)$ are on average separated by $e^2/\kappa\varepsilon$ and the interaction between them is of the order ε. If the density of states were to fall off faster, then the average distance would be greater than $e^2/\kappa\varepsilon$ and the interaction energy weaker than ε. Such a weak interaction could not result in lowering of the density of states and therefore they conclude:

$$N(\varepsilon) \propto |\varepsilon|^{d-1} \tag{2.17}$$

Returning to the problem of variable range hopping. For a d- dimensional system and an $N(E) \propto |E - E_{\mathrm{F}}|^n$ dependence of the density of states near the Fermi level, a general expression for VRH conductivity (resistivity) can be obtained [113] in of the form:

$$\frac{1}{\rho(T)} = \sigma(T) = \sigma_0 \exp\left[-\left(\frac{T_0}{T}\right)^p\right] , \tag{2.18}$$

where the exponent p is obtained from:

$$p = \frac{n+1}{n+d+1} . \tag{2.19}$$

Mott VRH is retrieved with $n = 0$, $p = 1/(d+1)$. On the other hand, the $n = d-1$ dependence of the density of states due to the Coulomb gap results in an exponent of $p = 1/2$, independent of the system dimension:

$$\frac{1}{\rho(T)} = \sigma(T) = \sigma_0 \exp\left[-\left(\frac{T_{\mathrm{ES}}}{T}\right)^{\frac{1}{2}}\right] . \tag{2.20}$$

This type of VRH due to the Coulomb gap is called the *Efros-Shklovskii VRH* (ES VRH).

2.2.1 VRH in Granular Metals

A different type of VRH has been observed in granular metals, which cannot be described by either Mott or ES VRH. Granular metals are composite materials of metals and insulators. The most common forms are granular metal films and cermets.

Granular metal films are created by depositing metals onto an insulating substrate. The materials are chosen so that the metal does not wet the substrate surface, leading to the formation of metallic islands on the substrate surface, as seen in Figure 2.3(a). A material consisting of metallic grains embedded in an insulating matrix, in this case air or vacuum, is thus obtained. Additional metal deposition causes the metal regions to

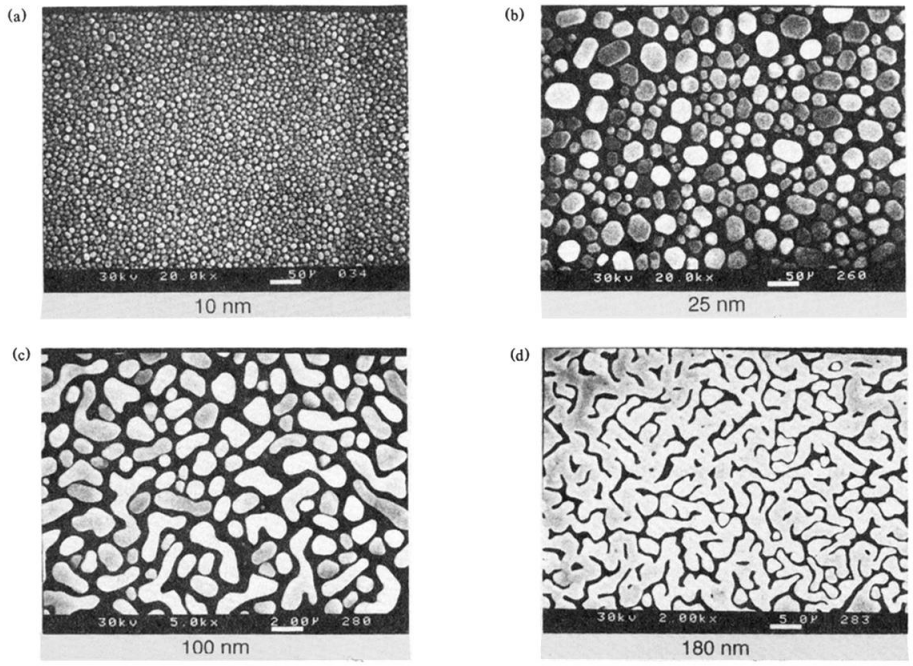

Figure 2.3: Scanning electron microscope images of indium evaporated onto SiO_2 at room temperature. The average film thickness is provided below each photograph. (**a**), (**b**) Growth and coalescence of islands; (**c**) elongated structures; (**d**) percolation. Reproduced from [117]

expand, as shown in Figures 2.3(b) and 2.3(b), until a percolation threshold is reached, and a single metallic region is formed. In other words, insulating regions are now separated by a metallic matrix.

Cermets, on the other hand, are produced by the simultaneous deposition of a metal and an insulator that do not dissolve into each other. Depending on the metal-to-insulator ratio, similar structural features to those in the films are obtained.

When the concentration of metal x is low, the metallic granules are isolated, and the system exhibits insulating properties. For high metal concentrations, above a critical percolation concentration x_c, the metal granules touch and form a continuum, thus exhibiting metallic properties. An interesting early observation in the insulating regime was the appearance of an ES-like VRH temperature behaviour of resistivity, described by the Expression (2.20) [118], examples of which can be seen in Figure 2.4. This temperature behaviour is quite pervasive, appearing for both metallic and semiconducting, irregular and periodic granular arrays [119].

Values of T_{ES} have been observed in a wide range of values, from 185 K for high metal concentrations ($x = 0.38$) in Au-Al_2O_3 to 51 000 K for low metal concentrations in Ni-SiO_2 ($x = 0.08$) and Pt-SiO_2 ($x = 0.04$) cermets [118]. Furthermore, in W-Al_2O_3

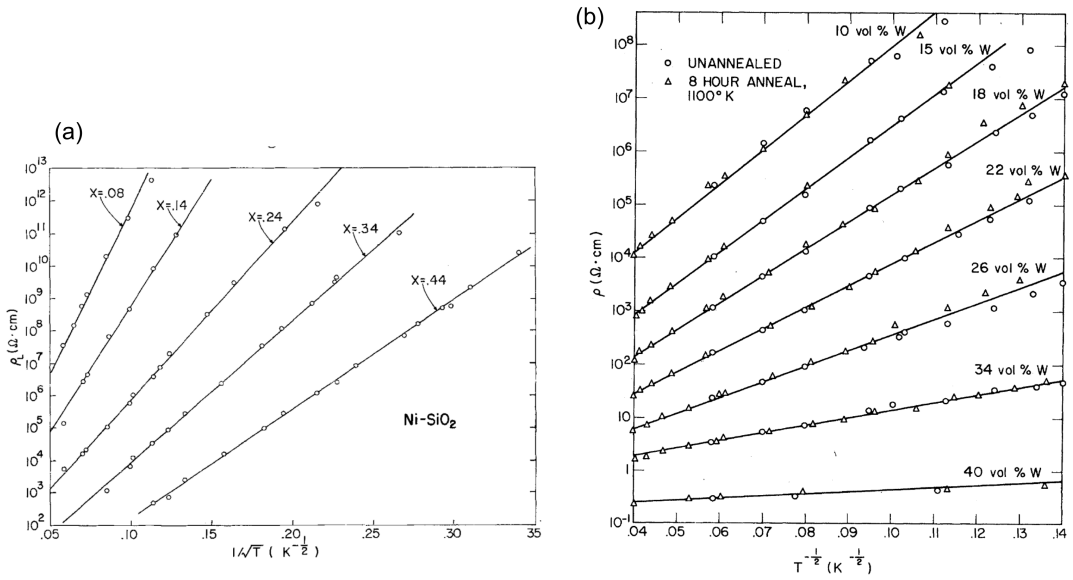

Figure 2.4: Resistivity of the (**a**) Ni-SiO_2 and (**b**) W-Al_2O_3 cermets (granular metals) vs $T^{-1/2}$. On the (a) panel x indicates the volume fraction of Ni. On the (b) panel the open circles are for the samples before annealing and open triangles for samples after annealing. The resistivities of annealed samples were normalized to sample resistivities at 300 K before annealing. Penal (a) was reproduced from [118] and panel (b) from [120].

cermet, it was observed that T_{ES} does not change when the samples are annealed at high temperatures, while the pre-exponential factor of resistivity ρ_{VRH} increases by several orders of magnitude, as shown in Figure 2.4(b). W does not precipitate with annealing and remains uniformly dispersed within the insulator, i.e. the metal concentration remains unchanged, but the size of the metal grains increases. This indicates that T_{ES} is insensitive to the distribution of the metal grains in these systems and is solely a function of the metal's volume fraction [120].

When discussing isolated metallic granules in the insulating regime, two additional parameters need to be considered. The first is the discreet electron energy levels due to electron confinement within a single grain. The mean level spacing in a grain is :

$$\delta = \frac{1}{N(E_{\mathrm{F}})V} \,, \tag{2.21}$$

where V is the volume of the grain. For granules of several nanometers, the spacing δ is typically of the order of several kelvins. For example, for an aluminium particle with radius of 5 nm the spacing is ≈1 K [119]. From here on, we will focus on the temperature range where quantum size effects are not significant.

The second parameter is the Coulomb charging energy required to add or remove an electron from a neutral grain:

$$E_{\mathrm{ch}} = \frac{e^2}{2\kappa a} \ , \tag{2.22}$$

where a is the granule radius.[d] This energy represents the amount required to charge a granule in isolation, without considering the interactions among other granules, i.e. it does not account for the inter-granule interactions.

Electrical conduction in the insulating regime arises from the transport of electrons and holes between isolated metallic grains. In the ground state, all the metal grains are neutral. To create charge carriers, an electron must be transferred between two neutral grains, generating a pair of positively and negatively charged grains, or in other words, an electron-hole pair. Since the transfer of an electron between two neutral grains requires considerable energy $2E_{\mathrm{ch}}$, a hard gap is present in the excitation spectrum. This can be considered analogous to a Mott gap in a Mott insulator, where E_{ch} plays the role of the repulsive Coulomb potential U [118, 119]. In the limit of weak electric fields,[e] the charge carriers are thermally activated, and the number of electron-hole pairs follows the Boltzmann distribution. Consequently, conductivity will exhibit an activation dependence:

$$\sigma(T) = \sigma_0 \exp\left(-\frac{E_{\mathrm{ch}}}{2k_{\mathrm{B}}T}\right) \ . \tag{2.23}$$

However, as previously mentioned, the activation behaviour is typically not observed in granular metals; instead, ES-like VRH is observed.

The initial explanation for this discrepancy was provided by B. Abeles et. al. [118]. Here, only a simplified derivation will be presented, keeping the key arguments. The charging energy is defined as:

$$E_{\mathrm{ch}} = \frac{e^2}{2\kappa a} F\left(\frac{s}{a}\right) \ , \tag{2.24}$$

where s is the separation between grains, and $F(s/a)$ is a function that depends on the shape and arrangement of grains. The primary assumption is that the ratio between the grain radius a and the separation between grains s, i.e. the insulating layer thickness, remains constant in a sample. Given a uniform composition throughout a sample up to a small subregion, larger grains must be separated further than smaller grains in order to maintain the uniform sample composition. As a result $s/a = \text{const.}$, and depends solely

[d] The granules are assumed to be isolated spherical capacitors $C = \kappa a$ and the energy to charge capacitors is $E_{\mathrm{ch}} = 1/2 \cdot Q^2/C = e^2/2\kappa a$.

[e] $e\Delta V < k_{\mathrm{B}}T$, where ΔV is the voltage drop between neighbouring metal grains due to the external field.

on the metal volume concentration x. It follows from Equation (2.24), that the product sE_{ch} is a constant as well.

Since there is a variation in size and shape of individual granules there will be a distribution of charging energies E_{ch}. Once an electron-hole pair with some charging energy E'_{ch} is created, they will move through the sample by tunnelling between grains. They are prevented from tunnelling to grains of higher charging energy due to insufficient energy, and to grains of smaller charging energy due to larger tunnelling barriers resulting from the $sE_{\mathrm{ch}} = \text{const.}$ constraint. Therefore, once charges are created they will move through the sample following an optimal path of least deviation of charging energies from E'_{ch}.

The corresponding mobility is then given by the tunnelling probability

$$\exp(-2\chi s) \ , \quad \chi = \frac{1}{\hbar}\sqrt{2m_e U_{\mathrm{eff}}} \tag{2.25}$$

where U_{eff} is the effective brier height and m_e is the electron mass. And since the number of charge caries is given by the Boltzmann distribution, the conductivity is given as:

$$\sigma \propto \exp\left(-2\chi s - \frac{E_{\mathrm{ch}}}{2k_{\mathrm{B}}T}\right) = \exp\left(-2\chi s - \frac{T_0}{8\chi s T}\right) \tag{2.26}$$

where in the second step we introduce a constant $T_0 = 4\chi s E_{\mathrm{ch}}/k_{\mathrm{B}}$.

Similar to Equation (2.8) we can observe a component of the conductivity that increases with s and another that decreases. Therefore, assuming there is a distribution of s as a result of a distribution of a, there will be an optimal distance:

$$s_{\mathrm{optimal}} = \frac{1}{4\chi}\sqrt{\frac{T_0}{T}} \ . \tag{2.27}$$

Assuming that the current flows mainly through the path set ba s_{optimal}, substituting (2.27) into (2.26), the characteristic ES VRH Expression (2.20) is obtained.

This model has been criticized on multiple assumptions. Based on measurements, the ratio of the grain radius a and grain radius s is not constant [121]. The random variation capacitance cannot lift the hard gap at the Fermi level, as that would require macroscopic grain sizes ($C \propto 1/a$) [122]. Furthermore ES VRH temperature dependence of resistivity was observed in periodic arrays of quantum dots and artificially manufactured metallic periodic granular systems where the size of the granules and the periodicity in the dot arrangement were controlled within a few percent accuracy [119].

Two key issues must be addressed in order to fully explain the ES VRH conductivity in granular materials [119]. First, the underlying mechanism governing tunnelling over extended distances must be identified. Second, the problem of the hard gap must be resolved, specifically the origin of the finite density of states in proximity of the Fermi level and the role of Coulomb interactions in shaping the density of states.

Unlike localised states discussed in the previous section 2.2, where even distant localised states have finite overlaps between exponentially decaying wavefunctions, the range of tunnelling in granular materials is non-trivial, as each grain is typically connected by tunnel junctions only to its nearest neighbours. The mechanism for long range tunnelling in granular materials has been attributed to co-tunnelling (elastic or inelastic) of electrons between distant granules via a chain of intermediate virtual states [119].

Before proceeding, a clarification should be added here. The density of states of a granule describes the energy levels of an electron in a single granule. When placing an electron into a granule, multiple states with similar energies are typically available for the electron to occupy ($\delta \ll$). For hopping purposes, these states are considered equivalent since finding at least one state is enough to ensure transport. Therefore, when constructing a density of states relevant for hopping, only the lowest excited state of each grain should be considered, resulting in the single-particle density of states of the granule system, known as the *density of ground states* [119, 122]. It is this density of ground states that exhibits a gap at the Fermi level due to the Coulomb charging energy required to form a conducting electron-hole pair.

J. Zheng and B. I. Shklovskii [122] successfully addressed the hard gap issue. The presence of charge impurities in the insulating layer leads to random charging of metallic granules in the global ground state. In the case of low metallic granule density, this is due to the random positioning of granules, and in the case of high density, it is due to the random positioning of impurities. These charge fluctuations smear the density of ground states, which at high enough levels of charge impurities leads to closing of the hard gap at the Fermi level. In other words, the charge disorder present the in insulating layer leads to a reduction in the Coulomb charging energy for some granule pairs within the system.

The density of ground states is then suppressed at the Fermi level by incorporating long-range Coulomb interactions between granules $e^2/\kappa_{\text{eff}} r_{ij}$, where κ_{eff} is the effective relative permittivity of the granular metal. To clarify, up to this point when considering the effects of granule charging we have treated the granules as isolated from each other, i.e. we have not considered the effects of Coulomb interactions when charging two neutral granules. Removing an electron and thereby charging the first granule requires E_{ch} energy,

but due to the attraction between the electron and the positively charged first granule, it only takes $E_{\mathrm{ch}} - e^2/\kappa_{\mathrm{eff}} r_{ij}$ energy to place an electron on the second granule. In a similar fashion as outlined for localised states in the previous section 2.2, these interactions than result in the appearance of the Coulomb soft gap in the density of ground states at the Fermi level.

2.3 Lifshitz model

The Anderson model assume that off-diagonal (structural) disorder is negligible. However, this is not the case in disordered amorphous systems. A alternative model that explores off-diagonal disorder is the so-called *Lifshitz model*, initially proposed by I. M. Lifshitz [123], and later utilized by B. I. Shklovskii and A. L. Efros to describe the metal-insulator transition [113].

The model consists of identical potential wells, randomly distributed in space with a concentration n_{w}, as illustrated in Figure 2.5. The model considers only one electron per well (site). Since all the wells have the same energy ε_0, diagonal disorder is absent, and the model solely addresses off-diagonal (structural) disorder. This stands in contrast to the Anderson model, which exclusively considers diagonal disorder.

In order to examine localization, we assume that the mean separation between the wells is large compared to both the well size and the radius of the single-well wave function. The single-well wavefunctions far from the well can be approximated by the Expression (2.1). Following the discussion in section 2.1 regarding resonant sites in the Anderson model, it can be inferred that since all the wells possess the same energy level ε_0, all the wells are resonant and only collective delocalized states would form. However, the resonant interaction will be stronger for pairs of nearest neighbour wells. These resonant pairs will form collective states similar to Expression (2.4), which subsequently shifts their energies levels to:

$$\varepsilon_0 \pm \lambda \frac{\exp\left(-\frac{R_{12}}{\xi}\right)}{R_{12}} , \tag{2.28}$$

where λ represents a value dependent on the well characteristics and the material's permittivity, and R_{12} is the distance between neighbouring wells forming a resonant pair. As this distance varies for each pair, the energy shift will also differ.

Not all wells will form resonant pair. Consider a well (3) whose nearest neighbour (2) has a different nearest neighbour (1), such that $R_{12} < R_{23}$, as illustrated in Figure 2.5. In this case, wells (1) and (2) will form collective states with energies described by

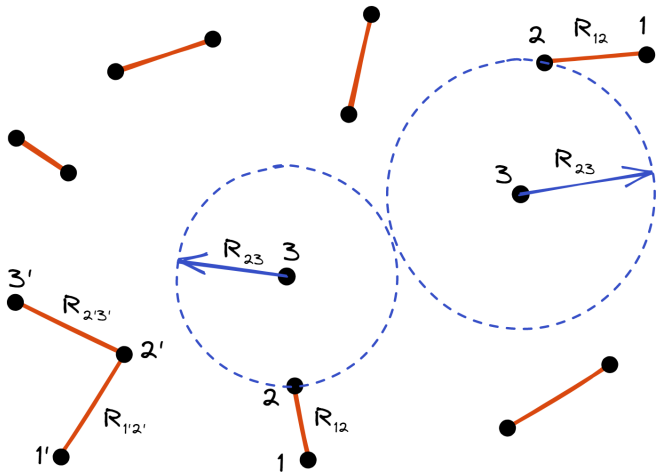

Figure 2.5: Illustration of the Lifshitz model. Black dots represent randomly distributed identical potential wells. Orange lines indicate resonant pairs and triplets of neighbouring wells that form collective states. Isolated wells (3) are formed when its the nearest neighbour (2) has a closer neighbour (1); such that $R_{12} < R_{23}$. Collective states equally shared by three wells can form when a well (2') has two equidistant neighbouring wells (1',3'); when $R_{1'2'} = R_{2'3'}$. After [111] and [123].

Equation (2.28), while the state on well (3) will remain localized with a minor admixture of neighbouring wavefunctions producing a small shift in energy $\propto \exp(2R_{23}/\xi)$.

For three wells to equally share a collective state, well (2) would have to be equidistant from wells (1) and (3), such that $R_{12} = R_{23}$. For a collective state to form, this equality can be violated by at most the localisation length ξ [113]. These implies that if the mean separation between wells $n_{\mathrm{w}}^{-1/3}$ greatly exceeds the localization length ξ, the probability of finding three of more wells forming collective states becomes exceedingly small. As a result, all electrons will be localised to individual wells or resonant pairs of neighbouring wells.

The Lifshitz model significantly differs from the Anderson model. In the Anderson model, energy dispersion and overlap between neighbouring sites are governed by two separate parameters, W and t. The ratio of these parameters determines whether the system is localized or not. Conversely, in the Lifshitz model, energy dispersion and overlap are controlled by a single parameter: the average separation between wells, $n_{\mathrm{w}}^{-1/3}$. Localization of the system occurs when the average separation between wells is much greater than the single-well wavefunction localization length, ξ, i.e., when $n_{\mathrm{w}}^{-1/3}/\xi \gg 1$.

Chapter 3

Samples and Experimental Methods

This chapter is divided into four sections, with the first two focusing on the samples measured as a part of this work, and the latter two describing the experimental setup and techniques employed for the measurements.

Section 3.1 details the manufacturing and prior work on the chemical and structural characterization of metallic glass ribbon samples of quinary TE-TL alloys. Section 3.2 describes the procedures and setups employed to fabricate and characterize amorphous thin films of TiZrNbCuNi. Section 3.3 describes the techniques used to measure and analyse resistance, magnetoresistance, and the Hall effect. Finally, Section 3.4 outlines the experimental setup used to perform measurements from room temperature down to 300 mK and in magnetic fields up to ± 16 T.

3.1 Metallic glass ribbon samples

In this work, we explore metallic glass thin ribbon samples of three similar quinary TE-TL alloy systems: $(\mathrm{TiZrNbCu})_{1-x}\mathrm{Ni}_x$, $(\mathrm{TiZrNbNi})_{1-x}\mathrm{Cu}_x$ and $(\mathrm{TiZrNbCu})_{1-x}\mathrm{Co}_x$ (hereinafter referred to as Ni_x, Cu_x and Co_x, respectively). Seven different compositions of Ni_x (x = 0.125, 0.15, 0.20, 0.25, 0.35, 0.43, 0.50), seven of Cu_x (x = 0.0, 0.12, 0.20, 0.25, 0.32, 0.43, 0.50) and five of Co_x (x = 0.10, 0.20, 0.25, 0.32, 0.43) were prepared and studied. Additionally, three alloys variants with fixed (CuNi) content, with nominal compositions: $\mathrm{Ti}_{0.30}\mathrm{Zr}_{0.15}\mathrm{Nb}_{0.15}\mathrm{Ni}_{0.20}\mathrm{Cu}_{0.20}$, $\mathrm{Ti}_{0.15}\mathrm{Zr}_{0.30}\mathrm{Nb}_{0.15}\mathrm{Ni}_{0.20}\mathrm{Cu}_{0.20}$, and $\mathrm{Ti}_{0.15}\mathrm{Zr}_{0.15}\mathrm{Nb}_{0.30}\mathrm{Ni}_{0.20}\mathrm{Cu}_{0.20}$ (hereinafter referred to as $\mathrm{Ti}_{0.30}$, $\mathrm{Zr}_{0.30}$ and $\mathrm{Nb}_{0.30}$, respectively), were also investigated. These three samples possess varying concentrations of TE elements while maintaining the same TE/TL ratio as $(\mathrm{TiZrNb})_{0.6}(\mathrm{NiCu})_{0.4}$, which is the same composition as $\mathrm{Ni}_{0.20}$ and $\mathrm{Cu}_{0.20}$.

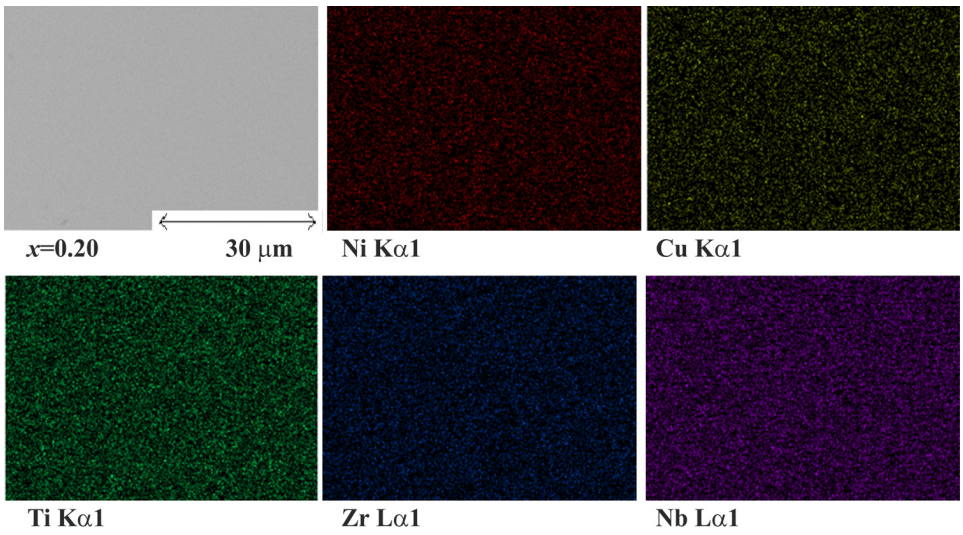

Figure 3.1: SEM image and EDS element maps of Ni K_α, Cu K_α, Ti K_α, Zr L_α, and Nb L_α, peaks of TiZrNbNiCu. Reproduced from [22].

All the metallic glass ribbon samples were prepared by Dr. I. A. Figueroa at the *Institute for Materials Research-UNAM, Mexico*. For each alloy composition, ingots were prepared from high purity components ($\geq$ 99.8 at.%) by arc melting in high purity argon in the presence of a titanium getter. The ingots were flipped and re-melted five times to ensure thorough mixing of the components. Thin ribbons were fabricated from these ingots through melt-spinning. Molten alloys were ejected onto the surface of a rotating copper roller in a pure He atmosphere. The rotating copper roller rapidly and continuously conducts heat away (10^4-10^6 K s^{-1}) from the melt, resulting in the solidification of the material in a glassy state. This procedure yielded ribbons typically ranging 1-2 mm in width and 15-40 µm in thickness.

XRD and DSC/DTA investigations of the as-cast ribbons confirmed that all samples were fully amorphous, exhibiting broad halos in the XRD patterns, for an example see Figure 1.3(b), and a glass transition in the DSC curves, for an example see Figure 1.2(b). However, a study of the structure factors and the associated radial distribution functions, using synchrotron based HEXRD, revealed a minor nanocrystalline phase within the amorphous matrix of $Cu_{0.0}$ and $Nb_{0.30}$, see Figure 1.5 and the discussion in Section 1.2. Elemental mapping by scanning electron microscopy with energy dispersive spectroscopy (SEM/EDS) confirmed a random distribution of constituent elements down to a micrometer scale, for an example see Figure 3.1, and the calculated compositions were within 1 at.% of nominal [21–23, 124, 125].

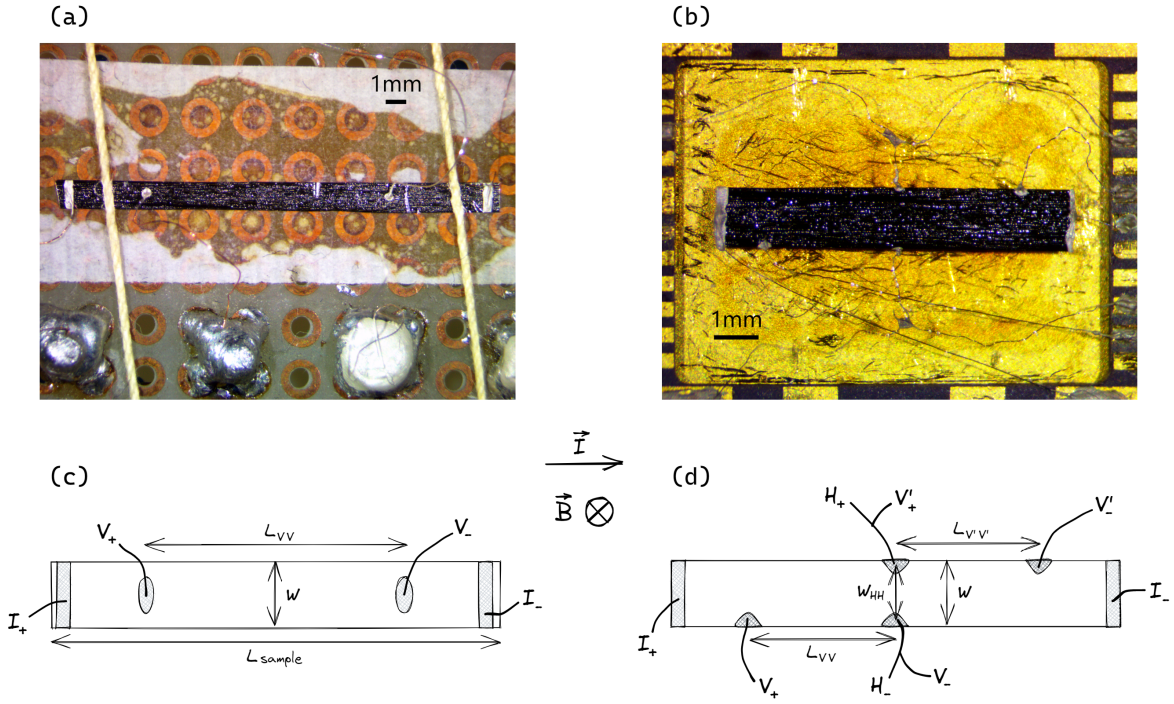

Figure 3.2: (**a**) and (**b**) show images of representative ribbon samples with applied silver paste contacts. (**c**) and (**d**) provide schematic representations of the sample and contact geometries. (**a**) and (**c**) are used for room-temperature measurements of resistivity on large samples, while (**b**) and (**d**) are used for measurements of resistivity, Hall effect and magnetoresistance in a cryostat. I_+I_- are the current contacts, V_+V_- and $V'_+V'_-$ are two pairs of redundant voltage contacts and H_+H_- are Hall contacts. The directions of electric current and magnetic field are indicated in the middle.

For the purpose of measuring resistivity, magnetoresistance, and Hall effect, ribbon samples typically 6-8 mm long were mounted on a gold-plated ceramic sample carrier with "GE" varnish, as shown in Figure 3.2(b). Prior to mounting, samples were thoroughly cleaned in an ultrasonic bath with acetone and isopropyl alcohol. Platinum wires were glued onto the samples with silver paste to make current, voltage, and Hall contacts. The silver paste was allowed to dry at room temperature, resulting in contact resistances up to 100 Ω. Two pairs of voltage contacts (V_+V_- and $V'_+V'_-$) were employed to provide redundancy during measurements, ensuring that an alternative pair is available in case one of the voltage contacts loses contact.

For the low-temperature measurements of superconductive transitions, only four contacts, two current and two voltage, were made, in the same configuration as shown in Figure 3.2(c).

Due to a large scatter in the measured resistivity of these relatively small samples, larger samples, typically 3-5 cm long, were used to measure resistivities at room-temperature, as seen in Figure 3.2(a). The same procedure for making contacts, as for small samples, was followed.

3.2 Amorphous thin film samples

In addition to the metallic glass ribbon samples, amorphous thin films were prepared using pulsed laser deposition (PLD). PLD is a thin film deposition technique that employs a focused, high-energy pulsed laser beam to vaporize target materials. The laser pulse energy is absorbed by the target, causing localized rapid heating and evaporation of the target material. This process generates a plasma plume of vaporized material that expands away from the target. As the plasma plume expands, the vaporized material reaches the substrate and begins to condense, forming a thin film on its surface. The properties of the deposited film can be controlled by various deposition parameters, such as substrate type, laser energy, fluence,[a] wavelength, pulse duration and frequency, target-to-substrate distance, substrate temperature, and background gas type (vacuum, O_2, N_2, Ar, etc.), pressure, and flow.

Figure 3.3 presents a schematic illustration of the employed pulsed laser deposition setup. The main components include the ultra-high vacuum (UHV) chamber and the Nd:YAG pulsed laser. The UHV chamber is capable of achieving vacuum levels down to 10^{-8} mbar, using a turbomolecular pump connected to a dry backing pump. The turbomolecular pump can be bypassed, and a partial pressure of an inert (N_2 or Ar) or reactive (O_2) gas can be introduced by supplying a steady flow of the desired gas and pumping the UHV chamber only through the dry backing pump.

Inside the chamber, the target and substrate are situated. The target is mounted on a target holder, which can rotate about its axis, enabling the laser beam to scan across the target. Without this rotation, the laser beam would create a deep spot in the target, negatively affecting the deposition process. Up to three target holders can be placed in the rotating target carousel, allowing for the change of the target in the laser beam's path without breaking the vacuum. Rotation of the target holder and carousel is achieved using two motors positioned atop the UHV chamber. The substrate is placed on a substrate carrier surrounded by a resistive heating element, enabling substrate temperatures up to 700 °C. A Maurer infrared radiation thermometer Series KTR 1075 is used to measure

[a] Optical energy per unit of area.

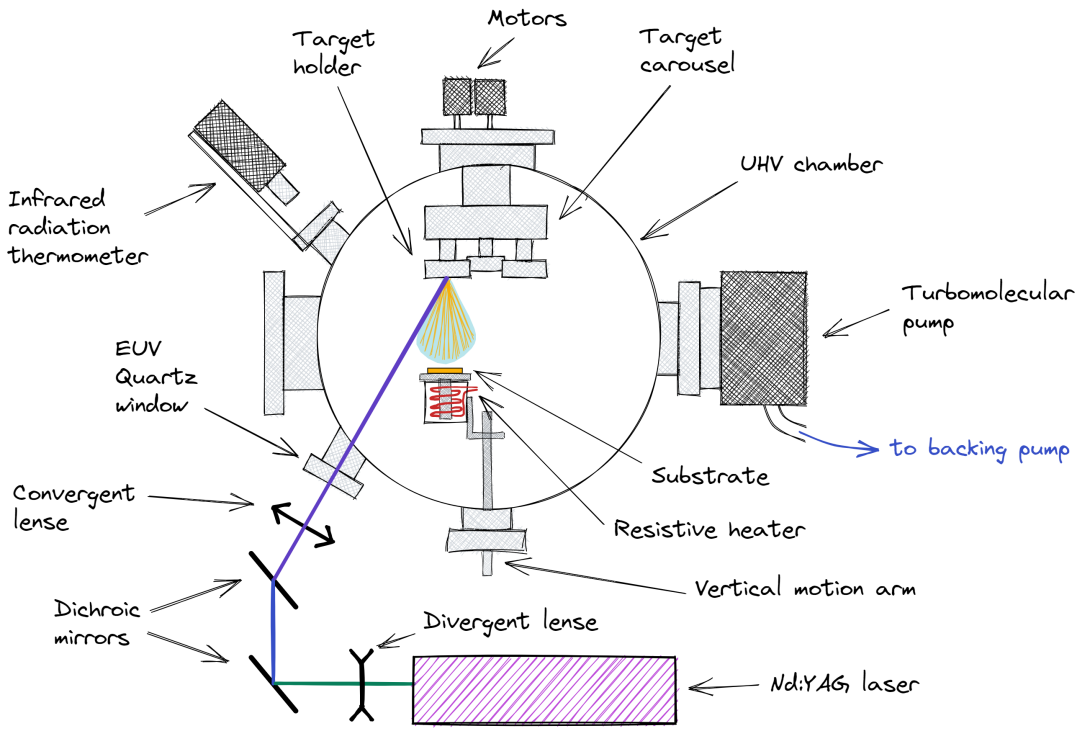

Figure 3.3: Schematic illustration of the pulsed laser deposition setup at the Department of Physics, Faculty of Science in Zagreb.

the substrate temperature through an infrared-transparent window on the UHV chamber. The target-to-substrate distance can be controlled through a vertical motion arm to which the substrate holder is attached.

The laser used in this setup is a Continuum Surelite SL II-10 Nd:YAG, with a fundamental wavelength of 1064 nm. Wavelengths of 532 nm and 266 nm can be achieved by using second and fourth harmonic generators. The laser pulse duration is in the range of 1-2 ns, and the frequency can be set in the 1-10 Hz range. Filtering (when using harmonics) and directing of the laser beam are performed by two dichroic mirrors. To prevent damage to the mirrors, the beam first passes through a divergent lens. After the mirrors, the beam passes through a convergent lens that focuses the beam onto the target. The laser beam enters the UHV chamber through a EUV quartz window that is transparent to ultraviolet light.

Using this setup, a series of thin films of TiZrNbCuNi with different deposition parameters was produced. The TiZrNbCuNi target with 99.9 % purity was supplied by Alineason GmbH (Frankfurt am Main, Germany). For the substrate, we used $5 \times 5 \times 0.5\text{mm}^3$ one side polished transparent $SrLaAlO_4$ ($a = 0.3756$ nm, $c = 1.2636$ nm) single crystals in the

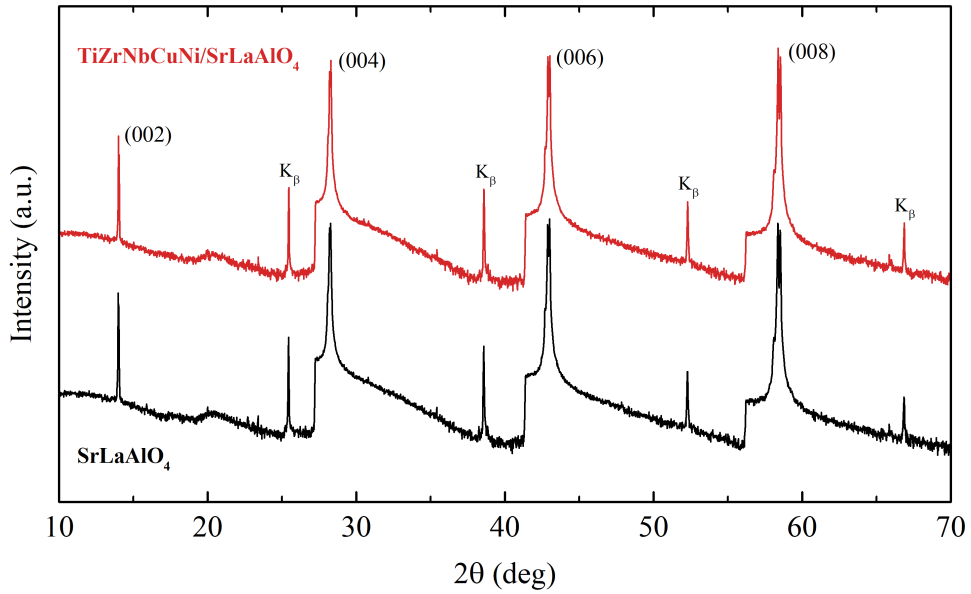

Figure 3.4: XRD patterns of TiZrNbNiCu/$SrLaAlO_4$ thin film CA011a and an as-delivered $SrLaAlO_4$ substrate. Large peaks correspond to (002)-(008) reflections on the $SrLaAlO_4$ substrate corresponding to the $c = 1.263$ nm out-of-plane lattice constant. Small peaks are the same reflections resulting from Cu K_β radiation (1.39 Å).

(001) orientation, supplied by Crystal GmbH (Berlin, Germany).

The produced films showed no signs of crystalline peaks in the XRD measurements.[b] XRD data was collected on a Bruker Discover D8 diffractometer (Karlsruhe, Germany) supplied with a LYNXEYE XE-T detector. Measurements were taken in Bragg–Brentano geometry (1D) applying Cu K_α radiation (1.54 Å). The angle 2θ was varied from 10° to 70°. The data was obtained using a step size of 0.02° and measuring time of 0.2 s/step. A representative example of an XRD measurement can be seen in Figure 3.4. The only observed sharp Bragg peaks are from the $SrLaAlO_4$ substrate. Unfortunately, due to the strong signal from the substrate, no broad diffuse halos from the amorphous state could be observed.

SEM/EDS imaging was also performed on the thin film samples.[c] A TESCAN VEGA3 SEM equipped with a tungsten filament was utilized for imaging the samples. The imaging process was carried out at a working distance of 15.3 nm and an accelerating voltage of

[b]XRD measurements were performed by T. Klaser from the Department of Physics, Faculty of Science, University of Zagreb.

[c]SEM/EDS imaging was conducted by B. Radatović from the Institute of Physics, Zagreb.

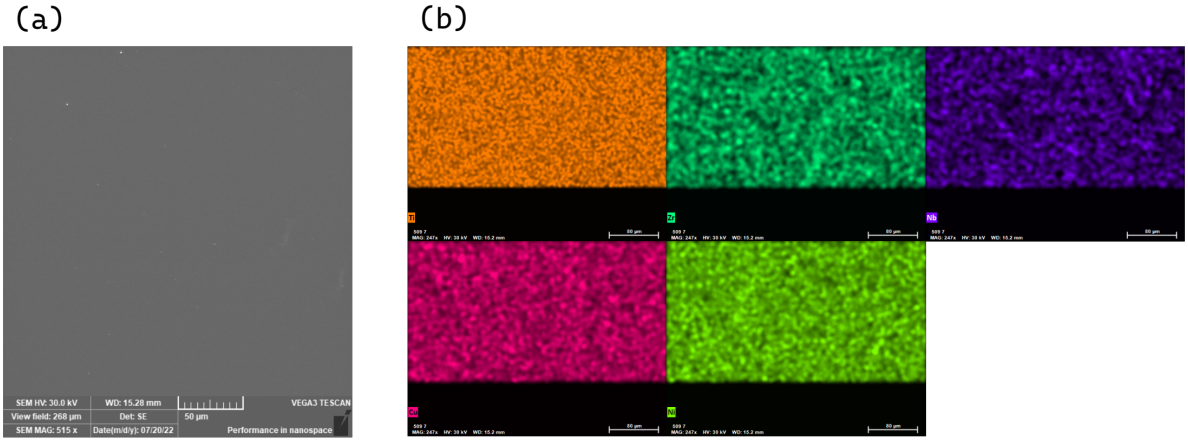

Figure 3.5: (**a**) SEM image and (**b**) EDS maps of Ni K_α, Cu K_α, Ti K_α, Zr K_α, and Nb K_α, peaks of TiZrNbNiCu/$SrLaAlO_4$ thin film CA011a.

30 kV in resolution mode using a secondary electron detector. For energy-dispersive X-ray spectroscopy (EDS) analysis, a Bruker XFlash 6l30 detector was employed, and the Esprit 2.1 software was used for spectrum analysis. A significant presence of droplets[d] and surface damage from high-energy particles in the plasma plume was observed in most of the imaged samples.

Of the produced samples, films designated as CA011a and CA011b exhibited the highest quality. They were deposited simultaneously by placing two polished transparent $SrLaAlO_4$ substrates on the substrate holder. Sample CA011a was utilized for XRD and SEM/EDS measurements, as shown in Figures 3.4 and 3.5, while sample CA011b was cut post-deposition into a smaller sample designated CA011b_1, measuring $5 \times 1.7 \times 0.5 \text{mm}^3$, to obtain a geometry more suitable for transport measurements.

The deposition parameters for TiZrNbCuNi/$SrLaAlO_4$ thin films CA011a and CA011b were as follows: laser wavelength 266 nm, fluence of $2\,\text{J}\,\text{cm}^{-2}$, pulse energy of 43 mJ, and a frequency of 10/3 Hz; deposition time of 30 min (corresponding to 6000 laser pulses); target-to-substrate distance of 4 cm; a vacuum in the chamber of 10^{-7} mbar; and the substrate was kept at room temperature during deposition. Prior to placement in the UHV chamber, the substrates were washed in baths of acetone and methanol and dried using N_2. Once in the chamber and under vacuum, the substrates were heated to 645 °C for 1 h to eliminate any contaminants present on the substrate surface. After the heating process, the substrates were allowed to cool down to room temperature before the deposition began. Before the start of deposition, to ensure a clean target surface, the target was ablated for

[d]Macroscopic pieces of the target that are ablated from the target surface and fall onto the substrate

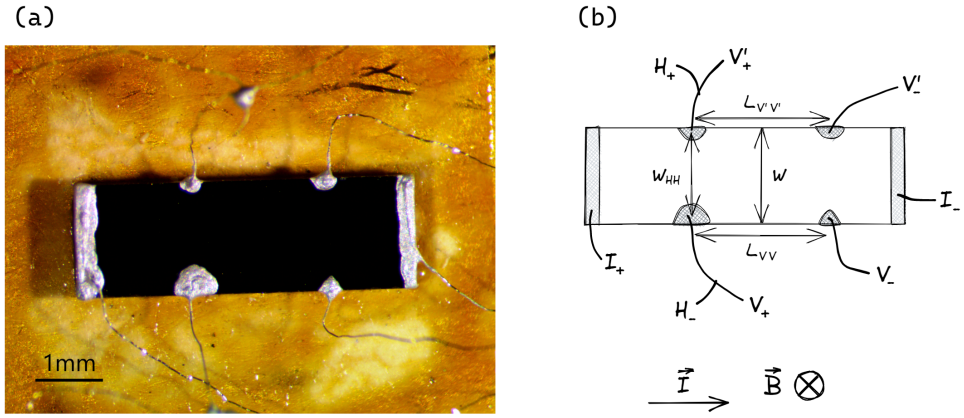

Figure 3.6: Image (a) and schematic representations of the sample and contact geometries (b) for resistivity, Hall effect and magnetoresistance measurements on a TiZrNbCuNi/$SrLaAlO_4$ thin film CA011b_1. I_+I_- are the current contacts, V_+V_- and $V'_+V'_-$ are two pairs of redundant voltage contacts and H_+H_- are Hall contacts. The directions of electric current and magnetic field are indicated in the bottom right.

10 min using the deposition parameters while keeping the substrate covered.

The SEM/EDS images of the CA011a sample reveal a clean surface and uniform distribution of elements, see Figure 3.5. However, the data for the Ti map is not reliable due to the overlap between the Ti Kα peak and La Kα peak from the substrate. Determining the atomic concentration of the deposited films was not possible, as a correction accounting for the sample's small thickness would be necessary. Unfortunately, no reliable methods for determining sample thickness were available at the time.

An estimate of the thickness can be made from Hall effect and resistivity measurements by using the Hall coefficient and room-temperature resistivity values for $Ni_{0.20}$ metallic glass ribbons. For CA011b_1, the estimated thickness from resistivity is (100 ± 10) nm, and from the Hall coefficient it is (200 ± 50) nm. Despite a slight difference, these values are in good agreement.

While we are currently unable to precisely pinpoint the origin of this discrepancy, it has been observed that amorphous thin films have higher resistivities than their bulk metallic glass counterparts [126–128]. Moreover, the resistivities were found to increase with decreasing thickness [129, 130]. A higher resistivity of the thin film sample would result in a larger calculated thickness value, thereby bringing it closer to the value obtained from the Hall coefficient. On the other hand, the Hall coefficients of thin films were found to be in good agreement with those of metallic glass ribbons [127, 128].

Resistivity, Hall effect, and magnetoresistance measurements were performed on the

TiZrNbCuNi/$SrLaAlO_4$ thin film CA011b_1 following the same procedures as for the metallic glass ribbon samples. The sample was thoroughly cleaned in an ultrasonic bath with acetone and isopropyl alcohol. It was then mounted on a gold-plated ceramic sample carrier using "GE" varnish. Platinum wires were glued onto the samples with silver paste to create current, voltage, and Hall contacts, as shown in Figure 3.6.

3.3 Transport measurements

Sample resistivities ρ were determined using the standard four-contact resistance measurements, in order to eliminate contact resistance. Contacts were arranged on the samples as shown in Figures 3.2 and 3.6. Due to significant uncertainty in ribbon sample thickness t, resistivity was calculated using sample mass m, sample length L_{sample}, voltage contact distance L_{VV}, and density D:[e]

$$\rho = \frac{w \times t}{L_{\text{VV}}} R = \frac{m}{L_{\text{sample}} \times L_{\text{VV}} \times D} R \,. \tag{3.1}$$

Magnetoresistance is defined as the relative change in sample resistance due to the applied magnetic field:

$$\frac{\Delta R}{R(0)} = \frac{R(\mu_0 H) - R(0)}{R(0)} \,, \tag{3.2}$$

where $R(\mu_0 H)$ and $R(0)$ represent resistance in the presence and absence of the magnetic field, respectively. Since MR is symmetric with respect to the direction of the applied magnetic field, any asymmetric contributions to the measured resistance, such as the Hall effect, can be eliminated by symmetrizing the resistance $R(\mu_0 H)$ with respect to the magnetic field direction:

$$R(\mu_0 H) = \frac{R(\mu_0 H) + R(-\mu_0 H)}{2} \,. \tag{3.3}$$

In Hall effect measurements, we measure the Hall voltage $V_H = E_H w_{\text{HH}}$ on a pair of contacts (H_+H_-) perpendicular to the applied magnetic field $\mu_0 H$ and current $I = jwt$, as indicated in Figures 3.2(d) and 3.6(b), where w_{HH} is the distance between the Hall contacts. In a magnetic field perpendicular to the current, the Hall effect generates an electric field E_H perpendicular to both the applied current and magnetic field, and is

[e]Density was estimated using the rule-of-mixtures, with $D = (\sum_i W_i/D_i)$, where W_i and D_i are the mass fraction and density of the i-th component, respectively [22, 124].

proportional to the magnitudes of the applied magnetic field $\mu_0 H$ and current density j:

$$E_H = R_H \, j \, \mu_0 H \ , \tag{3.4}$$

where the proportionality constant R_H is known as the Hall coefficient. It is common to combine the measured Hall voltage V_H and applied current I into a so-called Hall resistance:

$$R_{xy} = \frac{V_H}{I} = R_H \frac{w_{\mathrm{HH}}}{wt} \mu_0 H \ . \tag{3.5}$$

By measuring the magnetic field dependence of the Hall resistance R_{xy}, we can determine the slope $a = R_{xy}/\mu_0 H$, from which the Hall coefficient can be calculated as:

$$R_H = at \frac{w}{w_{\mathrm{HH}}} \ . \tag{3.6}$$

The thickness of the ribbon samples is determined from the sample mass, broad surface area $S_{L\times w}$, and density:

$$t = \frac{m}{S_{L\times w} \times D} \ . \tag{3.7}$$

Due to imperfect placement of the Hall contacts, it is possible to observe MR in measurements of the Hall resistance. Since the Hall effect is asymmetric with respect to magnetic field direction, we asymmetrize the Hall resistance to remove symmetric components:

$$R_{xy}(\mu_0 H) = \frac{R_{xy}(\mu_0 H) - R_{xy}(-\mu_0 H)}{2} \ . \tag{3.8}$$

Sample dimensions and contact distances were determined from calibrated images, captured by a CMOS camera attached to a microscope. Uncertainty due to the finite width of silver paste contacts and the error in determining the sample dimensions and mass was incorporated into the error values of absolute resistivity and Hall coefficient, as well as values derived from those.

Measurements were conducted using either DC or low-frequency (22Hz) AC current. In both cases, Keithley 6221 was used as the current source. For DC currents, voltages were measured with Keithley 2182a nanovoltmeters. Due to the presence of thermoelectric voltages, the measured voltages would not be symmetric with respect to the current direction, resulting in a voltage offset. To eliminate this contribution, voltages were measured for both directions of current and the respective resistances were averaged as follows:

$$R = \frac{R(+I) + R(-I)}{2} \ . \tag{3.9}$$

This method was applied for measurements of resistance and Hall voltage.

AC voltages were measured using dual-phase Signal Recovery 5210 and 7225 Lock-In amplifiers. A precision 1 Ω resistor in series with the sample and current source was employed to set up the reference phase on the Lock-In amplifiers. The advantages of AC measurements include lower noise and faster measurement times. Noise can be further reduced by connecting a low-noise model 1900 transformer, which amplifies the signal by a factor 100. The disadvantage of AC measurements involves parasitic capacitances at the sample-contact interface. These become significant for high resistance samples, i.e. high RC constant. All the measured samples were of low resistance <1 Ω, and parasitic capacitances were not an issue.

However, for some samples, an out-of-phase component (due to capacitance and/or inductance) appeared in the magnetic fields. This component increased roughly with $\mu_0 H^2$ and was dependent on the current frequency used, even displaying a change in sign with changing frequency. We attribute this to extrinsic sources, as it changed with new contacts applied to the same sample. Most likely, this effect is due to the uneven thickness profile and longitudinal microcracks in the ribbon samples, which are the result of the melt-spinning process, causing unpredictable current directions in the magnetic field. This is corroborated by the fact that this effect was not observed in the amorphous thin film CA011b_1. In most cases, the out-of-phase component was much larger than the in-phase (resistive) component of the voltage at high magnetic fields, which made precise measurements of the Hall effect and MR with an AC current impossible. In these cases, DC current was used for measurements within and without of the magnetic field, for consistency. While a similar effect, charging with an RC constant that increases with an increasing magnetic field, was also observed for DC currents in these samples. This could be mitigated by waiting 2-3 s after setting a current for the voltage to stabilize before taking a measurement.

Thus, resistance, Hall effect, and MR measurements, depending on the sample, were performed using either AC or DC currents with currents in the 200 µA-2 mA range.

For superconductive transition measurements, only AC current was employed, as the lower noise allowed for the application of smaller currents, and the applied magnetic fields <4 T were low enough for the out-of-phase component to be negligible. As a precaution, the measurements were verified with DC measurements, which showed good agreement within the noise. Currents in the 20-200 µA range were used, corresponding to current densities in the range of 0.1-0.8 A cm^{-2}.

3.4 Superconducting Magnet System

To perform measurements in a magnetic field and at low temperatures, a cryostat with a superconducting magnet is used. The 16/18 T Oxford superconducting magnet system employed in this work is illustrated in Figure 3.7(a).

High magnetic fields up to ±16 T are achieved by passing a high current 100 A through the superconductive coil. The magnet is immersed in a liquid He (LHe) bath to maintain its superconductivity. To minimize LHe evaporation, the LHe chamber is surrounded by a liquid nitrogen (LN_2) chamber. To reduce thermal contact between the two cryogenic liquid chambers and the exterior, an outer vacuum chamber is utilized.

Inside the system, either a variable temperature insert (VTI) or a HelioxVL He3 insert is placed, as illustrated in Figures 3.7(a) and 3.8. The VTI system is used for measurements from room temperature down to 1.3 K, although in the magnetic field, the highest temperature is limited to 200 K. The He3 insert is employed for low-temperature measurements down to 0.3 K. Although no high-temperature limit is explicitly set and temperatures up to room temperature can be achieved, for practical purposes, temperatures are kept <20 K. Measurements of resistivity, Hall effect, and MR were performed in the VTI, while low-temperature measurements of superconductive transitions were conducted in the He3 insert.

To perform measurements in the VTI system, the gold-plated sample carrier with a mounted sample is placed in a socket at the top of a sample holder, as detailed in Figure 3.7(b). The sample is then enclosed within a cylindrical copper cover cap to ensure good thermal equilibrium across the sample and with the calibrated Cernox temperature sensor mounted behind the sample carrier socket. The copper cap is wrapped with a Constantan wire, which serves as the sample heater. Once closed and tested, the sample holder is inserted into the sample space of the VTI system, as depicted in Figure 3.7(a). The sample is situated at the centre of the magnetic field. Inside the sample space, a rough vacuum is maintained by a rotary vane pump.

By opening a needle valve (NV), a small amount of LHe is transferred from the helium bath into the sample space. The expansion of LHe into a gas reduces its temperature below 4.2 K, so that sample temperatures down to 1.3 K can be achieved. The cooling power of the system is controlled by opening and closing the NV and with a heater placed near the opening of the NV into the sample space. Fine temperature control is achieved through the sample heater. A LakeShore 340 temperature controller reads the temperature from the Cernox sensor and controls the sample heater power to attain the desired temperature.

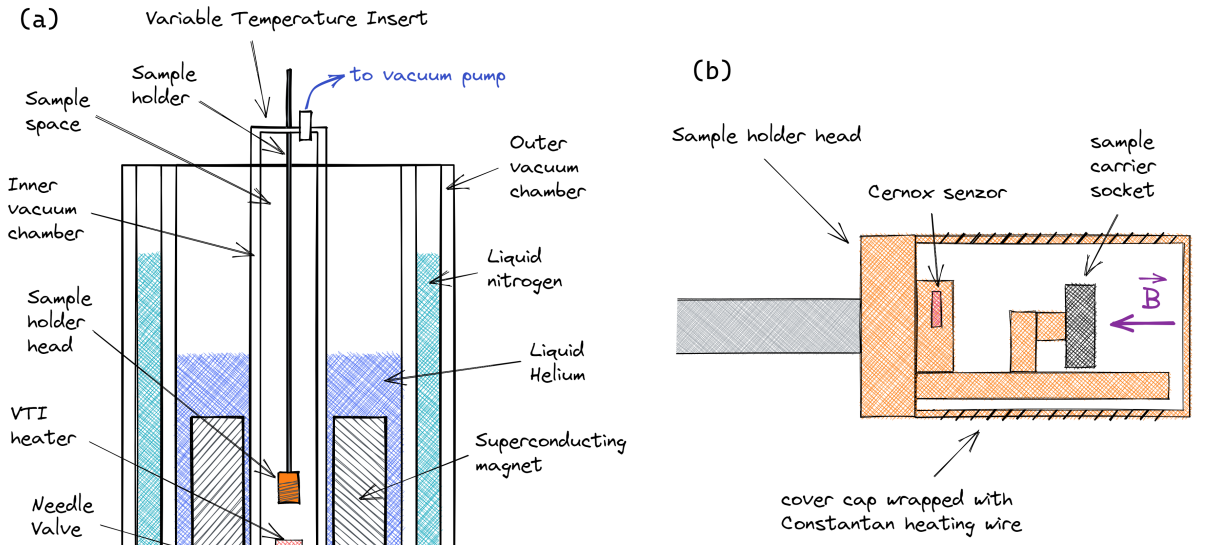

Figure 3.7: (**a**) Schematic diagram of the 16/18 T Oxford superconducting magnet system with a variable temperature insert and sample holder. (**b**) Schematic diagram of the sample holder head.

To perform measurements with the He3 system, the gold-plated sample carrier with a mounted sample is placed in a socket at the base of the He3 insert, as shown in Figure 3.8. Once the sample is in place, the inner vacuum chamber is sealed and evacuated, and a small amount of ^{4}He exchange gas is added to the inner vacuum chamber. The insert may than be slowly lowered into the superconducting magnet system, in place of the VTI shown in Figure 3.7(a). The small amount of exchange gas facilitates cooling; once the system reaches its base temperature, a piece of charcoal cloth will absorb the exchange gas, ensuring thermal insulation between the LHe bath and the sample.

The He3 insert possesses a self-contained storage reservoir of ^{3}He gas. When the system is cooled, the ^{3}He gas is absorbed by the sorption pump. Heating the sorption pump releases the ^{3}He gas, which condenses into the ^{3}He pot upon contact with the 1K plate. The 1K plate is cooled similarly to the VTI system: by opening the NV, liquid ^{4}He is drawn from the bath via a pickup tube into an expansion coil around the 1K plate. The expansion of the ^{4}He cools the 1K plate, and the gas is evacuated by a rotary vane pump.

Once all the ^{3}He gas has been released from the sorption pump and liquefied into the

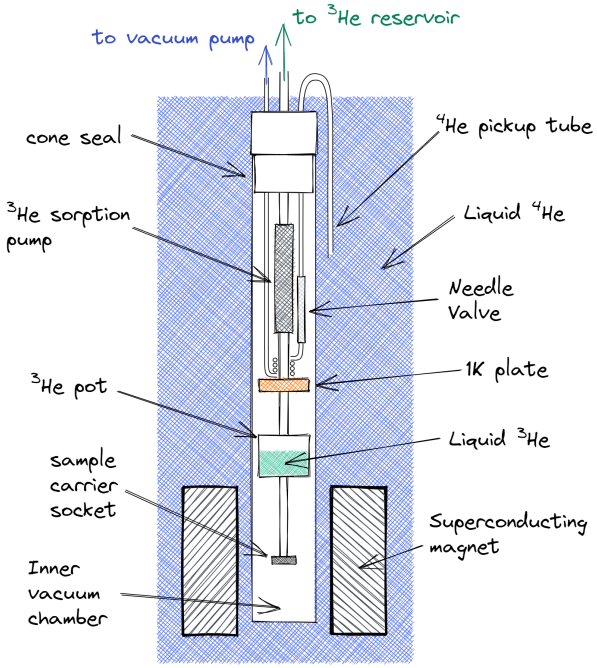

Figure 3.8: Schematic diagram of the HelioxVL He3 insert for the 16/18 T Oxford superconducting magnet system.

^{3}He pot, the pot and the sample, which is in good thermal contact with the pot, will be at approximately 1.3 K. The temperature can be lowered by cooling the sorption pump until it starts to absorb the ^{3}He gas, which results in pumping of the gas and consequently lowering the temperature of the ^{3}He liquid in the pot. In this way, the ^{3}He pot and the sample can be cooled down to 0.3 K.

The temperature is varied by heating or cooling the sorption pump, which alters the pumping of ^{3}He and therefore the cooling of the ^{3}He liquid. Additionally, heat can be supplied directly to the ^{3}He pot via a heater. In this manner, the temperature can be varied between 0.3-3 K. For higher temperatures, the liquid ^{3}He needs to be evaporated, and the temperature control is achieved by combining the cooling from the 1K pot and heating from the ^{3}He pot heater. Heat exchange between the two is facilitated through the ^{3}He gas.

The sample temperature is measured by a calibrated Cernox sensor placed directly behind the sample carrier socket. A LakeShore 340 temperature controller is used to read the temperature. Due to the extremely low temperatures, the Cernox sensor exhibits non-negligible magnetoresistance. Therefore, for measurements in a magnetic field, an appropriate temperature correction was applied.

Chapter 4

Results and discussion

This chapter presents the results, analysis, and discussion of comprehensive measurements of transport properties, which include resistivity, Hall effect, magnetoresistance, and superconductivity, on metallic glass ribbons from three alloy systems: Cu_x, Ni_x, and Co_x, and three alloy variants with a fixed TL (Cu, Ni) content: $Ti_{0.30}$, $Zr_{0.30}$, and $Nb_{0.30}$. Furthermore, measurements on the CA011b_1 thin film of TiZrNbCuNi deposited on a $SrLaAlO_4$ substrate, are presented as well.

In section 4.3 on resistivity, we outline a novel model involving two parallel conductance channels. This model was found to better describe the temperature variation of resistivity in our alloys. Additionally, we discuss the potential physical origins of this proposed model.

4.1 Superconductivity

All our samples, barring $Cu_{0.50}$ and $Co_{0.43}$, were superconducting at temperatures above 300 mK. The composition x dependence of the superconducting transition temperatures T_c, defined as the temperature at which the resistivity drops to half the normal resistivity just above the transitions $\rho(T_c) = 0.5\rho_N$, is illustrated in Figure 4.1(a).

The superconducting transition temperatures T_c are observed to be lower than those for Zr-based binary alloys of similar composition (such as those shown in Figure 1.15); this effect can be ascribed to the influence of Ti. As previously mentioned in the introduction 1.4.3, no superconducting transitions for $Ti_{1-x}Ni_x$ and $Ti_{1-x}Cu_x$ alloys were detected down to 1.4 K and 1.0 K respectively [102]. The adverse influence of Ti is also evident from the lower T_c for $Ti_{0.30}$ as compared to $Zr_{0.30}$ and $Nb_{0.30}$.

The monotonic decrease of T_c with increasing TL content, barring $Cu_{0.0}$, aligns with

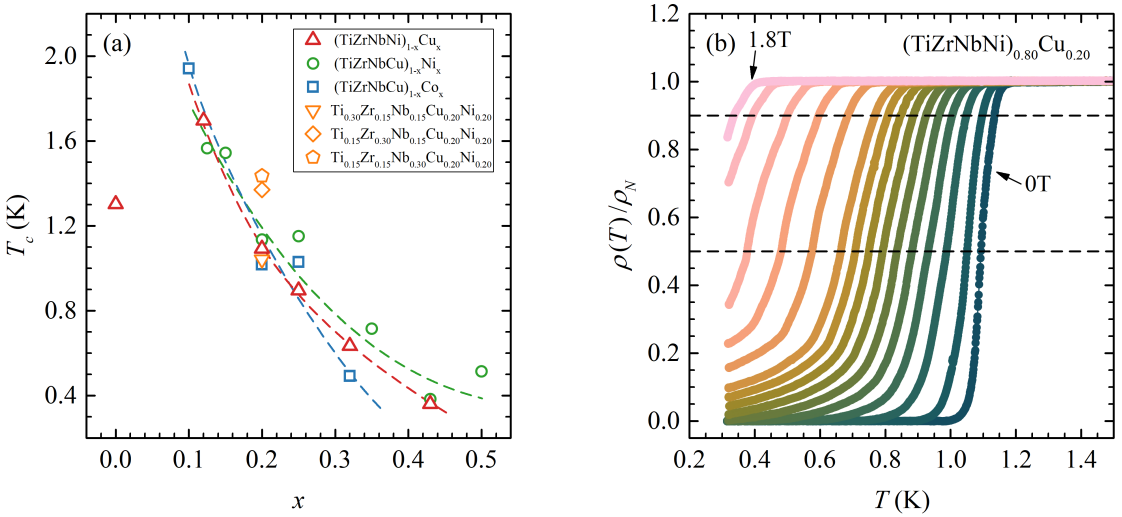

Figure 4.1: (**a**) Composition x dependence of the superconducting transition temperatures T_c for Cu_x (red up-triangles), Ni_x (green circles), Co_x (blue squares) alloy system. Additionally, three alloy variants with fixed (CuNi) content Ti_{30} (orange down-triangle), Zr_{30} (orange diamond) and Nb_{30} (orange pentagon) are shown. The dashed lines are provided as guides to the eye. (**b**) Temperature dependence of the normalized resistivity $\rho(T)/\rho_N$ close to the superconducting transition for a $Cu_{0.20}$ metallic glass ribbon sample, in constant magnetic fields from 0-1.8 T.

other amorphous [66, 100, 102, 103] and crystalline [131, 132] TE–TL alloys . The rate of decline increases in the sequence Ni_x, Cu_x, Co_x as observed in related binary amorphous alloys. The deviation for the $Cu_{0.0}$ sample could be due to its composition, as small amounts of a nanocrystalline phase in the amorphous matrix were noted [22].

The scattering of transition temperatures for different compositions, such as the similar T_c values for $Ni_{0.125}$ and $Ni_{0.15}$, or $Ni_{0.20}$ and $Ni_{0.25}$, can be attributed to structural inhomogeneities in the sample. These inhomogeneities arise during the fabrication process. They can be caused by factors such as varying cooling rates between the beginning and the end of the ribbon, which occur as the copper roller heats up during fabrication; or by differences in the ribbon thickness. Furthermore, T_c measurements based on resistance are particularly sensitive, as they record the onset of the first superconducting current path through the sample, while the bulk of the sample remains in the normal state [133].

Values of the width of the resistive transitions ΔT_c, defined as the temperature interval between $0.1\rho_N$ and $0.9\rho_N$, varied within 0.06-0.15 K for Cu_x, 0.05-0.12 K for Ni_x, 0.05-0.40 K for Co_x, and 0.04-0.12 K for alloy variants with fixed (CuNi) content.

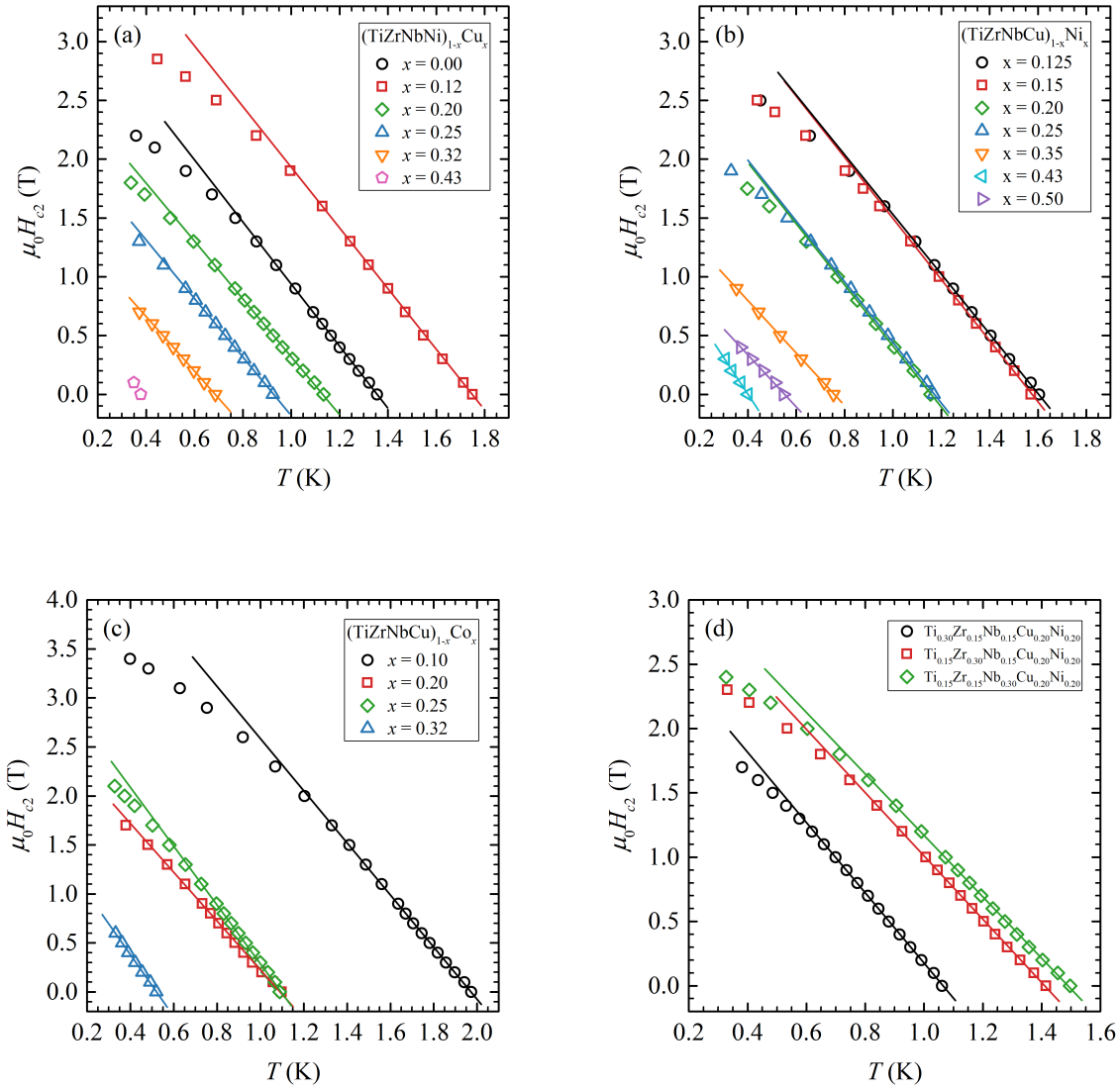

Figure 4.2: The temperature dependence of the upper critical fields $\mu_0 H_{c2}(T)$ for Cu_x (**a**), Ni_x (**b**), Co_x (**c**) alloy systems and three additional alloy variants with fixed (CuNi) content. The solid lines in these figures represent initial slopes of the upper critical field $(\mu_0 dH_{c2}/dT)_{T=T_c}$.

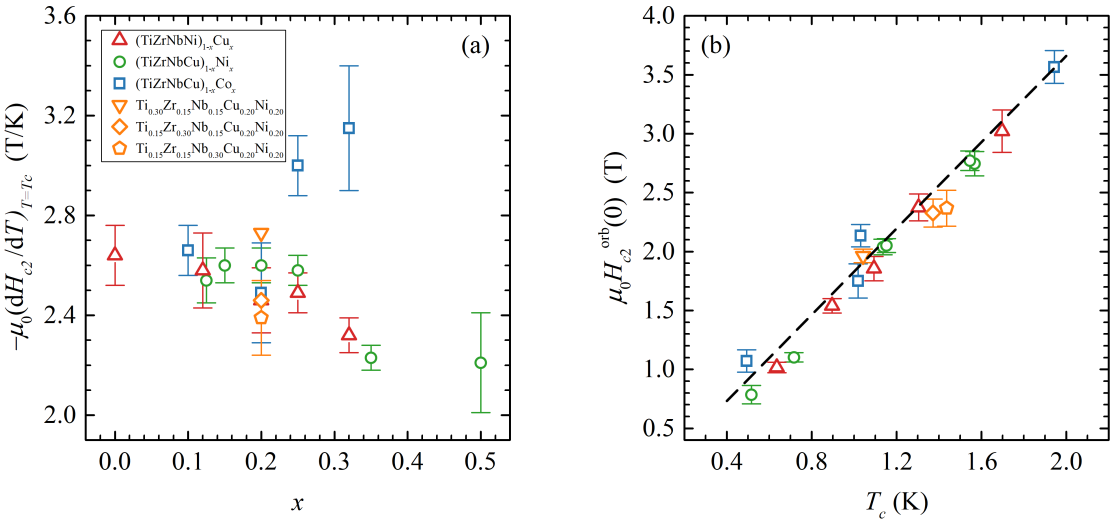

Figure 4.3: Composition x dependence of the upper critical fields at zero temperature $\mu_0 H_{c2}(0)$ (**a**) and the orbital-limiting field $H_{c2}^{\mathrm{orb}}(0)$ (**b**) for Cu_x (red up-triangles), Ni_x (green circles), Co_x (blue squares) alloy system, and three alloy variants with fixed (CuNi) content Ti_{30} (orange down-triangle), Zr_{30} (orange diamond) and Nb_{30} (orange pentagon). The dashed line in panel (b) corresponds to the BCS Pauli-limiting field $\mu_0 H_{\mathrm{P}}^{\mathrm{BCS}}(0) = 1.84 T_c$.

In Figure 4.1(b), we provide a representative example of the temperature dependence of the normalized resistivity $\rho(T)/\rho_N$ in proximity to the superconducting transition for a $\mathrm{Cu}_{0.20}$ sample, subjected to varied magnetic fields. As the magnetic field increases, the transition temperature T_c decreases, and the transition widens, more so at the lower temperature end. To circumvent the effects of this broadening when determining transition temperatures at different magnetic fields $T_c(\mu_0 H)$, we opted for a different resistivity criterion, $\rho(T_c(\mu_0 H)) = 0.9\rho_N$.

We then ascertain the temperature dependence of the upper critical fields $\mu_0 H_{c2}(T)$ from these measurements, as demonstrated in Figure 4.2. The measured temperature range of $\mu_0 H_{c2}(T)$ is too narrow to perform an adequate fit to the WHH formula (1.36). However, we can determine the orbital-limiting field $H_{c2}^{\mathrm{orb}}(0)$ according to Equation (1.38), from initial slopes of the upper critical field $(\mu_0 dH_{c2}/dT)_{T=T_c}$, depicted as solid lines in Figure 4.2. The values of $(\mu_0 dH_{c2}/dT)_{T=T_c}$ demonstrate minimal variation with composition x, with absolute values decreasing in Cu_x and Ni_x, while increasing in Co_x.

Figure 4.3(b) shows the dependence of the orbital-limiting field $H_{c2}^{\mathrm{orb}}(0)$ on the superconducting transition temperature T_c. As the values of $(\mu_0 dH_{c2}/dT)_{T=T_c}$ display negligible variation with composition, $H_{c2}^{\mathrm{orb}}(0)$ scales linearly with T_c in accordance with Equation (1.38).

Interestingly, this scaling seems to align with the scaling of the BCS Pauli-limiting field $\mu_0 H_{\mathrm{P}}^{\mathrm{BCS}}(0) = 1.84 T_c$. This suggests that the orbital and Pauli paramagnetic spin splitting mechanisms contribute nearly equally to the magnetic field breaking of Cooper pairs. From Equation (1.37), for $H_{c2}^{\mathrm{orb}}(0) \approx H_{\mathrm{P}}^{\mathrm{BCS}}(0)$, it follows that the Maki parameter for our amorphous alloys is $\alpha \approx \sqrt{2}$. This estimate aligns with the Maki parameter $\alpha = 1.2 - 1.9$ identified in related Zr–TL binary amorphous alloys [100, 106].

4.2 Hall effect

The Hall voltage (resistance) of all measured samples was linear with the magnetic field and temperature independent, within the noise, down to the lowest measured temperatures. Figure 4.4(a) shows a representative example for metallic glass ribbons, specifically a $Ni_{0.125}$ sample, while Figure 4.4(b) shows the measurement on the CA011b_1 thin film sample. While the voltage noise due to contact resistance was negligible compared to the full voltage across the sample in the case of resistance measurements, it constituted a significant component of the small Hall voltage signal. Uncertainty in the value of the slope due to this noise, coupled with the sample thickness t uncertainty, was incorporated into the error values of the Hall coefficient, as shown in Figure 4.4(c).

No temperature dependence of the Hall coefficient R_{H} was observed in any of the samples, despite the expected temperature dependence of R_{H} due to enhanced electron-electron interactions (EEI). This effect, which is proportional to the temperature dependence of the resistivity change due to EEI, as per Equation (1.6), should be less than 1 % (see subsection 4.3.3). The noise level in the present measurements precludes the detection of such minor variations in the Hall coefficient.

All values of the Hall coefficient R_{H} are positive, except for $Co_{0.43}$. The slope of Hall resistance in the CA011b_1 thin film sample was positive as well, as seen in Figure 4.4(b). However, the lack of an independently determined thickness of the sample precludes the determination of the Hall coefficient in the thin film sample. The dependence of the Hall coefficient on composition x in our quinary alloys, as seen in Figure 4.4(c), aligns well with that of binary TE–TL amorphous alloys.

R_{H} values for Cu_x alloys are generally constant within the measured range of Cu concentration. This is in line with binary $Zr_{1-x}Cu_x$, $Ti_{1-x}Cu_x$ and $Hf_{1-x}Cu_x$ amorphous alloys, where R_{H} values remain mostly constant up to 50 % of Cu content and exhibit a relatively high critical concentration around $x_c \approx 0.8$ [29, 44, 134].

R_{H} values for Ni_x alloys are practically constant for $x < 0.35$ and start to decrease

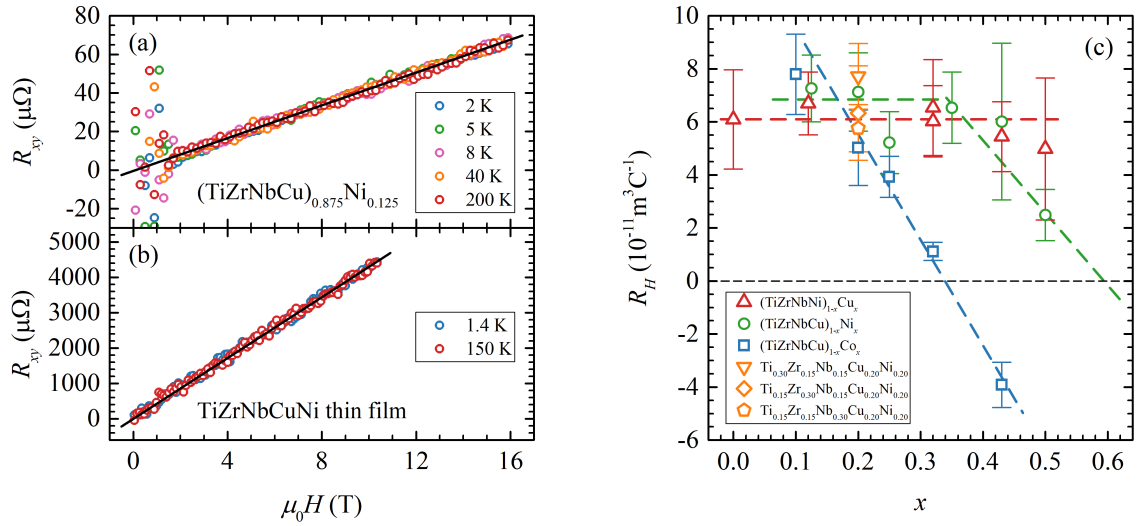

Figure 4.4: Magnetic field $\mu_0 H$ dependence of the Hall resistance R_{xy} for (**a**) a representative metallic glass ribbon $Ni_{0.125}$ and (**b**) the amorphous thin film sample CA011b_1. The solid black lines represent the slope fit. (**c**) Composition x dependence of the Hall coefficient R_H for Cu_x (red up-triangles), Ni_x (green circles), Co_x (blue squares) alloy systems. Additionally, three alloy variants with fixed (CuNi) content Ti_{30} (orange down-triangle), Zr_{30} (orange diamond) and Nb_{30} (orange pentagon) are shown. The dashed lines are provided as guides to the eye.

for higher concentrations. No crossover was observed within the available concentration range, but extrapolation from R_{H} values between $x = 0.35$ and $x = 0.50$ suggests a critical concentration of $x_c \approx 0.6$. This is higher than reported values in $Zr_{1-x}Ni_x$ of $x_c = 0.45$ [35]. This discrepancy could be due to the presence of Cu and Nb in our $(TiZrNbCu)_{1-x}Ni_x$ alloys. For instance, in $Ta_{1-x}Ni_x$.[a], the crossover concentration is around $x_c \approx 0.55$ [45]

Conversely, Co_x alloys exhibit a sharp drop in R_{H} values with an interpolated critical concentration at $x_c = 0.34$, which is in good agreement with binary $Zr_{1-x}Co_x$ with a critical concentration of $x_c = 0.32$ [35].

Regarding the alloys with fixed (CuNi) content, they exhibit a decrease in R_{H} values in the order $Ti_{30} \rightarrow Ni_{20} \rightarrow Zr_{30}$ and Nb_{30}. This trend is expected when increasing the concentration of 4d TE elements (Zr and Nb) at the expense of the 3d Ti.

[a]Ta and Nb belong to group 5, whereas Zr and Ti are group 4 elements.

4.3 Resistivity

All measured samples exhibited a high room-temperature resistivity in range of 140-240 µΩ cm, along with a small negative temperature coefficient of resistivity (TCR), consistent with the Mooij correlation [53], as is typically observed in amorphous TE-TL alloys [3, 29, 45, 46, 54, 66, 69–71, 104].

Figure 4.5 shows the composition x dependence of room-temperature resistivities ρ_{RT} for all measured metallic glass alloys. Room-temperature resistivities show some variation between different samples of nominally identical composition, with a typical discrepancy of around 5 %. In all three quinary alloy systems, the room-temperature resistivities ρ_{RT}, within a noticeable scatter, increase with composition x. This trend is consistent with findings in binary TE–TL alloys, where room-temperature resistivities initially increase with increasing proportion of TL content, and then begin to decrease at some concentration above 50 % TL content [3, 29, 45, 46, 54, 66]. The concentration at which this inversion occurs is relatively broad, with the specific point of change varying depending on the particular TE–TL system under consideration.

The room-temperature resistivities of Cu_x and Ni_x alloys exhibit a small increase with increasing TL content. Both the observed values and the small increase align with those found in related binary alloys, namely $\mathrm{Ti}_{1-x}\mathrm{Cu}_x$, $\mathrm{Zr}_{1-x}\mathrm{Cu}_x$, $\mathrm{Zr}_{1-x}\mathrm{Ni}_x$, and $\mathrm{Nb}_{1-x}\mathrm{Ni}_x$ [3, 29, 46, 54, 66, 73]. An exception is found in the binary $\mathrm{Ti}_{1-x}\mathrm{Ni}_x$ alloys, which display a significant increase from 149 µΩ cm at $x = 0.24$ to a peak value of 280 µΩ cm at $x = 0.40$, followed by a decrease to 184 µΩ cm at $x = 0.64$ [135]. A similarly high increase in resistivity with composition x is observed in our Co_x alloys. This behaviour differs from the related binary $\mathrm{Zr}_{1-x}\mathrm{Co}_x$ alloys, which have a smaller increase from 162 µΩ cm for $x = 0.20$, to 183.5 µΩ cm for $x = 0.45$ [3, 66, 73].

An interpretation for this type of resistivity dependence on composition has been proposed for amorphous TE-Cu alloys by D. Pavuna [46]. In the Cu-rich region, conduction primarily occurs via electron s-states. As the proportion of TE element increases, thereby enhancing the number of d-states at the Fermi level, resistivity increases due to a higher contribution from Mott s-d scattering. At the TE-rich end, conduction by d-state becomes increasingly more significant. In the intermediate region, the interplay of decreasing s-state conduction and increasing d-state conduction gives rise to a resistivity dependence that resembles the Nordheim rule, $\rho \propto x(1-x)$ [136]. However, extending this model to other TE elements (Fe, Co, Ni) is non-trivial, because unlike pure Cu, where the Fermi level is dominated by s-states, the Fermi levels of other pure TE elements contain both s- and d-states.

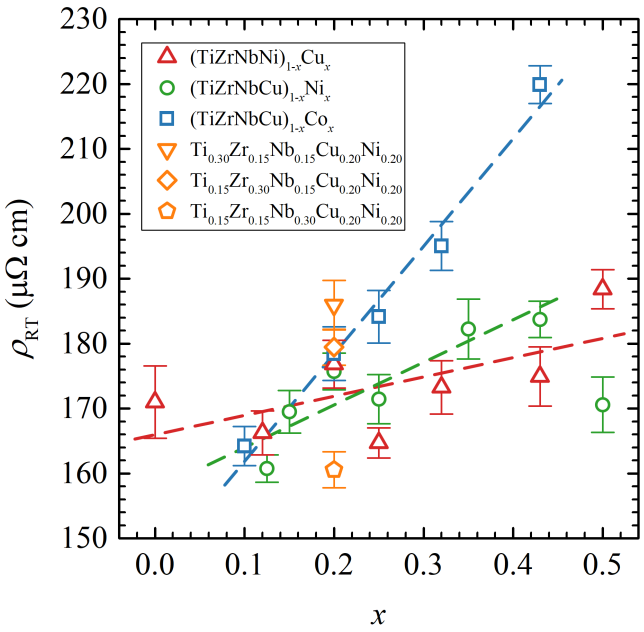

Figure 4.5: Composition x dependence of the room-temperature resistivity ρ_{RT} for Cu_x (red up-triangles), Ni_x (green circles), Co_x (blue squares) alloy system. Additionally, three alloy variants with fixed (CuNi) content Ti_{30} (orange down-triangle), Zr_{30} (orange diamond) and Nb_{30} (orange pentagon) are shown. The dashed lines are provided as guides to the eye.

The three studied alloy variants, with fixed (CuNi) content, show a small decline in ρ_{RT} in the $Ti_{0.30}$, $Zr_{0.30}$, $Nb_{0.30}$ sequence. This trend is consistent with the resistivity changes observed between different binary alloy systems, such as $Ti_{1-x}Ni_x$, $Ti_{1-x}Cu_x$, $Zr_{1-x}Ni_x$, $Zr_{1-x}Cu_x$, and $Nb_{1-x}Ni_x$ [3, 29, 46, 54].

4.3.1 Temperature dependence of resistivity

All measured samples exhibit a small negative TCR and the temperature variation of resistivity ρ_{RT} has the characteristic curve shape previously observed in binary and ternary TE–TL amorphous alloys, and as described in subsection 1.4.2.3. Examples of this curve shape can be found in Figures 4.7(a), 4.8(a) and 4.9(a). As the temperature is lowered, resistivity increases with a slightly increasing slope. Below approximately 30 K the resistivity curve begins to saturate with decreasing temperature, until it starts to increase again below approximately 15 K. Accordingly, as in other TE–TL alloys, the temperature variation of resistivity can be separated into a low-temperature and a high-temperature regime.

In the high-temperature regime the temperature dependence of resistivity has been attributed to the weak localization (WL) contribution. Accordingly, resistivity (conductivity) should scale with temperature as per Equation (1.25): $\propto \sqrt{T}$ above $\Theta_{\mathrm{D}}/3$ and $\propto T$ below $\Theta_{\mathrm{D}}/3$. As seen in Figure 4.6 for three representative curves, the conductivity ostensibly follows this temperature scaling, with a dividing temperature between the two regimes at approximately $\approx 100\,\mathrm{K}$. This is close to a third of the Debye temperatures $\Theta_{\mathrm{D}} = 220 - 260\,\mathrm{K}$ obtained for Ni_x alloys from LTSH measurements [37].

Examining the derivatives of conductivity with $\sqrt{T}$ and T in Figures 4.6(c) and 4.6(d) respectively, we observe wide peaks rather than a constant derivative over a wide temperature range, especially for the lower temperature $\sqrt{T}$ regime. This is understandable, as Equation (1.25) provides only limiting behaviour far from the Debye temperature Θ_D and furthermore does not consider the conductivity saturation due to spin-orbit coupling and magnetic impurity scattering at lower temperatures.

That begin said, we have found that the temperature variation of resistivity $\rho(T)$ can be better described by an alternative model involving two conductance channels:

$$\frac{1}{\rho(T)} = \frac{1}{\rho_{\mathrm{Metal}}(T)} + \frac{1}{\rho_{\mathrm{VRH}}(T)}\,. \tag{4.1}$$

where $\rho_{\mathrm{Metal}}(T)$ represents an ordinary metallic-like contribution and $\rho_{\mathrm{VRH}}(T)$ variable range hopping (VRH)-like contribution to the resistivity.

The metallic component $\rho_{\mathrm{Metal}}(T)$ consists of a nearly constant value ρ_0 at high temperatures, that we attribute to a large value of residual resistance in a disordered system, i.e. the Boltzmann contribution to resistivity. At low temperatures the resistivity in the metallic channel increases with decreasing temperature. This increase scales with $\sqrt{T}$ and can be attributed to quantum corrections to the Boltzmann conductivity. This metallic contribution to resistivity is therefore modelled as:

$$\rho_{\mathrm{Metal}}(T) = \begin{cases} a_{\mathrm{sqrt}}\left(\sqrt{T_{\mathrm{sqrt}}} - \sqrt{T}\right) + \rho_0 & \text{for } T \leq T_{\mathrm{sqrt}}\,, \\ \rho_0 & \text{for } T \geq T_{\mathrm{sqrt}}\,, \end{cases} \tag{4.2}$$

where T_{sqrt} represents the temperature at which the low-temperature component $\propto \sqrt{T}$ reaches a zero-value. In other words, it marks the transition between the low-temperature resistivity variation and the temperature-independent resistivity ρ_0 at higher temperatures.

As shall be shown latter, the low-temperature increase in resistivity can be equally

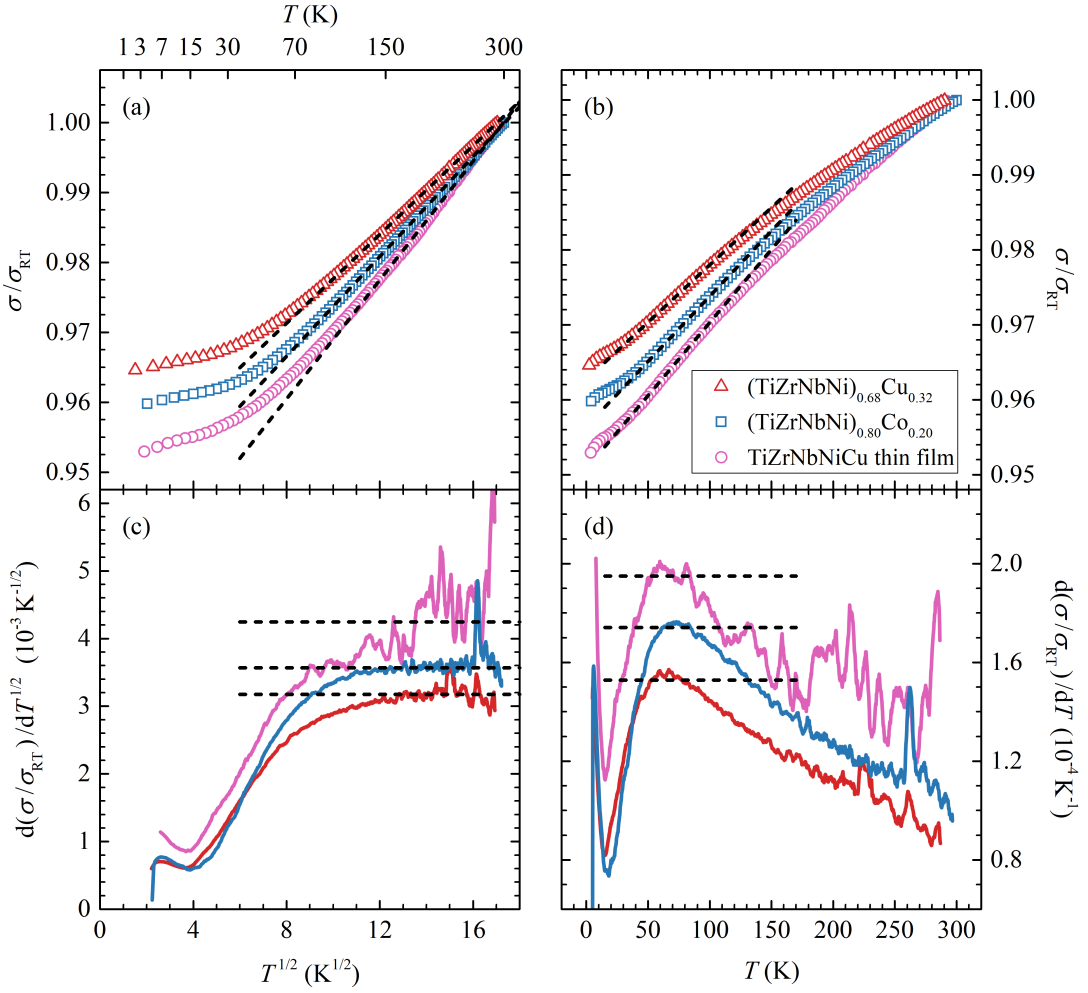

Figure 4.6: Normalized conductivity $\sigma/\sigma_{\mathrm{RT}}$ variation with $\sqrt{T}$ (**a**) and T (**b**) for representative metallic glass ribbon samples with compositions $Cu_{0.32}$ and $Co_{0.20}$, and the amorphous thin film sample CA011b_1. The dashed lines in these figures represent linear fits. (**c**) and (**d**) show derivatives of the normalized conductivity with $\sqrt{T}$ and T respectively. The dashed lines in these figures indicate the slope values of the linear fits in (a) and (b).

well described by a $\ln(T)$ scaling law, and the metallic contribution can alternatively be described by:

$$\rho_{\mathrm{Metal}}(T) = \begin{cases} a_{\ln} \ln\left(\frac{T_{\ln}}{T}\right) + \rho_0 & \text{for } T \leq T_{\ln} \,, \\ \rho_0 & \text{for } T \geq T_{\ln} \,, \end{cases} \tag{4.3}$$

where $T_{\ln}$ is analogous to T_{sqrt} in the previous Expression (4.2). We will return to discussing the merits of $\sqrt{T}$ and $\ln(T)$ scaling and other details of the low-temperature limit in subsection 4.3.3.

The VRH-like component can be described by the standard VRH temperature dependence:

$$\rho_{\mathrm{VRH}}(T) = \rho_{\mathrm{VRH},0} \, \exp\left(\frac{T_{\mathrm{VRH}}}{T}\right)^{p} , \tag{4.4}$$

with a $p = 1/2$ exponent. Contribution from $\rho_{\mathrm{VRH}}(T)$ to the total resistivity $\rho(T)$ is rather small, with its values 20-30 times larger than $\rho_{\mathrm{Metal}}(T)$ at room temperature and increasing for lower temperature. In other words, $\rho_{\mathrm{VRH}}(T)$ represents a small correction to the $\rho_{\mathrm{Metal}}(T)$ resistance.

It can be difficult to distinguish the correct value of the exponent p from $\ln(\rho) - T^{-p}$ plots. Therefore, to confirm the $p = 1/2$ used in the fitting procedure a so-called "special logarithmic derivative" can be used (see for example [137, 138]), where one calculates:

$$W = -\frac{d(\ln \rho_{\mathrm{VRH}})}{d(\ln T)} = p \left(\frac{T_{\mathrm{VRH}}}{T}\right)^{p} , \tag{4.5}$$

and then slope of the $\ln(W) - \ln(T)$ plot gives the value of the exponent p.

Three representative examples of fitting to the described model of two parallel conductance channels are shown in Figures 4.7, 4.8, and 4.9 for a $Cu_{0.32}$, a $Co_{0.20}$ and the thin film sample, respectively. (a) panels show the measured resistivity and the fitted curve according to Equation (4.1). Panels (b) and (c) display separated components $\rho_{\mathrm{Metal}}(T)$ and $\rho_{\mathrm{VRH}}(T)$ of the measured and fitted curves. To obtain the metal component of the measured resistivity, the VRH component of the fitting curve given with Equation (4.4) was subtracted from the total resistivity $\rho_{\mathrm{Metal}}(T) = \rho(T) - \rho^{\mathrm{fit}}_{\mathrm{VRH}}(T)$. Analogously, we obtain the VRH component of the measured resistivity by subtracting the metal component of the fitting curve given with Equation (4.2) (or (4.3)) $\rho_{\mathrm{VRH}}(T) = \rho(T) - \rho^{\mathrm{fit}}_{\mathrm{Metal}}(T)$.

The fitting procedure was performed iteratively. To start, initial values of the fitting parameters for $\rho_{\mathrm{Metal}}(T)$ are obtained from the measured resistivity curve $\rho(T)$— a_{sqrt} and T_{sqrt} (or $a_{\ln}$ and $T_{\ln}$) from the slope of the low-temperature increase and ρ_0 from the position of the saturation around 20 K. These values are used to calculate the values

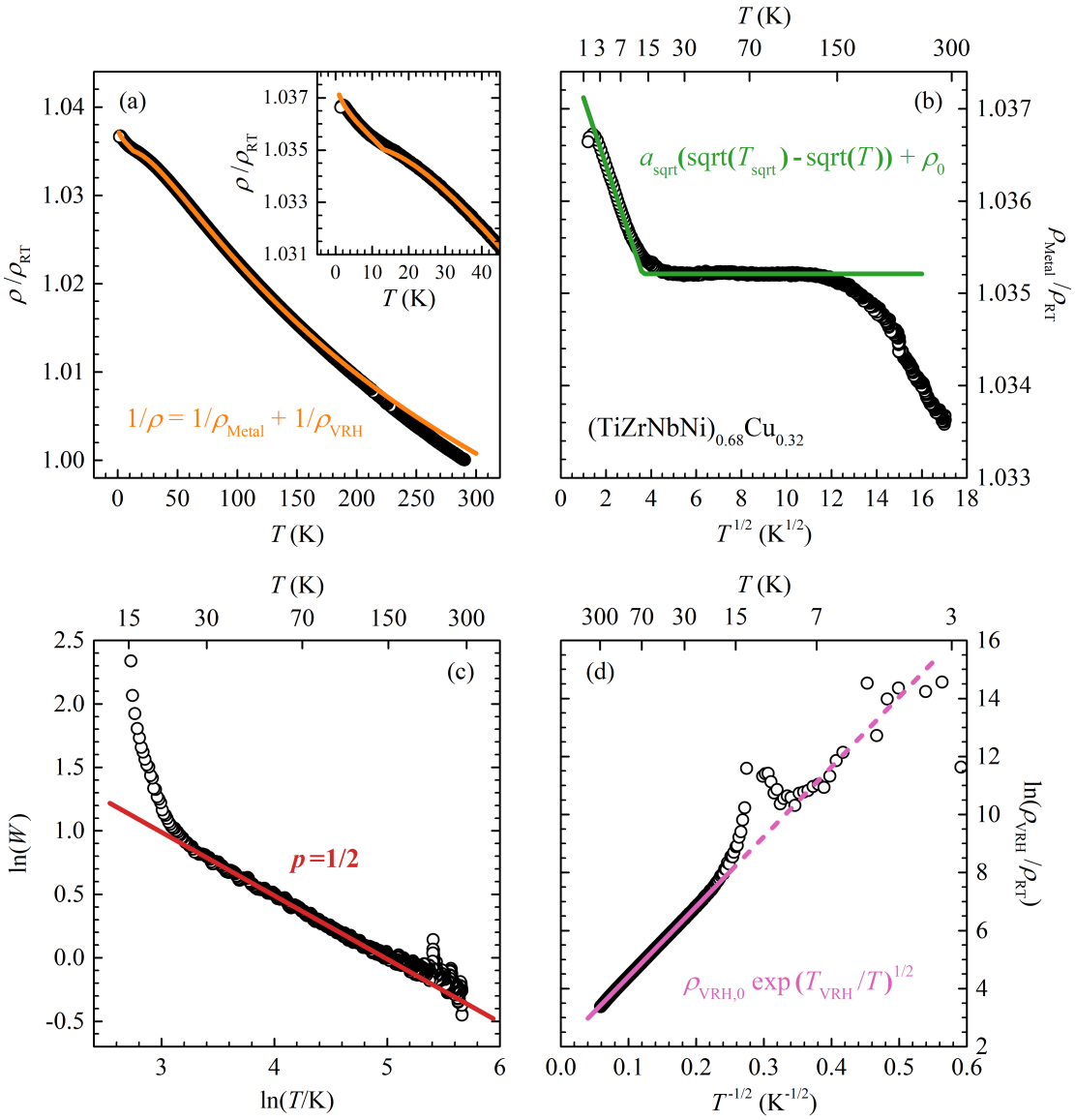

Figure 4.7: Results of fitting the measured temperature dependence of resistivity for a metallic glass ribbon sample with a $Cu_{0.32}$ composition, to the model with two parallel conductance channels. Points represent measured data, whereas lines indicate the fits. Refer to the text for details. (**a**) Temperature dependence of the normalized resistivity ρ/ρ_{RT}. Inset: magnified view of the low-temperature region of the main panel. (**b**) Temperature dependence of the metallic component of resistivity ρ_{Metal}/ρ_{RT}. (**c**) The "special logarithmic derivative" plot of the VRH-like component of resistivity, per Equation (4.5), featuring a $p = 1/2$ slope. (**d**) Logarithmic plot of the VRH-like component of resistivity $\ln(\rho_{VRH}/\rho_{RT})$ as a function of $1/\sqrt{T}$.

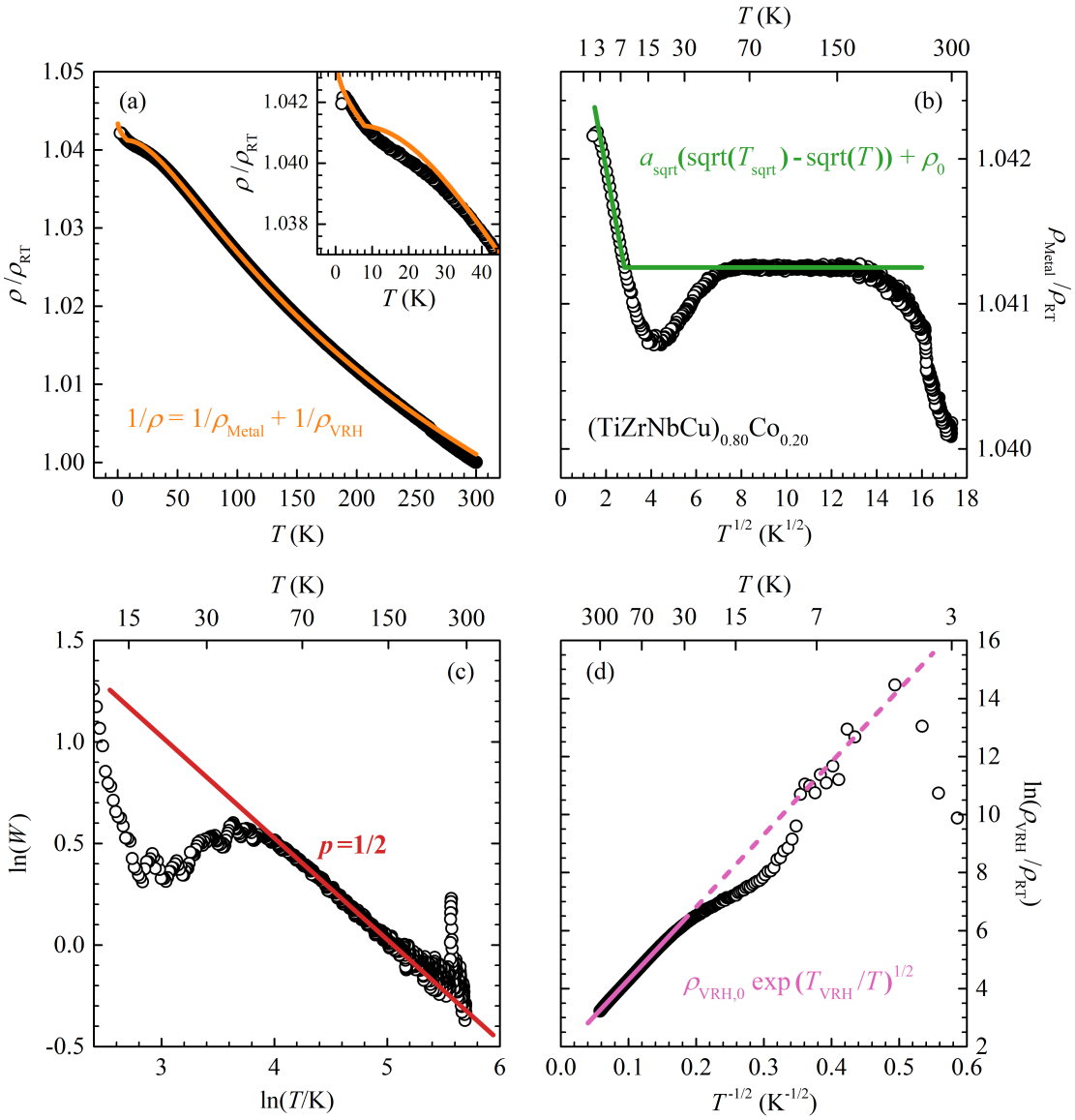

Figure 4.8: Results of fitting the measured temperature dependence of resistivity for a metallic glass ribbon sample with a $Co_{0.20}$ composition, to the model with two parallel conductance channels. Points represent measured data, whereas lines indicate the fits. Refer to the text for details. (**a**) Temperature dependence of the normalized resistivity ρ/ρ_{RT}. Inset: magnified view of the low-temperature region of the main panel. (**b**) Temperature dependence of the metallic component of resistivity ρ_{Metal}/ρ_{RT}. (**c**) The "special logarithmic derivative" plot of the VRH-like component of resistivity, per Equation (4.5), featuring a $p = 1/2$ slope. (**d**) Logarithmic plot of the VRH-like component of resistivity $\ln(\rho_{VRH}/\rho_{RT})$ as a function of $1/\sqrt{T}$.

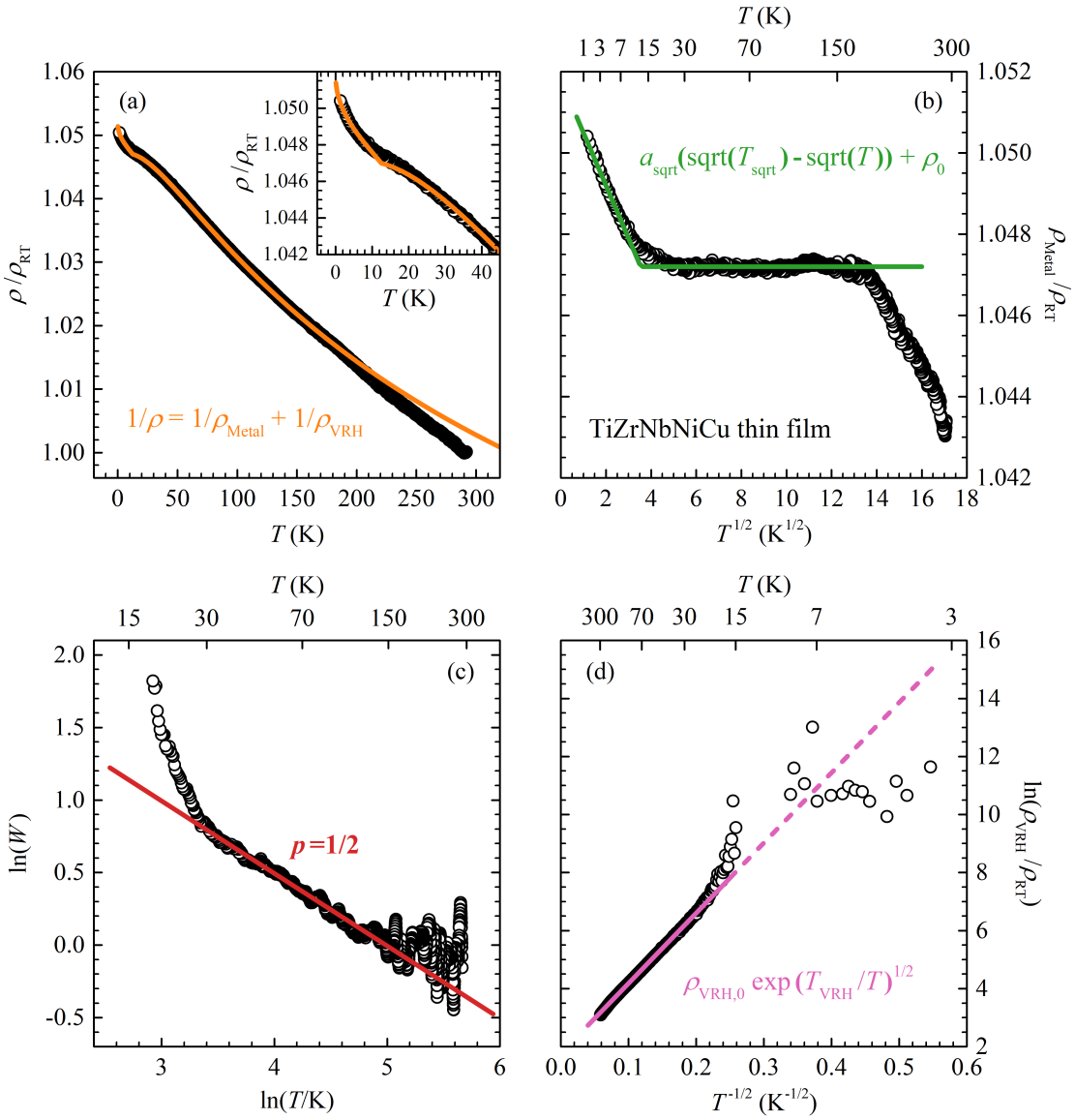

Figure 4.9: Results of fitting the measured temperature dependence of resistivity for the amorphous thin film CA011b_1, to the model with two parallel conductance channels. Points represent measured data, whereas lines indicate the fits. Refer to the text for details. (**a**) Temperature dependence of the normalized resistivity ρ/ρ_{RT}. Inset: magnified view of the low-temperature region of the main panel. (**b**) Temperature dependence of the metallic component of resistivity $\rho_{\mathrm{Metal}}/\rho_{\mathrm{RT}}$. (**c**) The "special logarithmic derivative" plot of the VRH-like component of resistivity, per Equation (4.5), featuring a $p = 1/2$ slope. (**d**) Logarithmic plot of the VRH-like component of resistivity $\ln(\rho_{\mathrm{VRH}}/\rho_{\mathrm{RT}})$ as a function of $1/\sqrt{T}$.

of the $\rho_{\mathrm{VRH}}(T)$ component, on which we fit Equation (4.4) to obtain parameters T_{VRH} and $\rho_{\mathrm{VRH}}(T)$. These are then used to calculate the $\rho_{\mathrm{Metal}}(T)$ component, on which we fit Equation (4.2) (or (4.3)) to obtain new values of the fitting parameters. We repeat this procedure until a satisfactory fit is reached for $\rho(T)$, calculated $\rho_{\mathrm{Metal}}(T)$ and $\rho_{\mathrm{VRH}}(T)$.

The described fitting procedure was satisfactorily applied to all our alloys, and the resulting fitting parameters are shown in Figures 4.13 and 4.15. These, along with the accompanying discussion, can be found in subsections 4.3.2 and 4.3.3, respectively. Errors of the fitting parameters are estimated based on the limits in which the values of the fitting parameters reasonably well describe the measured resistivity. The fitting was performed for normalized values of resistivity, such that values $a_{\mathrm{sqrt}}/\rho_{\mathrm{RT}}$, $a_{\mathrm{ln}}/\rho_{\mathrm{RT}}$ and $\rho_{\mathrm{VRH},0}/\rho_{\mathrm{RT}}$ are obtained from the fitting procedure. This was done in order to subsequently introduce the error in resistivity values stemming from errors in measuring the sample dimensions and mass, when calculating a_{sqrt}, a_{ln} and $\rho_{\mathrm{VRH},0}$.

From the calculated values of $\rho_{\mathrm{Metal}}(T)$ presented in Figures 4.7(b), 4.8(b) and 4.9(b), we clearly observe a low-temperature increase in resistivity, and a temperature independent contribution to resistivity from around 20 K to around 200 K, except for Co_x samples which exhibit a deviation from the proposed model at lower temperatures. Accordingly, in Co_x alloys, the lower limit of the temperature independent $\rho_{\mathrm{Metal}}(T)$ shifts to higher temperatures, with the limiting temperature increasing with Co content from 40 K for $\mathrm{Co}_{0.10}$ up to 70 K for $\mathrm{Co}_{0.43}$.

The temperature-independent behaviour of $\rho_{\mathrm{Metal}}(T)$ appears to break in all samples between 150 K and 200 K. Usually, the values of $\rho_{\mathrm{Metal}}(T)$ deviate below ρ_0, although in a few cases, it deviates to higher values. These deviations are of the order of 0.1 % of ρ_{RT}, whereas the contribution to the total resistivity from the VRH-like channel is only 3-5 %. That is to say, a small error in the measured data could have a significant effect on the fitting results. Measurements in this high-temperature range are difficult to perform with the current setup, and extrinsic effects on the resistivity, such as contact deterioration and thermal expansion of the sample, could play a significant role in the observed deviation. For example, the linear coefficient of thermal expansion of a related $\mathrm{Cu}_{0.55}\mathrm{Zr}_{0.30}\mathrm{Ti}_{0.10}\mathrm{Ni}_{0.05}$ metallic glass ribbon just above room temperature was found to be $\alpha_L = 1.3 \times 10^{-5}\,\mathrm{K}^{-1}$ [139]; similar values were found in other metallic glasses [140]. This corresponds to a length, and thereby a resistivity change, of about 0.13 % over a 100 K temperature range, comparable to the observed high-temperature deviation.

Due to the lack of more accurate data in this high-temperature regime at the moment, we believe that it is most likely that the temperature-independent $\rho_{\mathrm{Metal}}(T)$ extends above

200 K. To clarify this issue, additional measurements should be carried out from 200 K to temperatures well above room temperature.

In Figures 4.7(d), 4.8(d), and 4.9(d), we observe a good fit of the VRH Equation (4.4) to the calculated values of $\rho_{\mathrm{VRH}}(T)$ from 20 K to about 150-200 K depending on the sample. This is the same temperature range in which the temperature-independent $\rho_{\mathrm{Metal}}(T)$ is observed. Same as in $\rho_{\mathrm{Metal}}(T)$ a small deviation develops above approximately 200 K. A larger deviation is observed around 15 K and is an artefact of the fitting procedure, specifically, due to the sharp transition into the low-temperature resistivity upswing in the $\rho_{\mathrm{Metal}}(T)$ fitting curves (4.2) and (4.3), compared to a gradual transition in the measured curves. In case of Co_x samples a much larger deviation in $\rho_{\mathrm{VRH}}(T)$ appears due to the additional feature observed between 10 K and 70 K.

Figures 4.7(c), 4.8(c) and 4.9(c) of the "special logarithmic derivative" clearly show a $p = 1/2$ exponent. This exponent was confirmed in all measured samples in the temperature region where $\rho_{\mathrm{Metal}}(T)$ is constant, i.e. temperature independent. We emphasize here that the fitting procedure detailed above is unique in the sense that only one choice of $\rho_{\mathrm{Metal}}(T)$ values generates a $\rho_{\mathrm{VRH}}(T)$ with a VRH temperature variation, and only so with the exponent $p = 1/2$.

As seen in Figure 4.8(b), Co_x samples display a reproducible decrease in resistivity values below ρ_0, a feature unaccounted for in our proposed model and absent in all other measured alloy composition. This decrease for different Co_x alloys, which manifests between approximately 10 K and 70 K, can be seen in Figure 4.10. With an increase in Co content, both the magnitude and the width of this feature grow, while the temperature T_{min}, which marks the point of minimum resistivity in $\rho_{\mathrm{Metal}}(T)$, shifts towards lower values, as seen in Figure 4.15.

A similar minimum in resistivity, i.e. an additional increase with temperature in the low-temperature regime, has been reported in binary Zr–Fe [141, 142] as well as ternary Zr–Ni–Fe and Zr–Ni–Mn amorphous alloys [80, 143]. The effect increases as the composition approaches the paramagnetic-to-ferromagnetic transition with increasing Fe or Mn content, and it has been attributed to scattering of conduction electrons from spin fluctuations in nearly (ferro- and antiferro-) magnetic metals [141, 143].

It is plausible that this effect extends to Co-containing amorphous TE–TL alloys, but due to its small magnitude, it may not be discernible in the temperature variation of the raw resistivity measurements ρ_{RT}. Nonetheless, when the VRH-like component is removed from the total resistivity, the small change is visible next to other features of the calculated $\rho_{\mathrm{Metal}}(T)$ channel.

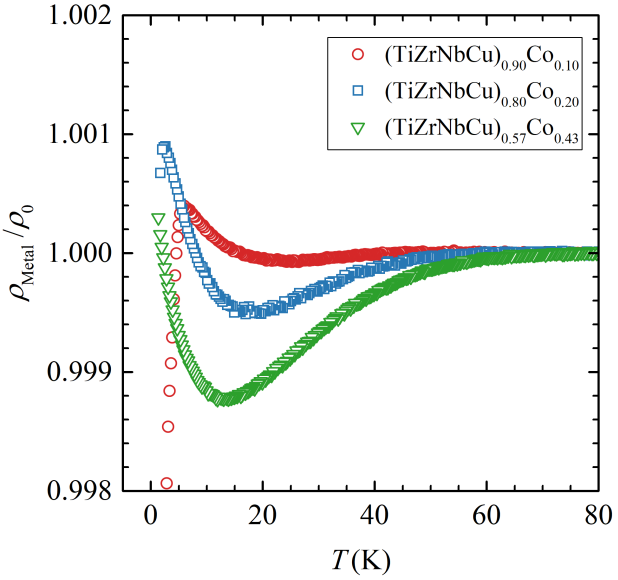

Figure 4.10: Temperature dependence of the normalized metallic component of resistivity $\rho_{\mathrm{Metal}}/\rho_0$ for three different Co_x alloys.

The resistivity contribution from spin fluctuations exhibits an increase with temperature, which scales as T^2 at low temperatures, transitions to a linear scaling T at medium temperatures, and eventually saturates to a temperature-independent contribution at higher temperatures [143]. It is challenging to validate this scaling behaviour in our data because of the overlapping effect from the low-temperature resistivity increase associated with quantum corrections.

Magnetic susceptibility measurements on Co_x alloys [21, 30] demonstrated an increase in susceptibility with increasing Co content for $x \geq 0.25$. This was associated with the approach towards a ferromagnetic transition at higher concentrations of Co. Moreover, partially crystalline $\mathrm{Co}_{0.50}$ alloys, which have not been investigated in this work, displayed ferromagnetic hysteresis loops at low temperatures [21].

The proposed model of two conductance channels bears resemblance to the empirical function (1.26) proposed by U. Mizutani and colleagues [76–80], to describe the temperature dependence of resistivity in the 30-300 K range. However, they differ in the finer details, such as using a sum of conductances (4.1) instead of resistivities (1.26). This difference enables our model to account for the resistivity saturation that happens at temperatures below 30 K. As the temperature is lowered, the $\rho_{\mathrm{VRH}}(T)$ component grows exponentially, leading to a substantial decline in its contribution to the total resistivity

$\rho(T)$. If not for the metal component's upswing at low temperatures, the total resistivity would tend towards ρ_0 as temperature is lowered.

4.3.2 VRH

We turn to exploring possible origins of the VRH-like temperature dependence. In the simplest picture a portion of the sample is insulating, i.e. electron states in parts of the sample are localised due to random variation of chemical and structural disorder throughout the sample. The metallic component of the sample contributes the temperature independent conductivity and the insulating component the VRH-like temperature dependent conductivity.

At room temperature the measured resistivities of the metal component are in the range of 140-240 µΩ cm, and those of the VRH-like component are in the range of 3000-8000 µΩ cm, as seen in Figure 4.13(a). These values represent the upper bounds of the true resistivities for the underlying metallic and insulating subregions.[b] In essence, these resistivities would be observed if the entire sample consisted exclusively of either the metallic or insulating region. The values appear appropriate for a disordered bad metal and a heavily doped semiconductor (e.g. the resistivity value is akin to that of silicon with $10^{19}\,\mathrm{cm}^{-3}$ impurities). However, a concern arises as a heavily doped semiconductor, i.e. high concentration of charge carries, is fundamentally opposed to localization and VRH conductivity [113].

A constraint must be imposed on the volume concentration of the insulating regions, as the predominantly metallic nature of the conductivity suggests that the insulating component appears as an inclusion within a metallic matrix. Moreover, SEM measurements did not reveal any inhomogeneity in the samples down to a scale of approximately 1 µm. Consequently, the dimensions of the features of the metallic and insulating regions would need to be smaller than roughly 3000 atoms.

[b] Assuming that the subregions contribute to the total resistance as two separate parallel resistors $1/R = 1/R_{\mathrm{Metal}} + 1/R_{\mathrm{insulator}}$, and their dimensions add up to the dimension of the entire sample. The measured resistivities of the insulating region are derived from the dimensions of the entire sample $\rho^{\mathrm{measured}}_{\mathrm{insulator}} = R_{\mathrm{insulator}} \times w_{\mathrm{sample}} \times t_{\mathrm{sample}}/L_{\mathrm{sample}}$, while the true resistivity of the insulating component should be determined from the dimensions of the subregion $\rho^{\mathrm{true}}_{\mathrm{insulator}} = R_{\mathrm{insulator}} \times w_{\mathrm{insulator}} \times t_{\mathrm{insulator}}/L_{\mathrm{insulator}}$. Assuming that the dimensions of the subregions scale with the volume concentration of the insulator $0 < x < 1$, $(w,t,L)_{\mathrm{insulator}} = x \times (w,t,L)_{\mathrm{sample}}$, it follows that $\rho^{\mathrm{true}}_{\mathrm{insulator}} = x \times \rho^{\mathrm{measured}}_{\mathrm{insulator}}$. Similarly, for the metallic subregion, $\rho^{\mathrm{true}}_{\mathrm{metal}} = (1-x) \times \rho^{\mathrm{measured}}_{\mathrm{metal}}$. Therefore, the true resistivities are invariably smaller then the measured values as defined above. This conclusion is valid if one or two of the sample dimensions are equal for the subregions and the sample, except when the width and thickness are maintained equal, and the length scales with concentration. However, this would correspond to a series connection between the subregions, which is in contradiction to the initial assumption that they are connected in parallel.

A further issue with this interpretation is the exponent $p = 1/2$, which is observed for all samples. This value excludes 3D Mott VRH with $p = 1/4$, which would be expected for an isotropic bulk material, although this assumption is debatable due to size limitations placed on the insulating features. This leaves the Efros-Shklovskii (ES) VRH with $p = 1/2$ as a possibility, but it has its own challenges. While it is possible to calculate the localisation length from the characteristic temperature, which for ES VRH is given as [113]:

$$T_{\mathrm{ES}} = \frac{2.8e^2}{\kappa\xi}\,. \tag{4.6}$$

Regrettably, we lack information on the value of relative permittivity κ, and furthermore, relative permittivity is expected to diverge when approaching the metal-insulator transition [144]. However, from the available information, we can calculate the ratio of the mean hopping length and localisation length [144]:

$$\bar{R}_{\mathrm{hop}}(T)/\xi = \frac{1}{4}\left(\frac{T_{\mathrm{ES}}}{T}\right)^{\frac{1}{2}}\,. \tag{4.7}$$

For VRH, the mean hopping length is expected to be larger than the localization length, which places an upper limit on the temperature at which ES VRH should be observed:

$$T < \frac{T_{\mathrm{ES}}}{16}\,. \tag{4.8}$$

The values of the mean hopping length can be smaller than the localisation length close to metal-insulator transition (MIT), but then an even stricter limit can be placed in the case of weakly compensated semiconductors [144]:

$$T < \frac{T_{\mathrm{ES}}}{25}\,. \tag{4.9}$$

The values of T_{VRH} in our samples vary in the 500-800 K range, while the $p = 1/2$ exponent was clearly observed in the 30-150 K, meaning neither condition is satisfied in our samples. According to criteria (4.8), the highest temperature VRH should be observed is $800\,\mathrm{K}/16 = 50\,\mathrm{K}$.

We therefore look for an alternative theory which could explain both the low resistivity of the insulating component and the high temperatures of the observed VRH-like conductivity with a $p = 1/2$ exponent. We start with the assumption that the system, due to inherent chemical and structural disorder, contains localised states, i.e. there exists a mobility edge separating localized and delocalised sites. This appears as a reasonable as-

sumption due to the high resistivity for a metal and the presumed appearance of VRH-like conduction.

Sites, i.e. localized atomic orbitals, in the system can either be resonant (close in energy and space) and form collective extended delocalized states, or non resonant forming localized states (see section 2.1 for details). Orbitals that form localised states do not contribute significantly to wavefunctions of delocalised states and vice versa. Thus, throughout the system there will exist randomly distributed regions composed of localised or delocalised states, as illustrated in the Figure 4.11. To clarify, it is not that the localised states are found at the Fermi level, but that the existence of localized states at these sites means they will not contribute significantly to delocalized states and therefore there will be regions of space were delocalized state wavefunctions fall of exponentially. We will refer to them as regions of delocalised states and regions of localised states, or localised and delocalized regions for short.

Owing to the predominantly metallic nature, it is reasonable to assume that regions of delocalised states form an infinite cluster. Alongside the infinite cluster, finite clusters of mutually resonant sites can also form, which are separated from the infinite cluster by regions of localised states. These finite clusters will not contribute to charge transport and neither will branches of the infinite cluster that form dead ends (blind alleys), as indicated in Figure 4.11. From now on, we will refer to the portion of the infinite cluster that contributes to charge transport solely through the diffusive motion of electrons as the *principal component of the infinite cluster*. The remaining portions of the infinite cluster will be referred to as *dead ends*, and the finite clusters as *isolated pockets*.

Only the portion of the sample that contains the principal component of the infinite cluster contributes to the classical metallic conductivity. This is a sub-portion of the portion of the sample forming the infinite cluster, therefore the part of the sample contributing $\rho_{\mathrm{Metal}}(T)$ can be smaller then the critical concentration of sites forming delocalized states that is needed to from an infinite cluster, i.e. for the system to be on the metallic side of the MIT.

We propose that in such a system, hopping between two dead ends, or an isolated pocket and the infinite cluster, at places where they are separated by short distance can significantly contribute to charge transport. These dead ends and/or isolated pockets can form conduction channels that run parallel to the principal component of the infinite cluster, for example, see the illustrations in Figures 4.12(a) and (b). With a small number of hops, channels can be formed that connect distant parts of the principal component of the infinite cluster, acting as a sort of bypass.

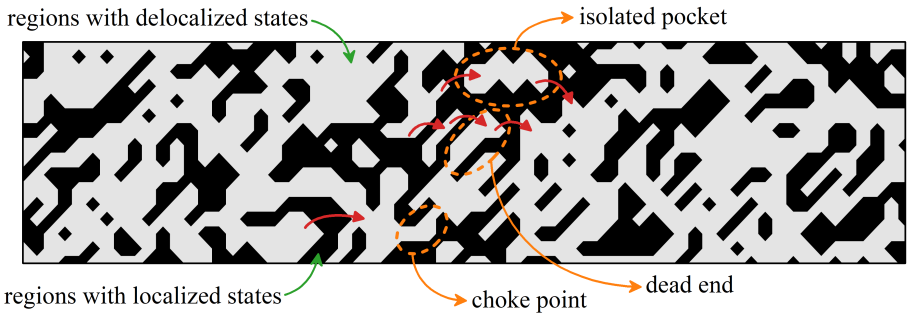

Figure 4.11: Illustration of a two dimensional sample with randomly distributed regions of localised sites and delocalised states. Grey area: regions of delocalized states. Black area: regions of localized sites. Red arrows: hopping between isolated pockets and/or dead ends. Orange ellipsis identify examples of key features: isolated pocket, dead end, and choke point.

The most significant contribution would come from channels, which are combinations of dead ends and isolated pockets, that connect sections of the principal component of the infinite cluster with anomalously high resistance. For example, channels that bypass "choke points" (sections of the principal component of the infinite cluster formed by an anomalously small number of resonant sites),[c] for an example see Figure 4.11. Or short channels that bypass long paths in principal component of the infinite cluster. The limiting factor for transport in these parallel channels would be the hopping probability, rather than the diffusive electron transport, therefore the highest contribution to conductivity would come from paths with the fewest hops.

Given that most of the sample length is covered by the diffusive motion of electrons, rather than hopping, the conductivity of these channels would be greater than hopping exclusively through localised sites. Furthermore, as indicated by measurements, the metallic conduction channel is temperature independent down to $\approx$20 K; that is, diffusion through delocalised states is temperature-independent. We can therefore conclude that the temperature dependence of conductivity in these channels is the result of hopping process.

It is worth emphasizing that hopping enables the utilisation of delocalised regions that would otherwise not contribute to charge transport, leading to an enhancement in conductivity. Or looking at it from the other side, the conduction of electrons through delocalised regions within the sample effectively reduces the distance that electrons need to hop in order to traverse the sample.

[c] When considering a sample cross-section perpendicular to the current, "choke points" would be points along the length of the sample where the area occupied by the principal component of the infinite cluster was anomalously small.

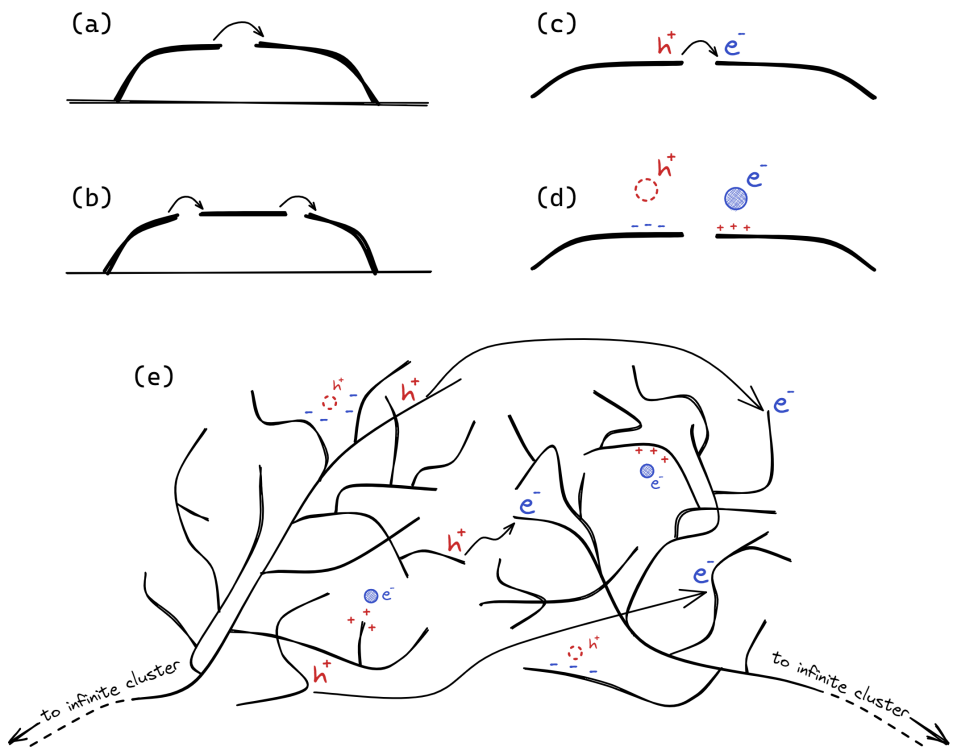

Figure 4.12: Illustrations of the hopping process between delocalised regions of a system. (**a**) Hopping between two dead ends and (**b**) hopping through an isolated pocket in a channel parallel to the infinite cluster (**c**) Creation of an electron-hole pair after hopping between two delocalised regions separated by localised sites. (**d**) Effects of electrons and holes trapped in the localised states. (**e**) A more detailed illustration of the complex shape of the branches of delocalised regions in the vicinity of a hopping location.

Hopping of an electron between two delocalised regions separated by localised sites (dead ends and/or isolated pockets) will create an electron-hole pair, as illustrated in Figure 4.12(c). These charges then move diffusively through the delocalised regions and contribute to charge transport. Hopping can be thought of as a process of creating an electron-hole pair separated by a barrier of localised sites. The hopping process determines the number of charge carriers, while the diffusive motion dictates their mobility.

We now turn to the process of hopping between the delocalized regions and the resulting temperature dependence. This process has a lot of similarities to hopping granular materials. In our model we have hopping between regions of delocalized states separated by localised sites, in granular metals the hopping occurs between metallic granules separated by an insulating matrix. Both hopping processes involve creation of charges, electron-hole pairs or pairs of charged granules.

Just as the granules have numerous states an electron can hop to, the delocalized regions also contain a multitude of states that are close in energy, this includes the initial energy state of the electron. Therefore, an electron will always be able to find an empty state on the other side of the localized region to hop into. This would correspond to a simple tunnelling process between distant sites, and would only depend on the separation distance due to a small overlap between sites $\propto \exp(-2r/\xi)$. However, this would be a constant, temperature-independent process, and would not be able to reproduce the observed temperature dependence.

However, just like in granular metals, hopping of the electron will charge two separated delocalised regions. The energy required to charge a delocalised region is given by:

$$E_{\mathrm{ch}} = \frac{e^2}{2C} \,, \tag{4.10}$$

where C is capacitance involved with charging one region, and is highly dependent on the features of the delocalized regions in the vicinity of the hopping site. Therefore, for an electron to hop it would need enough energy to charge the starting and final delocalised region. Just like granular metals, this would open a hard gap in the electron-hole excitation spectrum, and would result in an activation behaviour, not VRH conductivity with $p = 1/2$ exponent.

In granular metals, it was reported [122], that the capacitance disorder and variation in separation between granules are not enough to remove the hard Coulomb gap in the associated electron-hole excitation spectrum, the so-called *density of ground states*, and random charging of the granules in the ground states is required to close the hard gap. This charging is the result of charge disorder from impurities and defects in the insulating layer [122]. Similarly, the localised states in our system can contain trapped holes (empty localised states below the Fermi level) and electrons (filled localised states above the Fermi level), which could alter the local Coulomb potential, as illustrated in Figure 4.12(d). But while the isolated pockets could be charged in a fashion similar to metal granules, the same cannot be said for dead ends which are all connected by the infinite cluster, and will therefore always remain neutral in the ground state.

More specifically, however, in the case of a low density of metallic granules, it is the fluctuation of the electrical potential, arising from variations in position and charge of impurities and metallic granules, that smears the density of ground states and eliminates the hard Coulomb gap at the Fermi level [122]. While the fluctuation of the electrical potential in granular metals is predominately the result of a random distribution of charges

on granules, in the absence of charged granules, the charge variations in impurities could potentially still smear the density of ground states, just at a higher concentration of impurities.

As illustrated in Figure 4.12(e), in the vicinity of a hopping location the structure of the delocalised regions is quite complex, due to the assumed random distribution of localised and delocalised sites. Therefore, charge impurities in localized sites, originating from trapped holes and electrons, along with a high variability in charging capacitances, which can be expected to be greater than in granular metals, coupled with screening from neighbouring branches, could eliminate the charging penalty between sections of neighbouring delocalized regions. In other words, the hard gap could be closed.

Similarly, to granular metals, and as previously discussed in 2.2, incorporating the Coulomb interactions $e^2/\kappa r_{ij}$ between generated electrons and holes leads to the appearance of a soft Coulomb gap at the Fermi level in the electron-hole excitation spectrum. Consequently, we arrive at the ES VRH temperature dependence characterized by Expression (2.20).

Unlike granular metals, the long range hopping is not due to co-tunnelling between distant granules each associated with a different energy in the density of ground states. In our model, the hopping always occurs between two neighbouring delocalized regions, where different sections (branches) of the delocalized regions are associated with different Coulomb charging energies E_{ch} due to variations in the local capacitance and electrical potential. Since most of the charge transports in the parallel channels occurs through diffusive motion, the exact position of the hopping sites on a pair delocalized regions is irrelevant to conduction. The important contribution of the hopping process is the creation of electron-hole pairs. The hopping process therefore optimizes for pairs of hopping sites on two neighbouring delocalized regions, which are separated in distance by r_{ij} and in energy ΔE_{ij}, where ΔE_{ij} is the result of Coulomb charging energies E_{ch} at sites i and j and the Coulomb interaction energy $e^2/\kappa r_{ij}$. See Figure 4.12(e) for an illustration.

At higher temperatures, when the thermal energy $k_{\mathrm{B}}T$ exceeds the width of the Coulomb gap Δ_{CG} a transition to Mott VRH followed by a transition to the NNH regime, is expected. [113, 122]. Although for high values of Δ_{CG}, the transition could bypass Mott VRH and move directly into activation-like behaviour of the NNH regime. This was suggested to be the case for granular metals [145]. It is possible that the high temperature deviation of resistivity from the proposed two-channel model, observed in our samples above approximately 200 K, could be due to a change in the hopping regime. Specifically, the decrease below the fitting function, observed in most measurements, is accompanied

by an upward deviation of the logarithm special derivative $\ln(W)$ from the $p = 1/2$ line, towards $p = 1/4$. However, the data is generally too noisy and the temperature range too short to confirm this proposition at this point. As previously proposed, in order to clarify this situation, precise resistivity measurements above 300 K are needed.

Before proceeding further, we note that variations of disorder throughout the sample could give rise to regions with higher and lower proportions of localized states. This would produce the same outcome as discussed above, albeit at a different spatial scale. In this scenario, the black and grey areas in Figure 4.11 would correspond to regions of higher and lower proportions of localized states. This is similar to what was proposed in the beginning of this subsection, with a major difference that hopping would occur between separated delocalized states, rather than through localized states.

We can also investigate what would happen across an Anderson MIT. The outcome will depend on the position of the Fermi level. If the Fermi level is situated in the middle of the band, the transition will take place when all states are localized. In this state of the system, the conduction will proceed through hopping between localized states.

However, if the Fermi level is not found in the middle of the band, the transition can occur before all states are localized, specifically when the Fermi level crosses the mobility edge. In this scenario, there could still be delocalized states in the middle of the band, as illustrated in Figure 2.2. The delocalized states will either be entirely empty or occupied, depending on whether the Fermi level is below the lower mobility edge at E_{C}, or above the upper mobility edge at E'_{C}. Charge transport can then occur either through hopping across localized states or via activation in to empty, or out of occupied delocalized states.

A different outcome could emerge, if the transition takes place by cutting the infinite cluster of delocalized regions into two or more finite clusters, without altering the position of the Fermi level with respect to the mobility edge. Without the infinite cluster, the charge transport will continue via hopping between finite clusters, analogous to the charge transport in granular metals. This situation could arise in very thin films, where limited thickness of the finite sample could disrupt the infinite cluster. Above the percolation threshold, an infinite sample would possess an infinite cluster, but a finite sample with sufficiently small dimensions might only contain finite clusters that do not extend across the entire sample.

By examining amorphous thin films of our alloys with diminishing thickness, we should observe a decrease of conductivity in the metallic channel until it vanishes entirely as the infinite cluster of delocalized regions is broken. Subsequently, we should only observe the VRH-like conduction, which resembles ES VRH in granular metals.

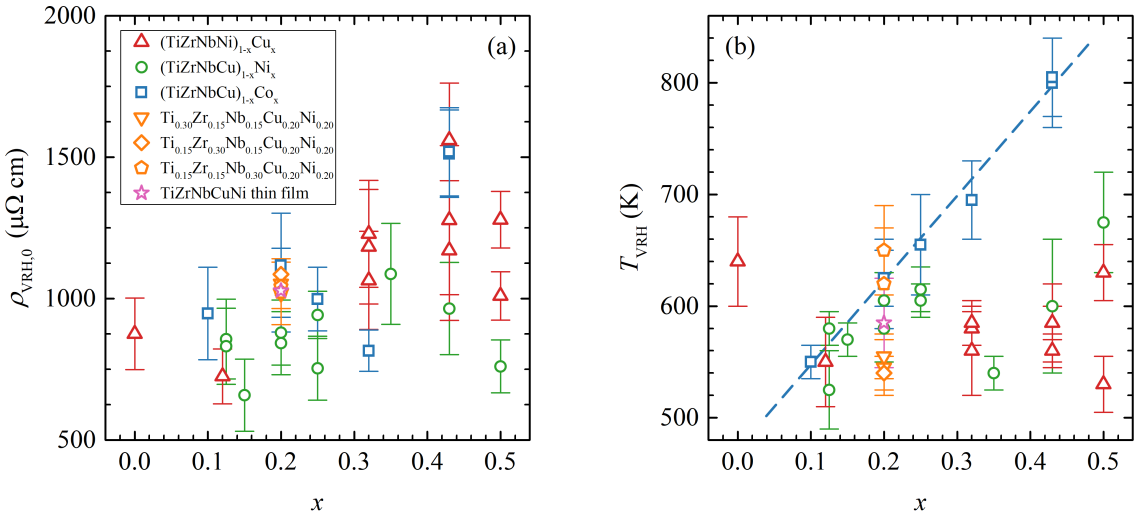

Figure 4.13: Composition x dependence of the fitting parameters T_{VRH} (**a**) and $\rho_{\mathrm{VRH},0}$ (**b**) for Cu_x (red up-triangles), Ni_x (green circles), Co_x (blue squares) alloy systems. Additionally, three alloy variants with fixed (CuNi) content Ti_{30} (orange down-triangle), Zr_{30} (orange diamond) and Nb_{30} (orange pentagon), and the amorphous thin film sample CA011b_1 (magenta star) are shown. The dashed line is provided as a guide to the eye. Multiple data points at the same composition x correspond to multiple measured samples.

Increased values of resistivity compared to related metallic glass ribbons have been previously observed in amorphous thin films [126–128]. Moreover, the resistivities of amorphous thin films have been found to increase with decreasing thickness [129, 130], with the rate of increase increasing as the thickness is reduced. For example, the resistivity of $Ti_{0.77}Co_{0.23}$ increased from about 130 μΩ cm at 140 nm to 267 μΩ cm at 8 nm [129]. The value at 140 nm is somewhat lower than values found in the related $Zr_{1-x}Co_x$ metallic glasses, but it is unclear if the reported thin films were fully amorphous. Furthermore, TCR values were found to increase with increasing resistivity, in agreement with the Mooij correlation [127]. These observations are consistent with our model, even though no MIT transitions were observed down to 8 nm. In thin films, the contribution from the principal component of the infinite cluster is suppressed, thus increasing resistivity. Consequently, the contribution from parallel channels exhibiting a VRH temperature dependence would increase, leading to a higher TCR. However, it also needs to be noted that resistivity in thin films will increase due to an enhanced contribution from conduction electron scattering on the surface, as well as when the film thickness approaches the electron mean free path.

We can now compare the results of the fitting procedure to the two conductance channels with this model. Clearly, the precise contribution to the conductivity from the parallel channels will be strongly dependent on the specific forms of the infinite and finite clusters, i.e. the extent to which parallel channels bypass the infinite cluster and how effectively they do so. This could account for the considerable scatter in the observed values of $\rho_{\mathrm{VRH},0}$, as found in Figure 4.13(a). However, it is difficult to assess the relative significance of this contribution to the scatter in comparison to the contribution arising from the high variability of room-temperature resistivities in small samples, and whether there is any correlation between the two.

On the other hand, T_{VRH} values, as found in Figure 4.13(b), would be entirely dependent on the hopping process, and consequently, the local structure of delocalised regions and localised sites in the vicinity of hopping sites. For Ni_x and Cu_x samples, T_{VRH} remains, within some scatter, constant with changing concentration x. However, for Co_x, T_{VRH} exhibits a clear increase with increasing Co concentration. This difference could be attributed to the Co d-band, which is situated closer to the Fermi level than the Ni and Cu d-bands. As previously noted for the Hall effect results, with increasing Co content in Co_x, the ratio of Co d-states near the Fermi level increases more rapidly than is the case for Ni d-states in Ni_x and Cu d-states in Cu_x.

In granular metals, it has been observed that T_{ES} does not vary with the change in size (structure) of metal granules but only with the volume concentration of the metal [120]. This observation is supported by theoretical considerations [122]. This suggests that the observed T_{VRH} increase with Co content in our Co_x alloys could be attributed to an increase in the ratio of localized to delocalized regions. This, in turn, would be consistent with the increase of ρ_{RT} with increasing Co content, due to a reduction in the size of the principal component of the infinite cluster.

The values of T_{VRH} a $\rho_{\mathrm{VRH}}(T)$ appear to agree well with those of $\mathrm{Ni}_{0.20}$ metallic glass ribbon samples. Although if the value of resistivity in our thin film is higher than the bulk, as in $\mathrm{Ti}_{1-x}\mathrm{Cu}_x$ amorphous thin films [127], the value of $\rho_{\mathrm{VRH}}(T)$ would be higher as well.

In the following paragraphs, we shall highlight some open questions and problems, and potential applications of this model. The assumption that regions of localised states exist, separating regions of delocalized states, is acceptable in a simple model where each site contributes one state, local orbital, to form collective wavefunctions. However, what are the implications for the model, if each site contributes multiple initial states/wavefunctions?

If all these orbitals were of the same character, s, p, or d, it would not be a significant stretch to assume that for a given site, they would all be either localized, or delocalized, particularly in the Lifshitz model where localization is dependent on the ratio of the wavefunction's localization length and the average separation between sites. The problem emerges when sites contain two types of electrons at the Fermi level, for example, s- and d-states in the case of our alloys, where the s orbitals extend further from the atom and are therefore more likely to overlap and from delocalized states than d orbitals. Can the associated s- and d- bands be treated independently with two separate structures of localized and delocalized regions seen in Figure 4.11, with electrons scattering between the two? Or do they have to be treated collectively, and what are then the implications for this model? Furthermore, what is the significance of the s-d hybridization proposed to explain the Hall effect measurements?

This model for VRH-like parallel conduction mode is formed only with the assumption of the coexistence of delocalized and localized regions due to disorder near the metal-insulator transition. This would suggest that it should be applicable in describing the negative temperature coefficient of resistivity in other high-resistivity metallic disordered systems, particularly other amorphous TE-TL alloys, as our measurements indicate no significant difference between our multicomponent and binary TE-TL alloys. This is further bolstered by the success of U. Mizutani and colleagues in fitting the empirical function (1.26) to resistivities of a variate of TE-TL and other amorphous alloys in the 30-300 K range [76–80].

However, due to the small contribution of the VRH-like conduction mode (3-5 % at room temperature), two practical limitations exist. First, the temperature measurements of resistivity must be highly precise; second, the metallic component must be temperature-independent for a wide range of temperatures. Otherwise, it would be challenging or even impossible to successfully disentangle the metallic and VRH-like conduction channels in the temperature dependence of resistivity.

4.3.3 Low-temperature resistivity

In all the samples measured, we observed an increase in resistivity in the low-temperature regime, a trend routinely observed in non-magnetic TE–TL alloys. This increase had been attributed to the EEI effect, which dominates the variation in low-temperature resistivity with the characteristic dependence $\Delta\rho(T) \propto -\Delta\sigma(T) \propto -\sqrt{T}$ [3].

As was reported elsewhere [3, 45, 71, 80], we too found it difficult to discern weather

$\sqrt{T}$ or $\ln(T)$ resistivity scaling more accurately describes the measured data at low temperatures. In fact, some samples conformed more closely to one or the other scaling law, while the majority could be reasonably well fitted to both. Generally, the temperature range where $\sqrt{T}$ accurately describes the data is a few degrees lower compared to the region where $\ln(T)$ fits the data well.

It is important to note that we performed our fits on the calculated $\rho_{\mathrm{Metal}}(T)$ values, which stands distinct from the current literature where the raw measured low-temperature data was fitted either to $\sqrt{T}$ or $\ln(T)$ [71, 74, 95, 146], or using a combined function of EEI (1.24) and WL (1.21) (with $\tau_{\mathrm{in}}^{-1} \propto T^2$) temperature dependent contributions [72, 73, 147, 148].

Figure 4.14 provides examples of linear fits of $\rho_{\mathrm{Metal}}(T)$ to both $\sqrt{T}$ and $\ln(T)$ for comparison. Given the associated derivatives, neither the $\sqrt{T}$ nor $\ln(T)$ scaling can be definitively preferred in our measured amorphous alloys.

Figure 4.15 provides the fitting parameters of the $\rho_{\mathrm{Metal}}(T)$ functions (4.2) and (4.3). In addition to these fitting parameters, we include the slope values $a_{\mathrm{sqrt}}/\rho_0^2$ and $a_{\ln}/\rho_0^2$ of the temperature scaling of conductivity,[d] given that the EEI and WL equations are defined in terms of conductivity.

Regrettably, the temperature range where a linear variation in $\sqrt{T}$ or $\ln(T)$ can be observed in our samples is limited by superconducting fluctuations and potentially contributions from the Cooper channel of the EEI effect. This is naturally more pronounced for alloys exhibiting higher superconducting transition temperatures T_c at lower TL concentrations x. This observation may account for the decrease in slope values $a_{\mathrm{sqrt}}/\rho_{\mathrm{RT}}$ and $a_{\ln}/\rho_{\mathrm{RT}}$ ($a_{\mathrm{sqrt}}/\rho_0^2$ and $a_{\ln}/\rho_0^2$) for concentrations $x < 0.25$, compared to near constant values for $x > 0.25$. The outlier, $\mathrm{Cu}_{0.0}$, which also presents a lower T_c than expected from its composition x as observed in Figure 4.1, further substantiates this explanation.

The near constant values of $a_{\mathrm{sqrt}}/\rho_{\mathrm{RT}}$ in the $320-560\,\Omega^{-1}\mathrm{m}^{-1}\mathrm{K}^{-1/2}$ range for $x > 0.25$ align with values reported for other TE–TL alloys [74, 149]. We also observe that the slope values for the thin film CA011b_1 exceed those of the corresponding metallic glass ribbons. This indicates a higher resistivity in the thin film in comparison to the ribbon samples, as an increase in resistance would lead to a decrease in the values of $a_{\mathrm{sqrt}}/\rho_0^2$ and $a_{\ln}/\rho_0^2$.[e]

Finally, we note that except for Co_x alloys, T_{sqrt} and $T_{\ln}$ mark the transition point between the low-temperature resistivity variation and the constant ρ_0 value in $\rho_{\mathrm{Metal}}(T)$.

[d] $\Delta\sigma = -\Delta\rho/\rho^2$

[e] Fitting parameter $a_{\mathrm{sqrt}}/\rho_{\mathrm{RT}}$ is normalized and therefore independent of resistivity ρ, this implies that $a_{\mathrm{sqrt}}/\rho_0^2 \propto 1/\rho_0$.

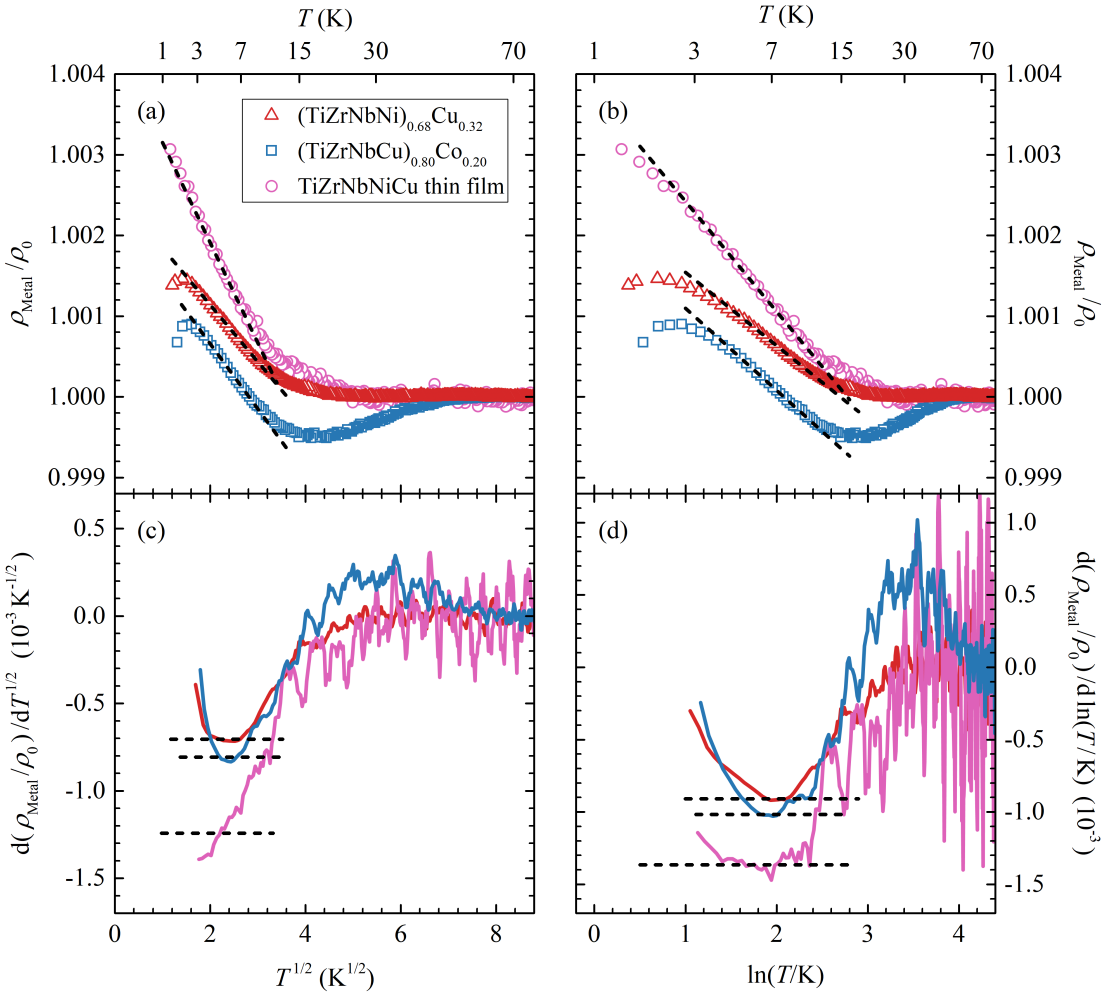

Figure 4.14: Variation of the normalized metallic component of resistivity $\rho_{\mathrm{Metal}}/\rho_0$ with respect to $\sqrt{T}$ (**a**) and $\ln(T)$ (**b**) for representative metallic glass ribbon samples with compositions $Cu_{0.32}$ and $Co_{0.20}$ and the amorphous thin film sample CA011b_1. The dashed lines in these figures represent linear fits. (**c**) and (**d**) show derivatives of the normalized metallic component of resistivity with $\sqrt{T}$ and $\ln(T)$ respectively. The dashed lines in these figures indicate the slope values of the linear fits in (a) and (b).

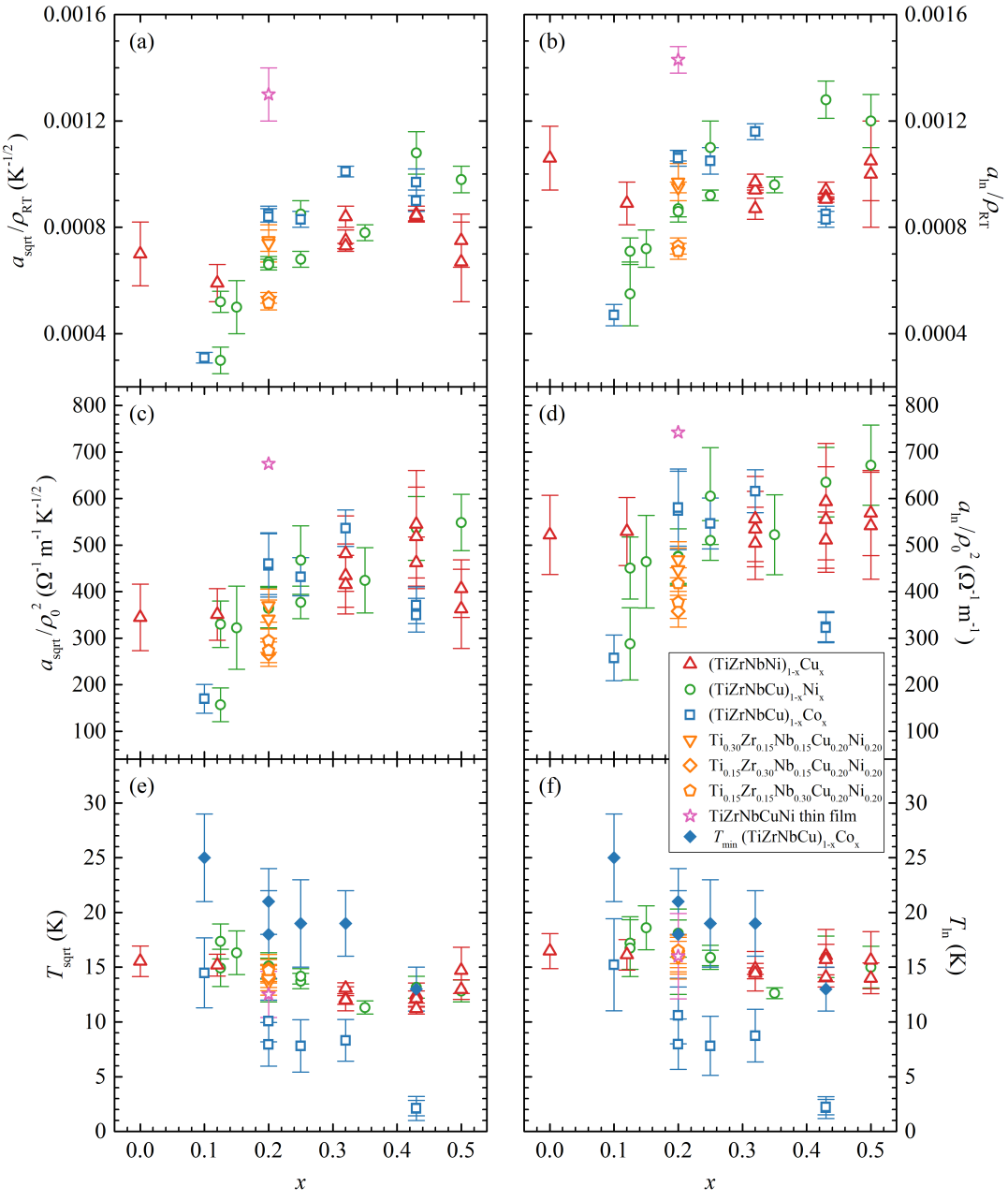

Figure 4.15: Composition x dependence of the fitting parameters a_{sqrt} (**a**), a_{ln} (**b**), T_{sqrt} (**e**) and T_{ln} (**f**), and the derived parameters $a_{\mathrm{sqrt}}/\rho_0^2$ (**c**) and a_{ln}/ρ_0^2 (**d**) for Cu_x (red up-triangles), Ni_x (green circles), Co_x (blue squares) alloy systems. Additionally, three alloy variants with fixed (CuNi) content Ti_{30} (orange down-triangle), Zr_{30} (orange diamond) and Nb_{30} (orange pentagon), and the amorphous thin film sample CA011b_1 (magenta star) are shown. Panels (e) and (f) also show the variation of temperature T_{min} (blue diamond), marking the point of minimum resistivity in $\rho_{\mathrm{Metal}}(T)$, in Co_x alloys. Multiple data points at the same composition x correspond to multiple measured samples.

For Co_x alloys, we added the temperature $T_{\min}$, which marks the point of minimum resistivity in $\rho_{\text{Metal}}(T)$, i.e. the transition, with increasing temperature, from the low-temperature resistivity decrease due to quantum corrections to the resistivity increase due to scattering from spin fluctuations.

For a quantitative analysis we will use $Ni_{0.25}$ as an example, in order to minimize the effects of superconducting fluctuations, and for which the data for $N(E_F)$ is also available [37]. We can determine the value of the diffusion coefficient from the Einstein relation [8]:

$$\sigma = e^2 N(E_F) D \, . \tag{4.11}$$

Using the values for $Ni_{0.25}$, $N(E_F) = 1.14\,\text{eV}^{-1}\,\text{atom}^{-1}$, with a rule-of-mixture value for the atomic volume $V_{at} = 1.6 \times 10^{-29}\,\text{m}^3$[f], and the room-temperature resistivity for the small sample used to measure the resistivity curve $\rho_{RT} = 162.5\,\mu\Omega\,\text{cm}$, we obtain $D = 5.4 \times 10^{-5}\,\text{m}^2\,\text{s}^{-1}$.

Using Equation (1.24) the diffusion coefficient can be derived from the slope of the low-temperature increase a_{sqrt}/ρ_0^2. In a first-order approximation, we use $\tilde{F}^\sigma = 0$ [74], and omit the Cooper channel contribution. Higher values of F^σ would result in lower vales of the diffusion coefficient. From the slope $a_{\text{sqrt}}/\rho_0^2 = 468\,\Omega^{-1}\text{m}^{-1}\text{K}^{-1/2}$ of a $Ni_{0.25}$ sample, we calculate the diffusion coefficient as $D = 3.4 \times 10^{-5}\,\text{m}^2\,\text{s}^{-1}$.

The agreement between the two obtained values is excellent, especially considering the error in determining resistivities. In addition, we emphasize that we used two expressions for the diffusion coefficient D; in one (the Einstein relation) the diffusion coefficient is proportional to conductivity ($D \propto \rho^{-1}$), while in Equation (1.24), the diffusion coefficient is proportional to the square of resistivity ($D \propto \rho^2$), via the dependence on the slope a_{sqrt}/ρ_0^2.

However, a complication arises when we consider that, according to the proposed model, only the principal component of the infinite cluster contributes to diffusive metallic conduction $\rho_{\text{Metal}}(T)$. Hence, the actual value of resistivity ρ' within the infinite cluster will be lower than the resistivity ρ determined with dimensions of the entire sample, rather than the unknown dimensions of the infinite cluster, i.e. $\rho' = \eta\rho$, where $\eta < 1$ represents an unknown scaling. This implies that for any $\rho' < \rho$, the diffusion coefficient calculated through the Einstein relation and the EEI Equation (1.24) would diverge, as the former would increase by η^{-1} and the latter decrease by η^2. Therefore, we can conclude that in the proposed model with two conductance channels, the EEI contribution to conductivity is

[f] $N(E_F) = 7.13 \times 10^{22}\,\text{eV}^{-1}\,\text{cm}^{-3}$

insufficient to fully account for the magnitude of the temperature dependence of resistivity on its own.

It is important to also consider the contribution of the WL correction to conductivity. Notwithstanding that the current theoretical framework cannot account for the observed $\sqrt{T}$ or $\ln(T)$ scaling, barring a potential $\tau_{\text{in}}^{-1} \propto T$ contribution from TLS. However, MR measurements in binary TE–TL alloys returned a $\tau_{\text{in}}^{-1} \propto T^2$ scaling [3].

In addition, we also note that in binary TE–TL alloys the bulk of the MR magnitude in the low-temperature limit ($\lesssim 30\,\text{K}$) has been attributed to the WL contribution, with corrections from the EEI contribution and superconducting fluctuations [3, 8]. Despite the apparent dominance of the EEI contribution in the temperature variation of resistivity, the magnetic field variation is primarily governed by WL and weak antilocalization (WAL).

A unique aspect of our model is the clear observation of the constant Boltzmann contribution ρ_0 to the total resistivity, in $\rho_{\text{Metal}}(T)$ within the temperature range of 20-200 K. This constant provides a baseline value to which the quantum corrections to resistivity are added. This feature allows, not only the determination of temperature scaling, but also the estimation of the total resistivity contribution from quantum corrections. Furthermore, we can observe the breakdown of quantum corrections with increasing temperature. This occurs as the thermal coherence time τ_{T}, and the phase-breaking time τ_{φ} (τ_{in}), approach the value of the elastic scattering time τ_{e}.

Assuming that the contribution from WL vanishes when τ_{in} aligns with τ_{e}, we can leverage Equation (1.22), with $\tau_{\text{in}} = \tau_{\text{e}}$, to estimate the value of τ_{e}. In essence, the total contribution to resistivity from WL, σ^{WL}, identified in the zero-temperature limit, must be equivalent in magnitude and opposite in sign to the temperature-dependent contribution from WL when $\tau_{\text{in}} = \tau_{\text{e}}$.

Further assuming that the entire low-temperature increase is attributable to WL, we arrive at:

$$\sigma^{\text{WL}} = -\frac{a_{\text{sqrt}}}{\rho_0^2}\sqrt{T_{\text{sqrt}}} = -\Delta\sigma^{\text{WL}}\left(\tau_{\text{e}}\right) = -\frac{e^2}{2\pi^2\hbar(3D)^{1/2}}\left(\frac{1}{\tau_{\text{e}}}\right)^{1/2}, \tag{4.12}$$

where the factor $3^{-1/2}$ was added to account for the difference between ballistic motion in time τ_{e} and diffusive motion over longer periods. For the diffusion coefficient we use the values determined from the Einstein relation.

However, it must be noted that the contribution from the WL effect should decay considerably before τ_{in} reaches the value τ_{e}. Moreover, Equation (1.21) and consequently Equation (1.22) were ascertained in the $\tau_{\text{in}} \gg \tau_{\text{e}}$ regime.

Despite this, Expression (4.12) can be used to estimate the value of τ_e and juxtapose it against the value computed from the free electron Drude formula, given by:

$$\sigma = \frac{ne^2\tau_\mathrm{e}}{m_e} \,, \tag{4.13}$$

where n denotes the charge carrier density. Assuming that each atom contributes one conduction electron and using the rule-of-mixtures density, we determine a charge carrier density of $n \approx 6.3 \times 10^{22}\,\mathrm{cm}^{-3}$ for $\mathrm{Ni}_{0.25}$.

By using the same resistivity and slope data for the $\mathrm{Ni}_{0.25}$ sample, we are able to calculate $\tau_\mathrm{e}^\mathrm{Drude} = 3.5 \times 10^{-16}\,\mathrm{s}$ using the Drude expression and $\tau_\mathrm{e}^\mathrm{WL} = 3.1 \times 10^{-13}\,\mathrm{s}$ by employing Equation (4.12). A discrepancy of three orders of magnitude exists between these values, which suggests that the WL contribution to resistivity in our samples should be larger than what we have measured.

However, we must once again consider that the diffusive-current-carrying principal component of the infinite cluster is smaller than the whole sample, and accordingly rescale the resistivity as $\rho' = \eta\rho$. This, in turn, modifies the slope values to $(a_\mathrm{sqrt}/\rho_0^2)' = \eta^{-1}(a_\mathrm{sqrt}/\rho_0^2)$ and the diffusion coefficient determined from the Einstein relation to $D' = \eta^{-1}D$. For instance, using $\eta = 0.2$, we obtain $\tau'^\mathrm{Drude}_\mathrm{e} = 1.8 \times 10^{-15}\,\mathrm{s}$ and $\tau'^\mathrm{WL}_\mathrm{e} = 2.5 \times 10^{-15}\,\mathrm{s}$, which agree far better. The $\eta = 0.2$ value implies that 20 % of the sample contributes to metallic conduction, and not that only 20 % of sites (localized atomic orbitals) form delocalized states.

We are now faced with a new issue, as these elastic scattering times τ'_e are significantly shorter than both the thermal dephasing time $\tau_\mathrm{T} = 4 \times 10^{-14}\,\mathrm{s}$ and an estimated value of the inelastic scattering time $\tau_\mathrm{in} = 4.4 \times 10^{-13}\,\mathrm{s}$, as reported by J. B. Bieri et al. [88] for $\mathrm{Zr}_{0.43}\mathrm{Cu}_{0.57}$ at 30 K.[g] This is the temperature at which no indications of the low-temperature resistivity increases due to quantum corrections are observable, except for possibly Co_x alloys.

This suggests one of two possibilities: either the elastic scattering time τ_e is considerably longer, which would then approach values seen in good metals ($10^{-14}\,\mathrm{s}$), or a different mechanism could be responsible for the loss of interference in the quantum corrections as the temperature approaches 30 K. The former seems unlikely, as we observe no contribution from electron-phonon scattering in the metallic (Boltzmann) contribution to resistivity, implying that $\tau_\mathrm{e} \ll \tau_\mathrm{in}$ even at room temperature. As for the latter,

[g] J. B. Bieri et al. [88] provide the temperature scaling $\tau_\mathrm{in}^{-}1 = 2.5 \times 10^9\,\mathrm{s}^{-1}\,\mathrm{K}^{-2}T^2$ for $\mathrm{Zr}_{0.43}\mathrm{Cu}_{0.57}$. The inelastic scattering times should also be rescaled with η as $\tau'_\mathrm{in} = \eta^{-1/3}\tau_\mathrm{in} = 2.6 \times 10^{-13}\,\mathrm{s}$ (see Equation (1.30c)), however this change is negligible, and we opt to use the original values.

it is difficult as this stage to speculate on the validity of such a proposition, particularly given the potential implications for the magnetoresistance, which is also sensitive to phase-breaking processes. Consequently, additional research is necessary to investigate this matter further.

At this juncture, the source of the observed low-temperature increase in resistivity remains ambiguous — it could stem from contributions from either EEI or WL, or a combination of both. We also note, that the confined environment within the infinite cluster could potentially alter the effective dimensionality of the sample. This infinite cluster, with variable size and shape throughout the sample, could lead to some intriguing physical implications. In particular, if at any point the cluster size in one or two dimensions is smaller than $\sqrt{D\tau_{\text{in}}}$ or $\sqrt{D\tau_{\text{T}}}$ — the distances a diffusive electron can traverse before its phase coherence is destroyed — the quantum corrections at that point will behave as if the system is effectively lower-dimensional $d < 3$. In case of $d = 2$, both the EEI and WL temperature-dependent contributions will scale as $\ln(T)$, irrespective of the polynomial scaling factor of τ_{in} [41, 63]. Such a shift in dimensionality would have significant implications for MR as well.

4.3.4 Magnetoresistance

Figures 4.16 and 4.17 display the variation of MR with $\sqrt{\mu_0 H}$ and $(\mu_0 H)^2$ at different temperatures for selected metallic glass ribbon samples. The observed magnetic field variation and values are similar to the MR in $Zr_{0.43}Cu_{0.57}$ shown in Figure 1.14, and consequently other binary non-magnetic TE–TL alloys. MR in the thin film sample CA011b_1 exhibited similar qualitative and quantitative behaviour to the metallic glass ribbons.

All measured samples displayed positive MR, with no negative slopes detected up to 10 T, which was the maximum measured field for most samples. In measurements with higher magnetic fields, a minimal negative slope was found at 1.3 K in the $Co_{0.10}$ sample between 10-14 T and in the $Ni_{0.20}$ sample between 10-16 T. However, these negative slopes are barely distinguishable from the measurement noise ($\approx$0.01 %). Conversely, MR in the $Co_{0.25}$ sample showed an increase at 1.3 K up to 14 T.

Due to contributions from superconducting fluctuations (Aslamasov-Larkin and Maki-Thomson), relatively large MR values are observed at low temperatures (blue circles), particularly in samples with higher superconducting transition temperature T_c, lower TL concentrations. The low-temperature MR curves seem to saturate at higher magnetic

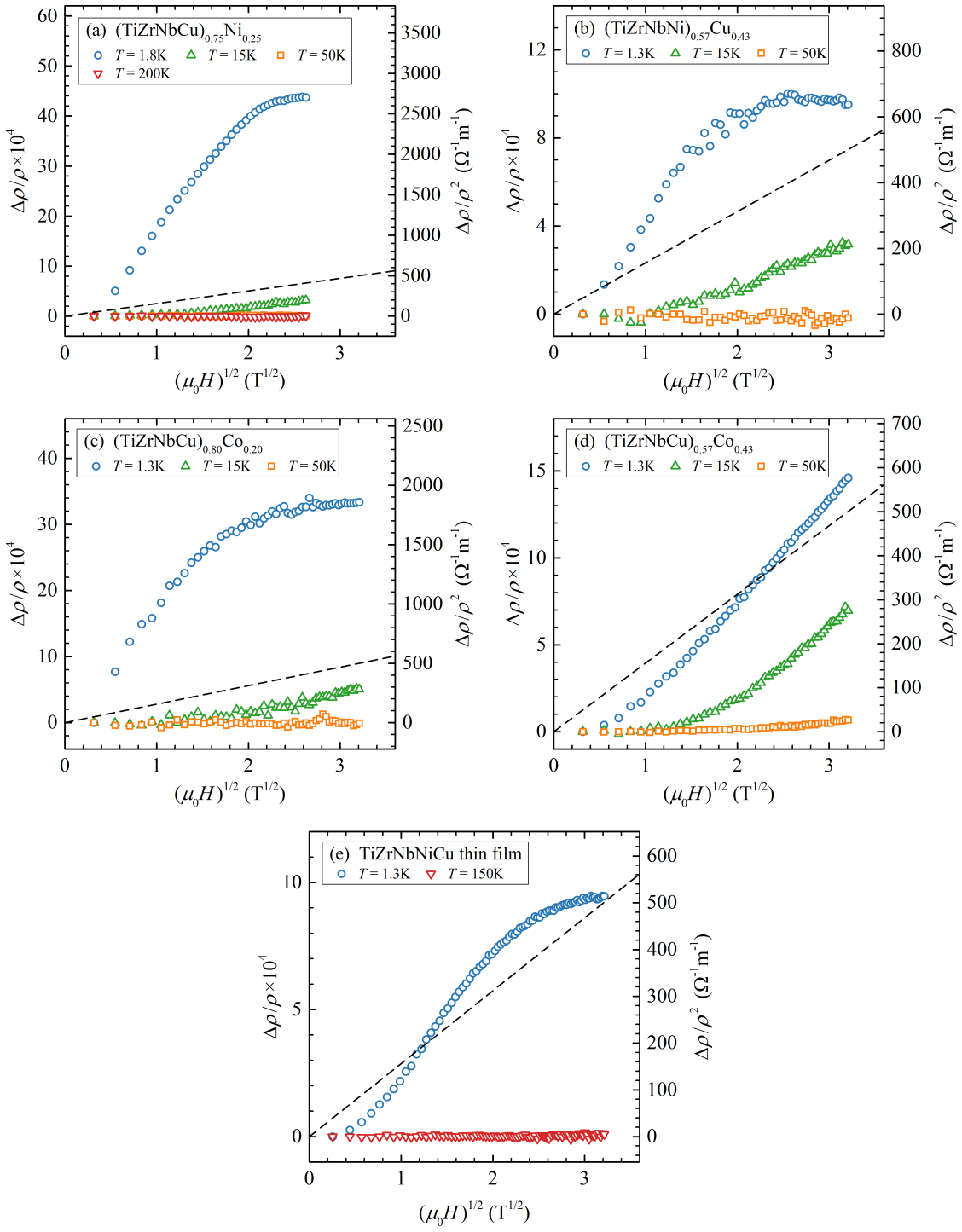

Figure 4.16: Magnetoresistance as a function of $\sqrt{\mu_0 H}$ at a set of temperatures is shown for selected metallic glass ribbons: (**a**) $Ni_{0.25}$, (**b**) $Cu_{0.43}$, (**c**) $Co_{0.20}$, (**d**) $Co_{0.43}$, and (**e**) for the amorphous thin film sample CA011b_1. The dashed lines represent the temperature independent MR scaling of Equation (1.30c).

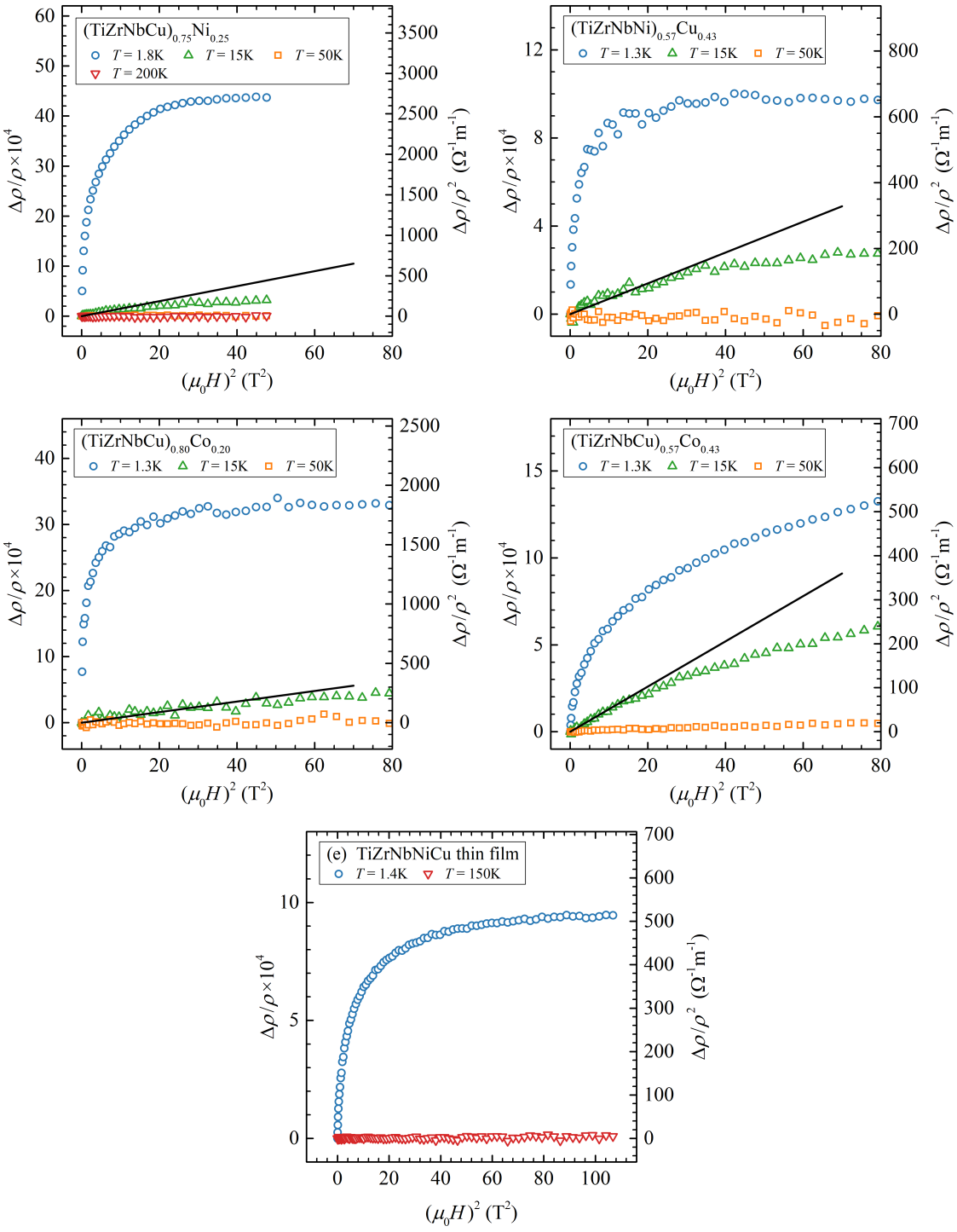

Figure 4.17: Magnetoresistance as a function of $(\mu_0 H)^2$ at a set of temperatures is shown for selected metallic glass ribbons: (**a**) $Ni_{0.25}$, (**b**) $Cu_{0.43}$, (**c**) $Co_{0.20}$, (**d**) $Co_{0.43}$ and (**e**) for the amorphous thin film sample CA011b_1. The solid lines in these figures represent linear fits at low magnetic fields.

fields, except for Co_x samples with $x \geq 0.20$, where saturation is not reached up to 10 T (14 T for $Co_{0.25}$).

The MR in the thin film samples resembles the values found for $Cu_{0.43}$ more closely than those for $Ni_{0.25}$. This suggests that the superconducting transition temperature is suppressed in our thin film compared to the related metallic glass ribbon sample. This observation is further supported by the temperature variation of resistivity in the thin film sample, as seen in Figure 4.14. Here, the drop due to superconducting fluctuations is observed at lower temperatures than in $Co_{0.20}$ and $Cu_{0.34}$, which have comparable or lower transition temperatures than the $Ni_{0.20}$ and $Cu_{0.20}$ ribbon samples. Resistivity measurements in the He3 cryostat at temperatures below 1.3 K, in order to determine the superconducting transition temperature, have yet to be conducted.

There are noticeable differences between the MR curve shapes in $Cu_{0.43}$ and $Co_{0.43}$,[h] which may be tentatively attributed to spin fluctuations [142], the presence of which we observed in the temperature dependence of resistivity.

The spin-orbit time was found to be similar between binary Zr–Cu, Zr–Ni, and Zr–Co alloys [88, 142]. As such, the observed differences should not be the result of increased spin-orbit scattering in Co_x alloys. However, it is imperative to note that suppression of spin fluctuations in a magnetic field theoretically induces a negative MR [150]. As already noted, no negative MR was observed up to at least 100 K, although a more precise MR measurement is warranted for definitive conclusions.

At an intermediate temperature (green triangles; 15 K), we observe a nearly linear variation with $\sqrt{\mu_0 H}$. However, the slopes do not align with the universal slope from Equation (1.30c) (represented by the dashed lines), just as is the case in $Zr_{0.43}Cu_{0.57}$. This discrepancy is attributable to the combined influence of superconducting fluctuations and EEI MR. At higher temperatures (orange squares and red down triangles; $\geq$50 K), no discernible MR within the measurement noise was detected in all samples, with the exception of Co_x alloys with $x \geq 0.20$.

From the slope of the MR curves vs $(\mu_0 H)^2$ in low magnetic fields at 15 K, as shown in Figure 4.17, the values of the inelastic scattering time τ_{in} can be calculated with Equation (1.30b). Using $Ni_{0.25}$ as a representative example, and employing the previously calculated diffusion coefficient from the density of states and resistivity, $D = 5.4 \times 10^{-5}\,\text{m}^2\,\text{s}^{-1}$, the value $\tau_{\text{in}} = 1.4 \times 10^{-12}\,\text{s}$ is calculated. This is close to the $\tau_{\text{in}} = 1.8 \times 10^{-12}\,\text{s}$ value at 15 K provided by J. B. Bieri et al. [88] for $Zr_{0.43}Cu_{0.57}$.

[h] $Cu_{0.43}$ exhibits a superconducting transition at $T_c = 0.36$ K, while in $Co_{0.43}$ no superconducting transition was observed down to 0.3 K

As for $Cu_{0.43}$, $Co_{0.20}$, $Co_{0.43}$ samples, the values of the density of states $N(E_F)$, which are necessary to determine the diffusion coefficient, are not presently known. However, we can make a rough approximation for the density of states $N(E_F) = 1\,\mathrm{eV}^{-1}\,\mathrm{atom}^{-1}$ in order to calculate the diffusion coefficients D and the scattering times τ_{in}. We obtain $D = 6.2 \times 10^{-5}\,\mathrm{m}^2\,\mathrm{s}^{-1}$ and $\tau_{in} = 7.5 \times 10^{-13}\,\mathrm{s}$ for $Cu_{0.43}$, $D = 5.7\,\mathrm{m}^2\,\mathrm{s}^{-1}$ and $\tau_{in} = 7.8 \times 10^{-13}\,\mathrm{s}$ for $Cu_{0.20}$, and $D = 3.6 \times 10^{-5}\,\mathrm{m}^2\,\mathrm{s}^{-1}$ and $\tau_{in} = 1.4 \times 10^{-12}\,\mathrm{s}$ for $Co_{0.43}$. These values are in good agreement with each other, more so considering the rough nature of the approximations used.

As mentioned in the preceding section 4.3.3, τ_{in} values need to be rescaled in accordance with resistivity when considering the model proposed to explain the two conductance channels in subsection 4.3.2. With the rescaled values obtained as $\tau'_{in} = \eta^{-1/3}\tau_{in}$. However, this rescaling will not significantly alter the values of τ_{in}.

The temperature-dependent resistivity in a magnetic field, compared against the zero field curve, can be seen in Figure 4.18. At higher temperatures, the two curves align, signifying the absence of MR above 50 K with the exception of the Co_x alloy, wherein a minor MR was still detected at somewhat higher temperatures. Interestingly, the $\sqrt{T}$ scaling, not only persists, but improves in the magnetic field at low temperatures, especially so in alloys possessing higher values of the superconducting transition temperature T_c. This can be attributed to the suppression of the superconducting fluctuations (Aslamasov-Larkin and Maki-Thomson) in the magnetic field. Moreover, the $\ln(T)$ scaling remains observable as well. However, the temperature range in good agreement with $\ln(T)$ scaling shifts towards higher temperatures.

While the present measurements are sparse and noisy, they show good qualitative and even quantitative agreement with MR measurements in binary amorphous TE–TL alloys. To perform a thorough analysis of MR in our quinary alloys, ribbons and thin films, a comprehensive and systematic set of measurements in varying magnetic fields and temperatures needs to be conducted. However, before that, more effort is needed to find ways of reduce the noise in MR measurements, for example, by reducing the contact resistance.

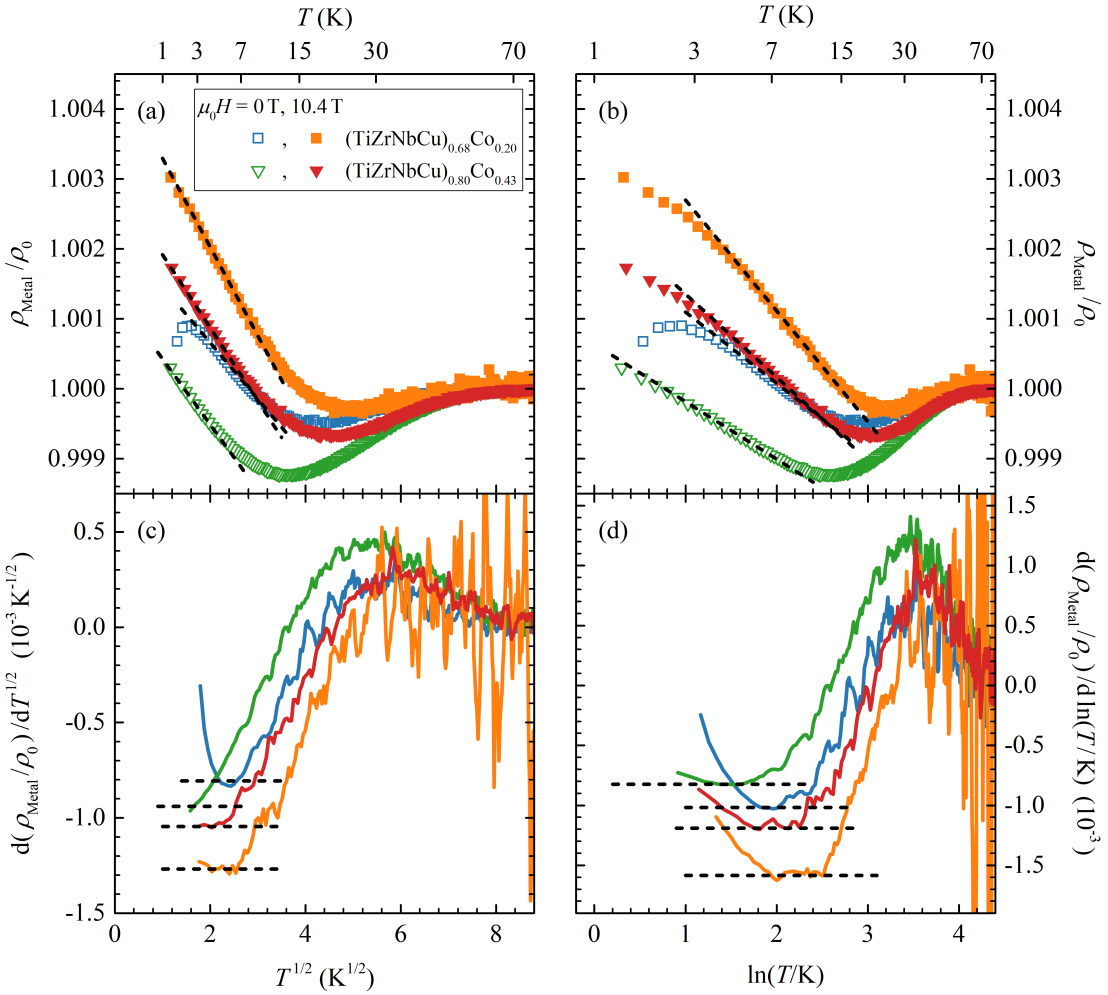

Figure 4.18: Variation of the normalized metallic component of resistivity $\rho_{\mathrm{Metal}}/\rho_0$ with respect to $\sqrt{T}$ (**a**) and $\ln(T)$ (**b**) for selected metallic glass ribbon samples with compositions $Co_{0.20}$ and $Co_{0.43}$ in zero magnetic field and at $\mu_0 H = 10.4\,\mathrm{T}$. The dashed lines in these figures represent linear fits. (**c**) and (**d**) show derivatives of the normalized metallic component of resistivity with $\sqrt{T}$ and $\ln(T)$ respectively. The dashed lines in these figures indicate the slope values of the linear fits in (a) and (b).

Chapter 5

Summary and Outlook

As part of this work, we sought to expand our understanding of amorphous alloys, particularly those comprised of early and late transition metals. Our initial interest was in exploring the roles and interplay of chemical and structural disorder within these materials. To this end, we examined the transport properties of quinary TE–TL alloys, including resistivity, Hall effect, magnetoresistance, and superconductivity.

Our investigation centred on metallic glass ribbons from three alloy systems: Cu_x, Ni_x, and Co_x, along with three alloy variants with a fixed TL (Cu, Ni) content: $Ti_{0.30}$, $Zr_{0.30}$, and $Nb_{0.30}$. Additionally, we also studied an amorphous thin film of TiZrNbCuNi, deposited on a $SrLaAlO_4$ substrate using a PLD system.

In regard to superconductivity, all samples except for $Cu_{0.50}$ and $Co_{0.43}$ were superconducting above 300 mK. We observed low transition temperatures, which can likely be attributed to a negative influence of Ti observed in binary TE–TL, and further illustrated by the lower T_c for $Ti_{0.30}$ compared to $Zr_{0.30}$ and $Nb_{0.30}$. The supercontracting transition temperatures T_c decreased with increasing TL content, in line with amorphous and crystalline TE–TL alloys.

The Hall coefficients also showed good agreement with amorphous binary TE–TL alloys. Hall coefficients were positive, with the exception of $Co_{0.43}$. For Co_x alloys, a change in R_H sign was observed with an increasing concentration x, with the critical concentration around $x(\mathrm{Co}) = 0.34$. R_H in Ni_x alloys slightly decreased at higher concentrations x, with an extrapolated critical concentration of approximately $x(\mathrm{Ni}) = 0.6$. Conversely, Cu_x alloys remained constant for the entire measured concentration range.

We found that all metallic glass ribbon samples exhibited high room-temperature resistivity (140-240 µΩ cm), coupled with a small negative temperature coefficient of resistivity. The room-temperature resistivities increased with higher TL content in line with related

binary TE–TL alloys, except for Co_x alloys which show a more significant increase than expected from $Zr_{1-x}Co_x$.

In a magnetic field, all the samples displayed a positive and increasing magnetoresistance up to 10 T, with some indications of a potential negative slope at fields greater than 10 T. The magnetic field variation is consistent with amorphous binary TE–TL alloys — roughly $\propto B^2$ at low fields, $\propto \sqrt{B}$ at intermediate fields, followed by a saturation-like behaviour at higher fields. Furthermore, the temperature variation of MR can be attributed to the contribution from superconducting fluctuations. This demonstrates a qualitative and even quantitative agreement with binary TE–TL alloys.

To reiterate, these measurements showed good agreement with their binary counterparts, effectively suggesting that these quinary alloys can be regarded as pseudo-binary alloys, $TE_{1-x}TL_x$.

While the temperature dependence of resistivity in our samples can be described by the temperature variation of weak localization and enhanced electron-electron interaction contributions to conductivity, as has been done in amorphous binary and ternary TE–TL alloys, we discovered that a model with two parallel conductance channels better fits the measured temperature variation. This model features a metal-like and a VRH-like channel as $1/\rho(T) = 1/\rho_{\mathrm{Metal}}(T) + 1/\rho_{\mathrm{VRH}}(T)$.

We postulated that the Boltzmann contribution in the metallic channel is dominated by elastic scattering on the disordered lattice resulting in a temperature-independent resistivity at higher temperature ($\gtrsim$ 20 K), and by WL and EEI contributions at low temperatures ($\lesssim$ 20 K). We proposed that the VRH-like conductance channel is the result of the formation of regions of delocalized and localized states. The delocalized states form an infinite cluster that contributes to the aforementioned metallic conductance channel. However, not all portions of the infinite cluster contribute to this diffusive transport of electrons, these portions are termed *dead ends*. Hopping between these dead ends can then contribute to parallel conduction channels. Due to the temperature independent nature of the Boltzmann conduction through the infinite cluster, including dead ends, the temperature dependence of these channels is dominated by the hopping process, resulting in the VRH-like temperature dependence $\exp(T_{\mathrm{VRH}}/T)^{1/2}$.

This model, however, raises questions regarding the influence of localized states on other properties of the system, the role of lower effective dimensionality of the infinite cluster, the nature of the low-temperature resistivity increase and magnetoresistance, and possible effects on superconductivity and the Hall effect. At this stage of research, we are unable to provide satisfactory answers to these questions.

The next step in validating the two-channel conductance model should be to reanalyse previously published measurements of the temperature variation of resistivity in amorphous binary and ternary TE-TL alloys and other high-disorder high-resistivity systems, and where necessary perform new measurements with higher precision.

For the quinary alloys examined in this study, a more detailed set of magnetoresistance measurements should be performed as a function of magnetic field and temperature, given the sparse and noisy data presented in this work. Furthermore, alternative methods of applying contacts (e.g. other types of conductive epoxy glues, wedge and ball bonding, pressure contacts) should be explored in order to reduce contact resistance and measurement noise.

Finally, the thickness of the amorphous thin film reported in this work, estimated to be in the range of 100-200 nm, is still very much within the bulk range. Nevertheless, it demonstrates that amorphous thin films of multicomponent TE-TL alloys can be fabricated, and that their transport properties are in good agreement with those of metallic glass ribbon samples. The next step is to conduct a new series of thin film depositions of varying thicknesses to study the effect of film thickness on the value and temperature variation of resistivity. This could provide valuable insights into the nature of the VRH-like conductance channel we observed. However, a reliable method for independently determining film thickness should be established before proceeding with measurements of resistivity, Hall effects, magnetoresistance, and superconductivity.

References

[1] W. Klement, R. H. Willens, and P. Duwez, Non-Crystalline Structure in Solidified Gold–Silicon Alloys, Nature **187**, 869 (1960).

[2] K. H. J. Buschow, Short-Range Order and Thermal Stability in Amorphous Alloys, J. Phys. F Met. Phys. **14**, 593 (1984).

[3] M. A. Howson and B. L. Gallagher, The Electron Transport Properties of Metallic Glasses, Phys. Rep. **170**, 265 (1988).

[4] H.-J. Güntherodt and H. Beck, eds., *Glassy Metals I*, Topics in Applied Physics, Vol. 46 (Springer, Berlin, Heidelberg, 1981).

[5] H. Beck and H.-J. Güntherodt, eds., *Glassy Metals II*, Topics in Applied Physics, Vol. 53 (Springer, Berlin, Heidelberg, 1983).

[6] H. Beck and H.-J. Güntherodt, eds., *Glassy Metals III*, Topics in Applied Physics, Vol. 72 (Springer, Berlin, Heidelberg, 1994).

[7] U. Mizutani, Electronic Structure of Metallic Glasses, Progress in Materials Science **28**, 97 (1983).

[8] J. S. Dugdale, *The Electrical Properties of Disordered Metals*, Cambridge Solid State Science Series (Cambridge University Press, Cambridge, 1995).

[9] B. Cantor, K. B. Kim, and P. J. Warren, Novel Multicomponent Amorphous Alloys, Mater. Sci. Forum **386–388**, 27 (2002).

[10] L. Ma, L. Wang, T. Zhang, and A. Inoue, Bulk Glass Formation of Ti-Zr-Hf-Cu-M (M=Fe, Co, Ni) Alloys, Mater. Trans. **43**, 277 (2002).

[11] B. Cantor, I. T. H. Chang, P. Knight, and A. J. B. Vincent, Microstructural Development in Equiatomic Multicomponent Alloys, Mater. Sci. Eng. A **375–377**, 213 (2004).

[12] J.-W. Yeh, S.-K. Chen, S.-J. Lin, J.-Y. Gan, T.-S. Chin, T.-T. Shun, C.-H. Tsau, and S.-Y. Chang, Nanostructured High-Entropy Alloys with Multiple Principal Elements: Novel Alloy Design Concepts and Outcomes, Adv. Eng. Mater. **6**, 299 (2004).

[13] M. C. Gao, J.-W. Yeh, P. K. Liaw, and Y. Zhang, eds., *High-Entropy Alloys* (Springer International Publishing, Cham, 2016).

[14] B. S. Murty, J. W. Yeh, S. Ranganathan, and P. P. Bhattacharjee, *High-Entropy Alloys*, 2nd ed. (Elsevier, Amsterdam, Netherlands ; Cambridge, MA, 2019).

[15] A. Takeuchi, J. Wang, N. Chen, W. Zhang, Y. Yokoyama, K. Yubuta, and S. Zhu, $Al_{0.5}$TiZrPdCuNi High-Entropy (H-E) Alloy Developed through $Ti_{20}Zr_{20}Pd_{20}Cu_{20}Ni_{20}$ H-E Glassy Alloy Comprising Inter-Transition Metals, Mater. Trans. **54**, 776 (2013).

[16] T. Nagase, A. Takeuchi, K. Amiya, and T. Egami, Solid State Amorphization of Metastable $Al_{0.5}$TiZrPdCuNi High Entropy Alloy Investigated by High Voltage Electron Microscopy, Mater. Chem. Phys. High-Entropy Materials, **210**, 291 (2018).

[17] M. Kuveždić, E. Tafra, M. Basletić, R. Ristić, P. Pervan, V. Mikšić Trontl, I. A. Figueroa, and E. Babić, Change of Electronic Properties on Transition from High-Entropy to Ni-rich $(TiZrNbCu)_{1-x}Ni_x$ Alloys, J. Non-Cryst. Solids **531**, 119865 (2020).

[18] M. Kuveždić, E. Tafra, I. A. Figueroa, and M. Basletić, (Magneto)Transport Properties of $(TiZrNbNi)_{1-x}Cu_x$ and $(TiZrNbCu)_{1-x}Co_x$ Complex Amorphous Alloys, Materials **16**, 1711 (2023).

[19] J. Sólyom, *Fundamentals of the Physics of Solids Volume 1: Structure and Dynamics*, Vol. 1 (Springer, Berlin, Heidelberg, 2007).

[20] C. Suryanarayana and A. Inoue, *Bulk Metallic Glasses*, 2nd ed. (CRC Press, Taylor & Francis Group, Boca Raton, 2017).

[21] R. Ristić, I. A. Figueroa, A. Salčinović Fetić, K. Zadro, V. Mikšić Trontl, P. Pervan, and E. Babić, Transition from High-Entropy to Conventional $(TiZrNbCu)_{1-x}Co_x$ Metallic Glasses, J. Appl. Phys. **130**, 195102 (2021).

[22] R. Ristić, I. A. Figueroa, A. Lachová, Š. Michalik, V. Mikšić Trontl, P. Pervan, K. Zadro, D. Pajić, and E. Babić, Transition from High-Entropy to Cu-based $(TiZrNbNi)_{1-x}Cu_x$ Metallic Glasses, J. Appl. Phys. **126**, 154105 (2019).

[23] I. A. Figueroa, R. Ristić, A. Kuršumović, K. Biljaković, D. Starešinić, D. Pajić, G. Remenyi, and E. Babić, Properties of $(TiZrNbCu)_{1-x}Ni_x$ Metallic Glasses, J. Alloys Compd. **745**, 455 (2018).

[24] A. Cunliffe, J. Plummer, I. Figueroa, and I. Todd, Glass Formation in a High Entropy Alloy System by Design, Intermetallics **23**, 204 (2012).

[25] J. M. Ziman, *Models of Disorder: The Theoretical Physics of Homogeneously Disordered Systems* (Cambridge University Press, Cambridge, 1979).

[26] U. Mizutani, *Introduction to the Electron Theory of Metals* (Cambridge University Press, Cambridge, 2001).

[27] S. R. Elliott, *Physics of Amorphous Materials*, 2nd ed. (Longman Scientific & Technical ; J. Wiley, Harlow, Essex, England, New York, 1990).

[28] I. Bakonyi, Atomic Volumes and Local Structure of Metallic Glasses, Acta Materialia **53**, 2509 (2005).

[29] R. Ristić, J. R. Cooper, K. Zadro, D. Pajić, J. Ivkov, and E. Babić, Ideal Solution Behaviour of Glassy Cu–Ti,Zr,Hf Alloys and Properties of Amorphous Copper, J. Alloys Compd. **621**, 136 (2015).

[30] E. Babić, Đ. Drobac, I. A. Figueroa, M. Laurent-Brocq, Ž. Marohnić, V. Mikšić Trontl, D. Pajić, L. Perrière, P. Pervan, G. Remenyi, R. Ristić, A. Salčinović Fetić, D. Starešinić, and K. Zadro, Transition from High-Entropy to Conventional Alloys: Which Are Better?, Materials **14**, 5824 (2021).

[31] J. Sólyom, *Fundamentals of the Physics of Solids Volume II: Electronic Properties*, Vol. 2 (Springer, Berlin, Heidelberg, 2009).

[32] D. Greig, B. L. Gallagher, M. A. Howson, D. S. L. Law, D. Norman, and F. M. Quinn, Photoemission Studies on Metallic Glasses Using Synchrotron Radiation, Materials Science and Engineering **99**, 265 (1988).

[33] H. J. Güntherodt, P. Oelhafen, R. Lapka, H. U. Künzi, G. Indlekofer, J. Krieg, T. Laubscher, H. Rudin, U. Gubler, F. Rösel, K. P. Ackermann, B. Delley, M. Fischer, F. Greuter, F. Hauser, M. Liard, M. Müller, J. Kübler, K. H. Bennemann, and C. F. Hague, Electronic Structure of Liquid and Amorphous Metals, J. Phys. Colloques **41**, C8 (1980).

[34] P. Oelhafen, E. Hauser, and H. J. Güntherodt, Varying D-Band Splitting in Glassy Transition Metal Alloys, Solid State Commun. **35**, 1017 (1980).

[35] J. Ivkov, E. Babic, and R. L. Jacobs, Hall Effect and Electronic Structure of Glassy Zr 3d Alloys, J. Phys. F Met. Phys. **14**, L53 (1984).

[36] R. Zehringer, P. Oelhafen, H. J. Güntherodt, Y. Yamada, and U. Mizutani, Electronic Structure of $(Ni_{0.33}Zr_{0.67})_{0.85}X_{0.15}$ (X≡ Ti, V, Cr, Mn, Fe, Co and Cu)Metallic Glasses Studied by Photoelectron Spectroscopy, Materials Science and Engineering **99**, 317 (1988).

[37] E. Babić, D. Pajić, K. Zadro, K. Biljaković, V. M. Trontl, P. Pervan, D. Starešinić, I. A. Figueroa, A. Kuršumović, Š. Michalik, A. Lachová, G. Remenyi, and R. Ristić, Structure Property Relationship in $(TiZrNbCu)_{1-x}Ni_x$ Metallic Glasses, J. Mater. Res. **33**, 3170 (2018).

[38] P. Pervan, V. Mikšić Trontl, I. A. Figueroa, T. Valla, I. Pletikosić, and E. Babić, Compositionally Complex Alloys: Some Insights from Photoemission Spectroscopy, Materials **16**, 1486 (2023).

[39] D. G. Naugle and K. Rhie, Hall Effect in Amorphous Metals, AIP Conf. Proc. **286**, 61 (1992).

[40] B. L. Gallagher, D. Greig, and M. A. Howson, The Temperature Dependence of the Hall Coefficient of Metallic Glasses: Further Evidence for Electron-Electron Interaction Effects, J. Phys. F: Met. Phys. **14**, L225 (1984).

[41] B. L. Altshuler and A. G. Aronov, CHAPTER 1 - Electron–Electron Interaction In Disordered Conductors, in *Modern Problems in Condensed Matter Sciences*, Electron–Electron Interactions in Disordered Systems, Vol. 10, edited by A. L. Efros and M. Pollak (Elsevier, 1985) pp. 1–153.

[42] J. S. Drewery and R. H. Friend, The Hall Effect and Resistivity of Amorphous Copper-Titanium Alloys, J. Phys. F: Met. Phys. **17**, 1739 (1987).

[43] B. L. Gallagher, D. Greig, M. A. Howson, and A. A. M. Croxon, The Positive Hall Coefficients of Amorphous Transition-Metal Alloys, J. Phys. F: Met. Phys. **13**, 119 (1983).

[44] J. Ivkov and E. Babic, On the Origin of the Positive Hall Coefficient in Disordered TE-TL Alloys, J. Phys. Condens. Matter **2**, 3891 (1990).

[45] T. Richmond, L. Rohr, P. Reimann, G. Leemann, and H. J. Güntherodt, Electronic Transport Properties of Ni-Ta Metallic Glasses, Materials Science and Engineering: A Proceedings of the Seventh International Conference on Rapidly Quenched Materials, **133**, 63 (1991).

[46] D. Pavuna, On the Concentration Dependence of Transport Coefficients in Amorphous Transition Metal Alloys, Solid State Commun. **54**, 771 (1985).

[47] G. F. Weir, M. A. Howson, B. L. Gallagher, and G. J. Morgan, Hybridization in Amorphous Metals, Philos. Mag. B **47**, 163 (1983).

[48] J.-P. Jan, Effective Electronic Mass Tensor, Electrical Conductivity, and Hall Effect for Spherical Energy Surfaces, American Journal of Physics **30**, 497 (1962).

[49] D. Nguyen-Manh, D. Mayou, G. J. Morgan, and A. Pasturel, The Hall Coefficient and the Derivative of the Density of States in Amorphous Metals, J. Phys. F: Met. Phys. **17**, 999 (1987).

[50] M. L. Trudeau, R. W. Cochrane, and J. Destry, The Hall Effect in Paramagnetic Co-Zr Metallic Glasses, Materials Science and Engineering **99**, 187 (1988).

[51] B. Movaghar and R. Cochrane, The Hall Effect in Amorphous Metals and Alloys, Phys. Status Solidi B **166**, 311 (1991).

[52] N. Nagaosa, J. Sinova, S. Onoda, A. H. MacDonald, and N. P. Ong, Anomalous Hall Effect, Rev. Mod. Phys. **82**, 1539 (2010).

[53] J. H. Mooij, Electrical Conduction in Concentrated Disordered Transition Metal Alloys, Phys. Status Solidi A **17**, 521 (1973).

[54] B. L. Gallagher and D. Greig, The Thermoelectric Powers and Resistivities of Amorphous Transition Metal Alloys, J. Phys. F Met. Phys. **12**, 1721 (1982).

[55] M. A. Howson and D. Greig, Localisation and Interaction Effects in the Temperature and Magnetic Field Dependence of the Resistivity of Metallic Glasses, J. Phys. F: Met. Phys. **16**, 989 (1986).

[56] J. Sólyom, *Fundamentals of the Physics of Solids Volume 3 - Normal, Broken-Symmetry, and Correlated Systems*, Vol. 3 (Springer, Berlin, Heidelberg, 2010).

[57] G. Bergmann, Weak Anti-Localization—An Experimental Proof for the Destructive Interference of Rotated Spin 1/2, Solid State Communications **42**, 815 (1982).

[58] S. Chakravarty and A. Schmid, Weak Localization: The Quasiclassical Theory of Electrons in a Random Potential, Physics Reports **140**, 193 (1986).

[59] H. Fukuyama and K. Hoshino, Effect of Spin-Orbit Interaction on Magnetoresistance in the Weakly Localized Regime of Three-Dimensional Disordered Systems, J. Phys. Soc. Jpn. **50**, 2131 (1981).

[60] G. Bergmann, Weak Localization in Thin Films: A Time-of-Flight Experiment with Conduction Electrons, Physics Reports **107**, 1 (1984).

[61] B. L. Al'tshuler and P. A. Lee, Disordered Electronic Systems, Physics Today **41**, 36 (1988).

[62] G. Bergmann, Electron Scattering by Electron Holograms: The Physical Interpretation of the Coulomb Anomaly in Disordered Electron Systems, Phys. Rev. B **35**, 4205 (1987).

[63] P. A. Lee and T. V. Ramakrishnan, Disordered Electronic Systems, Rev. Mod. Phys. **57**, 287 (1985).

[64] D. V. Baxter, R. Richter, M. L. Trudeau, R. W. Cochrane, and J. O. Strom-Olsen, Fitting to Magnetoresistance under Weak Localization in Three Dimensions, J. Phys. France **50**, 1673 (1989).

[65] A. I. Larkin, Reluctance of Two-Dimensional Systems, Sov. J. Exp. Theor. Phys. Lett. **31**, 219 (1980).

[66] Z. Altounian and J. O. Strom-Olsen, Superconductivity and Spin Fluctuations in $M - \mathrm{Zr}$ metallic glasses ($M = \mathrm{Cu, Ni, Co, and Fe}$), Phys. Rev. B **27**, 4149 (1983).

[67] H. Fukuyama, CHAPTER 2 - Interaction Effects in the Weakly Localized Regime of Two- and Three-Dimensional Disordered Systems, in *Modern Problems in Condensed Matter Sciences*, Electron–Electron Interactions in Disordered Systems, Vol. 10, edited by A. L. Efros and M. Pollak (Elsevier, 1985) pp. 155–230.

[68] B. Kramer and A. MacKinnon, Localization: Theory and Experiment, Rep. Prog. Phys. **56**, 1469 (1993).

[69] M. A. Howson, Incipient Localisation and Electron-Electron Correlation Effects in Metallic Glass Alloys, J. Phys. F Met. Phys. **14**, L25 (1984).

[70] E. Babić and K. Šaub, Universal Conductivity Variation in Glassy Zr-M Alloys, Solid State Commun. **56**, 111 (1985).

[71] K. Šaub, E. Babić, and R. Ristić, Quantum Corrections to Conductivity of Glassy $Zr_{100-x}Cu_x$ Alloys, Solid State Commun. **53**, 269 (1985).

[72] B. J. Hickey, D. Greig, and M. A. Howson, Spin-Orbit Scattering in Amorphous CuTi Alloys, J. Phys. F: Met. Phys. **16**, L13 (1986).

[73] R. Ristić, Electrical Transport in Glassy Zr-3d Alloys, Fiz. J. Exp. Theor. Phys. **1**, 159 (1992).

[74] T. K. Nath and A. K. Majumdar, Quantum Corrections to Boltzmann Conductivity in (Cu,Ni)–Zr–Al Amorphous Alloys, Int. J. Mod. Phys. B **12**, 125 (1998).

[75] R. Delgado, H. Armbrüster, D. G. Naugle, C. L. Tsai, W. L. Johnson, and A. Williams, Electron Transport in $La_{100-x}Al_x$ Metallic Glasses, Phys. Rev. B **34**, 8288 (1986).

[76] U. Mizutani, M. Tanaka, and H. Sato, Studies of Negative TCR and Electronic Structure of Nonmagnetic Metallic Glasses Based on Y and La, J. Phys. F: Met. Phys. **17**, 131 (1987).

[77] Y. Yamada, Y. Itoh, T. Matsuda, and U. Mizutani, Electron Transport Studies of $Ni_{33}Zr_{67}$<script>-based metallic glasses containing H, B, Al and Si, J. Phys. F: Met. Phys. **17**, 2313 (1987).

[78] S. Kanemaki, M. Suzuki, Y. Yamada, and U. Mizutani, Low Temperature Specific Heat, Magnetic Susceptibility and Electrical Resistivity Measurements in Ni-Ti Metallic Glasses, J. Phys. F: Met. Phys. **18**, 105 (1988).

[79] U. Mizutani, Electron Transport Properties of Non-Magnetic Metallic Glasses, Materials Science and Engineering **99**, 165 (1988).

[80] U. Mizutani, C. Mishima, and T. Goto, Electron Transport Properties of Ternary Metallic Glasses $(Ni33Zr67)_{1-x}X_x$ (X=Ti, V, Cr, Mn, Fe, Co and Cu): The Magnetic Effect on the Electron Transport Properties, J. Phys.: Condens. Matter **1**, 1831 (1989).

[81] R. Harris and J. O. Strom-Olsen, Low Temperature Electron Transport in Metallic Glasses, in *Glassy Metals II: Atomic Structure and Dynamics, Electronic Structure, Magnetic Properties*, Topics in Applied Physics, edited by H. Beck and H.-J. Güntherodt (Springer, Berlin, Heidelberg, 1983) pp. 325–342.

[82] J. L. Black, Low-Energy Excitations in Metallic Glasses, in *Glassy Metals I: Ionic Structure, Electronic Transport, and Crystallization*, Topics in Applied Physics, edited by H.-J. Güntherodt and H. Beck (Springer, Berlin, Heidelberg, 1981) pp. 167–190.

[83] A. Halbritter, O. Yu. Kolesnychenko, G. Mihály, O. I. Shklyarevskii, and H. van Kempen, Transport Properties and Point-Contact Spectra of Ni_xNb_{1-x} Metallic Glasses, Phys. Rev. B **61**, 5846 (2000).

[84] M. B. Tang, H. Y. Bai, and W. H. Wang, Tunneling States and Localized Mode in Binary Bulk Metallic Glass, Phys. Rev. B **72**, 012202 (2005).

[85] A. Kawabata, Theory of Negative Magnetoresistance in Three-Dimensional Systems, Solid State Communications **34**, 431 (1980).

[86] B. L. Altshuler, A. G. Aronov, A. I. Larkin, and D. E. Khmel'nitzkii, Anomalous Magnetoresistance in Semiconductors, Zh. Eksp. Teor. Fiz. **81**, 768 (1981).

[87] J. C. Ousset, S. Askenazy, H. Rakoto, and J. M. Broto, Analytic Expressions of the Magnetoresistance Due to Localization and Electron-Electron Interaction Effects. - Application to the Amorphous Alloys La3Al and La3Ga, J. Phys. France **46**, 2145 (1985).

[88] J. B. Bieri, A. Fert, G. Creuzet, and A. Schuhl, Weak Localisation in Metallic Glasses. I: Magnetoresistance, J. Phys. F: Met. Phys. **16**, 2099 (1986).

[89] P. Lindqvist and O. Rapp, Weak Localisation and Interaction Effects in Amorphous CuTi Alloys, J. Phys. F: Met. Phys. **18**, 1979 (1988).

[90] Y. Isawa and H. Fukuyama, Higher Order Interaction Effects in Weakly Localized Regime: Case of Repulsive Force, J. Phys. Soc. Jpn. **53**, 1415 (1984).

[91] P. A. Lee and T. V. Ramakrishnan, Magnetoresistance of Weakly Disordered Electrons, Phys. Rev. B **26**, 4009 (1982).

[92] W. L. McLean and T. Tsuzuki, Higher-Field Magnetoresistance in Disordered Metals from Superconducting Interaction Effects, Phys. Rev. B **29**, 503 (1984).

[93] J. M. B. Lopes dos Santos and E. Abrahams, Superconducting Fluctuation Conductivity in a Magnetic Field in Two Dimensions, Phys. Rev. B **31**, 172 (1985).

[94] M. A. Howson, B. J. Hickey, and C. Shearwood, Quantum Interference Effects and the Magnetoresistance of Cu_{1-x} Ti_x Metallic Glasses, J. Phys. F: Met. Phys. **16**, L175 (1986).

[95] A. Sahnoune, J. O. Ström-Olsen, and H. E. Fischer, Influence of Spin-Orbit Scattering on the Magnetoresistance Due to Enhanced Electron-Electron Interactions, Phys. Rev. B **46**, 10035 (1992).

[96] F. M. Mayeya and M. A. Howson, Quantum Interference and Electron Interaction Effects in CaAl(Au,Ag) Amorphous Alloys, J. Phys.: Condens. Matter **4**, 9355 (1992).

[97] J. B. Bieri, A. Fert, G. Creuzet, and J. C. Ousset, Magnetoresistance of Amorphous CuZr : Weak Localization in a Three Dimensional System, Solid State Communications **49**, 849 (1984).

[98] A. Schulte and G. Fritsch, Conductivity of Three-Dimensional $Cu_{100-x}Ti_x$ Glasses at Low Temperatures-the Influence of Quantum Interference, Spin-Orbit Scattering and Electron-Electron Interaction Effects, J. Phys. F: Met. Phys. **16**, L55 (1986).

[99] P. Lindqvist, Analysis of the Magnetoresistance of Three-Dimensional Amorphous Metals with Weak Localization and Electron-Electron Interaction Theories, J. Phys.: Condens. Matter **4**, 177 (1992).

[100] M. G. Karkut and R. R. Hake, Upper Critical Fields and Superconducting Transition Temperatures of Some Zirconium-Base Amorphous Transition-Metal Alloys, Phys. Rev. B **28**, 1396 (1983).

[101] W. Johnson, Superconductivitvy in Metallic Glasses, J. Phys. Colloq. **41**, C8 (1980).

[102] I. Bakonyi, Electronic Properties and Atomic Structure of (Ti, Zr, Hf)-(Ni, Cu) Metallic Glasses, Journal of Non-Crystalline Solids **180**, 131 (1995).

[103] E. Babić, R. Ristić, M. Miljak, M. G. Scott, and G. Gregan, Superconductivity in Zirconium-Nickel Glasses, Solid State Commun. **39**, 139 (1981).

[104] E. Tafra, M. Basletić, R. Ristić, E. Babić, and A. Hamzić, Enhanced Superconductivity in Hf-base Metallic Glasses, J. Phys. Condens. Matter **20**, 425215 (2008).

[105] N. Toyota, A. Inoue, T. Fukase, and T. Masumoto, Upper Critical Field and Related Properties of Superconducting Amorphous Alloys Zr-Si, J Low Temp Phys **55**, 393 (1984).

[106] A. Nordström, Ö. Rapp, and Z.-Y. Liu, Critical Magnetic Field of Disordered Zr-Cu Alloys: Density of States and Spin-Orbit Scattering Time, Phys. Rev. B **41**, 6708 (1990).

[107] N. R. Werthamer, E. Helfand, and P. C. Hohenberg, Temperature and Purity Dependence of the Superconducting Critical Field, H_{c2}. III. Electron Spin and Spin-Orbit Effects, Phys. Rev. **147**, 295 (1966).

[108] K. Maki, Effect of Pauli Paramagnetism on Magnetic Properties of High-Field Superconductors, Phys. Rev. **148**, 362 (1966).

[109] E. Batalla, Z. Altounian, and J. O. Strom-Olsen, Magnetism and Electron-Mass Enhancement in Zirconium-Rich Fe-Zr and Co-Zr Metallic Glasses, Phys. Rev. B **31**, 577 (1985).

[110] P. W. Anderson, Absence of Diffusion in Certain Random Lattices, Phys. Rev. **109**, 1492 (1958).

[111] V. F. Gantmakher, *Electrons and Disorder in Solids*, edited by L. I. Man (Oxford University Press, 2005).

[112] S. N. F. Mott and E. A. Davis, *Electronic Processes in Non-crystalline Materials* (Clarendon Press, 1979).

[113] B. I. Shklovskii and A. L. Efros, *Electronic Properties of Doped Semiconductors*, edited by M. Cardona, P. Fulde, and H.-J. Queisser, Springer Series in Solid-State Sciences, Vol. 45 (Springer Berlin Heidelberg, Berlin, Heidelberg, 1984).

[114] D. J. Thouless, Electrons in Disordered Systems and the Theory of Localization, Physics Reports **13**, 93 (1974).

[115] N. F. Mott, Conduction in Glasses Containing Transition Metal Ions, Journal of Non-Crystalline Solids **1**, 1 (1968).

[116] A. L. Efros and B. I. Shklovskii, Coulomb Gap and Low Temperature Conductivity of Disordered Systems, J. Phys. C: Solid State Phys. **8**, L49 (1975).

[117] X. Yu, P. M. Duxbury, G. Jeffers, and M. A. Dubson, Coalescence and Percolation in Thin Metal Films, Phys. Rev. B **44**, 13163 (1991).

[118] B. Abeles, P. Sheng, M. Coutts, and Y. Arie, Structural and Electrical Properties of Granular Metal Films, Adv. Phys. **24**, 407 (1975).

[119] I. S. Beloborodov, A. V. Lopatin, V. M. Vinokur, and K. B. Efetov, Granular Electronic Systems, Rev. Mod. Phys. **79**, 469 (2007).

[120] B. Abeles, H. L. Pinch, and J. I. Gittleman, Percolation Conductivity in W-Al_2O_3 Granular Metal Films, Phys. Rev. Lett. **35**, 247 (1975).

[121] M. Pollak and C. J. Adkins, Conduction in Granular Metals, Philos. Mag. B **65**, 855 (1992).

[122] J. Zhang and B. I. Shklovskii, Density of States and Conductivity of a Granular Metal or an Array of Quantum Dots, Phys. Rev. B **70**, 115317 (2004).

[123] I. M. Lifshitz, Energy Spectrum Structure and Quantum States of Disordered Condensed Systems, Sov. Phys. Usp. **7**, 549 (1965).

[124] K. Biljaković, G. Remenyi, I. A. Figueroa, R. Ristić, D. Pajić, A. Kuršumović, D. Starešinić, K. Zadro, and E. Babić, Electronic Structure and Properties of $(TiZrNbCu)_{1-x}Ni_x$ High Entropy Amorphous Alloys, J. Alloys Compd. **695**, 2661 (2017).

[125] E. Babić, I. A. Figueroa, S. Michalik, V. Mikšić-Trontl, P. Pervan, R. Ristić, A. Salčinović-Fetić, D. Starešinić, and K. Zadro, Influence of Early Transition Metals on Properties of Ti-Zr-Nb-Cu-Ni Complex Glassy Alloys, (2023), (*manuscript in preparation*).

[126] R. Morel, Y. Huai, and R. W. Cochrane, Resistivity and Hall Effect in Sputtered NiZr Metallic Glasses, Journal of Applied Physics **64**, 5462 (1988).

[127] K. D. D. Rathnayaka, A. B. Kaiser, and H. J. Trodahl, Electronic-Transport Properties of Amorphous Cu-Ti Films, Phys. Rev. B **33**, 889 (1986).

[128] K. D. D. Rathnayaka, K. Rhie, B. D. Hennings, and D. G. Naugle, Electronic Transport Properties of Amorphous Ti-Ni and Hf-Ni Alloys, J. Phys.: Condens. Matter **5**, 7251 (1993).

[129] M. Hosseini and J. Koike, Amorphous CoTix as a Liner/Diffusion Barrier Material for Advanced Copper Metallization, Journal of Alloys and Compounds **721**, 134 (2017).

[130] T. Jagielinski, Magnetic and Galvanomagnetic Properties of Amorphous CoZr Thin Films, Journal of Applied Physics **61**, 3237 (1987).

[131] K. Stolze, J. Tao, F. O. von Rohr, T. Kong, and R. J. Cava, Sc–Zr–Nb–Rh–Pd and Sc–Zr–Nb–Ta–Rh–Pd High-Entropy Alloy Superconductors on a CsCl-Type Lattice, Chem. Mater. **30**, 906 (2018).

[132] L. Sun and R. J. Cava, High-Entropy Alloy Superconductors: Status, Opportunities, and Challenges, Phys. Rev. Mater. **3**, 090301 (2019).

[133] K. Samwer and H. v. Löhneysen, Amorphous Superconducting Zr_xCu_{1-x}: Electronic Properties, Stability, and Low-Energy Excitations, Phys. Rev. B **26**, 107 (1982).

[134] M. A. Howson, D. Greig, B. L. Gallagher, and G. J. Morgan, The Hall Coefficients of CuTi and CuHf Amorphous Metal Alloys, J. Non-Cryst. Solids **61–62**, 1261 (1984).

[135] K. H. J. Buschow, Stability and Electrical Transport Properties of Amorphous $Ti_{1-x}Ni_x$ Alloys, J. Phys. F: Met. Phys. **13**, 563 (1983).

[136] J. S. Dugdale, *The Electrical Properties of Metals and Alloys* (Dover Publications, 2016).

[137] M. Čulo, E. Tafra, B. Mihaljević, M. Basletić, M. Kuveždić, T. Ivek, A. Hamzić, S. Tomić, T. Hiramatsu, Y. Yoshida, G. Saito, J. A. Schlueter, M. Dressel, and B. Korin-Hamzić, Hall Effect Study of the κ-$(ET)_2X$ Family: Evidence for Mott-Anderson Localization, Phys. Rev. B **99**, 045114 (2019).

[138] A. G. Zabrodskii, The Coulomb Gap: The View of an Experimenter, Philos. Mag. B **81**, 1131 (2001).

[139] D. V. Louzguine, A. R. Yavari, K. Ota, G. Vaughan, and A. Inoue, Synchrotron X-ray Radiation Diffraction Studies of Thermal Expansion, Free Volume Change and Glass Transition Phenomenon in Cu-based Glassy and Nanocomposite Alloys on Heating, Journal of Non-Crystalline Solids **351**, 1639 (2005).

[140] A. Inoue, W. Zhang, T. Zhang, and K. Kurosaka, High-Strength Cu-based Bulk Glassy Alloys in Cu–Zr–Ti and Cu–Hf–Ti Ternary Systems, Acta Mater. **49**, 2645 (2001).

[141] J. O. Strom-Olsen, Z. Altounian, R. W. Cochrane, and A. B. Kaiser, Spin-Fluctuation Effects in the Resistivity of Fe-Zr Metallic Glasses, Phys. Rev. B **31**, 6116 (1985).

[142] M. L. Trudeau and R. W. Cochrane, Magnetoresistivity Studies of Zr-M Amorphous Alloys (M=Ni, Co, and Fe): From Superconductivity to Ferromagnetism, Phys. Rev. B **41**, 10535 (1990).

[143] Z. Altounian, S. V. Dantu, and M. Dikeakos, Effects of Spin Fluctuations on the Resistivity of Metallic Glasses, Phys. Rev. B **49**, 8621 (1994).

[144] T. Castner, Hopping Conduction in the Critical Regime Approaching the Metal–Insulator Transition, in *Hopping Transport in Solids*, Vol. 28, edited by M. Pollak and B. I. Shklovskii (Elsevier, 1991) pp. 1–47.

[145] T. B. Tran, I. S. Beloborodov, X. M. Lin, T. P. Bigioni, V. M. Vinokur, and H. M. Jaeger, Multiple Cotunneling in Large Quantum Dot Arrays, Phys. Rev. Lett. **95**, 076806 (2005).

[146] C. L. Tsai and F. C. Lu, Electronic Transport Properties of La-Al Metallic Glasses, Journal of Applied Physics **55**, 1945 (1984).

[147] I. Kokanović, B. Leontić, and J. Lukatela, Weak-Localization and Coulomb-interaction Effects in Hydrogen-Doped Zr-Ni and Zr-Cu Metallic Glasses, Phys. Rev. B **41**, 958 (1990).

[148] I. Kokanović, B. Leontić, S. Rešetić, J. Lukatela, and Ž. Marohnić, The Electrical Resistivity of Hydrogen-Doped Zr-Co Metallic Glasses, Journal of Non-Crystalline Solids **185**, 163 (1995).

[149] R. W. Cochrane and J. O. Strom-Olsen, Scaling Behavior in Amorphous and Disordered Metals, Phys. Rev. B **29**, 1088 (1984).

[150] T. Moriya, *Spin Fluctuations in Itinerant Electron Magnetism*, edited by P. Fulde, M. Cardona, and H.-J. Queisser, Springer Series in Solid-State Sciences, Vol. 56 (Springer, Berlin, Heidelberg, 1985).

Biography

Marko Kuveždić was born on January 7th, 1992, in Varaždin. He attended elementary schools in Rijeka and Lovas. In 2010, he completed a mathematically-oriented gymnasium in Vukovar and enrolled in the integrated undergraduate and graduate university study of Physics at the Department of Physics, Faculty of Science, University of Zagreb. He graduated on September 3rd, 2015, with a thesis titled *Transport and dielectric properties of chosen BEDT-TTF organic materials*, supervised by assoc. prof. dr. sc. Mario Basletić. The same year, he enrolled in the doctoral program in condensed matter physics at the Department of Physics, Faculty of Science, University of Zagreb. Since 2016, he has worked as a teaching assistant there and collaborated in the Low Temperature and Strong Magnetic Field Laboratory led by assoc. prof. dr. sc. Mario Basletić. As a teaching assistant, he contributed to multiple courses: Physics laboratory, Statistics and Basic Measurements, Electronics Lab, Laboratory in Fundamentals in Electronics, Microelectronics, and Fundamentals of Electronics. From 2018 to 2022, he participated in the HRZZ project *Sulfosalts: new generation of complex functional materials* (Main investigator: prof. dr. sc. Denis Sunko). To date, he has co-authored 6 articles published in journals indexed in the Current Contents database, and he is the first author on 2 of them. He has participated in scientific meetings, presenting 4 times with a poster and once with an oral presentation.

List of publications

1. M. Pinterić, P. Lazić, A. Pustogow, T. Ivek, M. Kuveždić, O. Milat, B. Gumhalter, M. Basletić, M. Čulo, B. Korin-Hamzić, A. Löhle, R. Hübner, M. Sanz Alonso, T. Hiramatsu, Y. Yoshida, G. Saito, M. Dressel, and S. Tomić, Anion effects on electronic structure and electrodynamic properties of the Mott insulator $\kappa - (\mathrm{BEDT-TTF})_2\mathrm{Ag}_2(\mathrm{CN})_3$, Phys. Rev. B **94**, 161105 (2016)
2. T. Ivek, M. Čulo, M. Kuveždić, E. Tutiš, M. Basletić, B. Mihaljević, E. Tafra, S. Tomić, A. Löhle, M. Dressel, D. Schweitzer, and B. Korin-Hamzić, Semimetallic and charge-ordered $\alpha - (\mathrm{BEDT\text{-}TTF})_2\mathrm{I}_3$: On the role of disorder in dc transport and dielectric properties, Phys. Rev. B **96**, 075141 (2017)
3. J. Hu, B. Ernst, S. Tu, M. Kuveždić, A. Hamzić, E. Tafra, M. Basletić, Y. Zhang, A. Markou, C. Felser, A. Fert, W. Zhao, J.-P. Ansermet, and H. Yu, Anomalous Hall and Nernst Effects in $\mathrm{Co}_2\mathrm{TiSn}$ and $\mathrm{Co}_2\mathrm{Ti}_{0.6}\mathrm{V}_{0.4}\mathrm{Sn}$ Heusler Thin Films, Phys. Rev. Appl. **10**, 044037 (2018)
4. M. Čulo, E. Tafra, B. Mihaljević, M. Basletić, M. Kuveždić, T. Ivek, A. Hamzić, S. Tomić, T. Hiramatsu, Y. Yoshida, G. Saito, J. A. Schlueter, M. Dressel and B. Korin-Hamzić, Hall Effect Study of the κ-$(\mathrm{ET})_2X$ Family: Evidence for Mott-Anderson Localization, Phys. Rev. B **99**, 045114 (2019)
5. M. Kuveždić, E. Tafra, M. Basletić, R. Ristić, P. Pervan, V. Mikšić Trontl, I. A. Figueroa, and E. Babić, Change of electronic properties on transition from high-entropy to Ni-rich $(\mathrm{TiZrNbCu})_{1-x}\mathrm{Ni}_x$ alloys, J. Non-Cryst. Solids **531**, 119865 (2020)
6. M. Kuveždić, E. Tafra, I. A. Figueroa, and M. Basletić, (Magneto)Transport Properties of $(\mathrm{TiZrNbNi})_{1-x}\mathrm{Cu}_x$ and $(\mathrm{TiZrNbCu})_{1-x}\mathrm{Co}_x$ Complex Amorphous Alloys, Materials **16**, 1711 (2023)